Estimating the Sun's Open Magnetic Flux

Anna Marie Frost

Department of Meteorology

School of Mathematical, Physical and Computational Sciences

University of Reading

A thesis submitted for the degree of Doctor of Philosophy

September 2023

Abstract

The aims of this thesis were to quantify the Sun's open magnetic flux and understand its evolution with time. The Sun's open solar flux (OSF) is the component of the Sun's magnetic field that reaches a sufficient height to be dragged into the heliosphere by the solar wind. Photospheric estimates currently fail to accurately reconstruct the OSF as observed by *in-situ* spacecraft. As photospheric estimates are the basis for all long lead time space weather forecasts, the ability to reconstruct the OSF acts as a test of coronal models.

The work in the thesis is comprised of three studies. The first study details how we determined the topology of the magnetic field from the combination of the electron and radial magnetic field data. Within this chapter, we used observational results from 4 studies to constrain the conditions used to determine the topology of the magnetic field.

The second study used the topologies from the first chapter to calculate and correct the OSF. The biggest correction made to the OSF was the removal of locally inverted flux, which, being incorrectly assumed to be open flux, increases the calculated OSF. While this is part of the cause of the discrepancy between OSF estimates from *in-situ* and magnetograms, there is still a disagreement.

Finally, the third study investigated the variation of different magnetic field topologies and solar wind properties at true polarity reversals. Within this chapter the combination of the topologies from the first chapter and solar wind properties allowed us to understand the formation of the detected inverted flux prior to polarity reversals.

Declaration

I, Anna Marie Frost, confirm that the work presented in this thesis is my own. Where information has been derived from other sources, this has been indicated in the work.

Please note that some of the contents of this thesis have been previously reported in the following journal paper:

Frost, A.M., Owens, M., Macneil, A. et al. Estimating the Open Solar Flux from In-Situ Measurements. Sol Phys 297, 82 (2022). https://doi.org/10.1007/s11207-022-02004-6

Acknowledgements

First and foremost, I would like to thank my supervisors, Matt Owens and Mike Lockwood, for their continuous support and guidance throughout my PhD. Thank you for always keeping me on track, I think it's safe to say I wouldn't have made it here without you.

I would also like to give a special thanks to Allan Macneil. Thank you for your support with my coding during the first 2 years of my PhD and for answering my many, many questions.

Thank you to the members of SPATE for listening to my presentations on my research and helping me see where they sit in the wider context of space physics. I would also like to thank the members of my monitoring committee, Chris Scott and Hilary Weller, for pushing me and making me look at the big picture of my research.

I would like to give a huge thanks to Lauren James and the rest of my cohort. Lauren, thank you for keeping me sane throughout the last 4 years. Having someone to go through this process with has been invaluable.

Finally, thank you to all my family. Stuart, thank you for believing in me and encouraging me to keep going when I felt like giving up. Mum and Dad, thank you for your unwavering support.

I would also like to acknowledge the Science and Technology Facilities Council for financial support of my PhD studies.

Contents

1 Introduction **1**

1.1 Single-Particle Motion 2

1.2 Basic plasma physics 3

1.2.1 Electromagnetism 5

1.2.2 Magnetohydrodynamics 6

1.2.3 Magnetic Reconnection 8

1.3 The Sun 9

1.3.1 Solar Cycle 11

1.3.2 Coronal Holes 12

1.3.3 Coronal Mass Ejections 13

1.3.4 Flares 14

1.4 Solar Wind and the Heliosphere 16

1.4.1 Models of Solar Wind Expansion 17

1.4.2 Heliospheric Magnetic Field 20

1.5 Summary and Context 23

2 Background Material **24**

2.1 Magnetograms 24

2.1.1 OSF from Magnetograms 25

2.1.2 PFSS model 28

2.2 In-situ Observations 30

2.2.1 Early In-Situ Results . . . 31

2.2.2 OSF from In-situ Measurements . . . 32

2.3 OSF Problem . . . 34

2.4 Summary . . . 35

3 Instrumentation and Data 40

3.1 Detectors . . . 40

3.1.1 Fluxgate Magnetometer . . . 40

3.1.2 Top-Hat Electrostatic Analysers . . . 41

3.2 ACE Mission . . . 43

3.2.1 SWEPAM . . . 44

3.2.2 MAG . . . 44

3.2.3 ACE Data . . . 45

3.3 *Wind* Mission . . . 46

3.3.1 3DP . . . 46

3.3.2 SWE . . . 47

3.3.3 MFI . . . 47

3.3.4 *Wind* Data . . . 48

3.4 Data Calibration . . . 49

3.5 Conclusion . . . 50

4 Classifying the Topology of the HMF 57

4.1 Introduction . . . 58

4.2 Determining Field Topology . . . 61

4.3 Method . . . 64

4.3.1 Calibration Between Spacecraft . . . 65

4.4 Results and Discussion . . . 66

4.4.1 Topology of the Magnetic Field . . . 66

4.4.2 Constraining the Strahl Conditions . . . 69

4.4.3 Effect of Strahl Criteria on OSF 74

4.5 Conclusions 75

5 Estimating the OSF from In-Situ Measurements 77

5.1 Introduction 78

5.1.1 Methods of Estimating OSF 79

5.1.2 Previous studies 80

5.2 Method 82

5.2.1 Topology of the Field 82

5.2.2 Open Solar Flux 82

5.3 Results and Discussion 84

5.3.1 Open Solar Flux 84

5.3.2 Data Gaps 86

5.3.3 OSF Best Estimate 91

5.3.4 Time-averaging Approximation 93

5.3.5 *In-situ* and magnetogram OSF comparisons 96

5.4 Conclusions 97

6 HMF Topologies Around True Polarity Reversals 101

6.1 Introduction 102

6.1.1 Magnetic Reconnection 103

6.1.2 Statistical Analysis of HCS Crossings 104

6.2 Methods 106

6.2.1 Topology of the Field 106

6.2.2 Determining Field Polarity 106

6.2.3 Locating True Polarity Reversals 107

6.2.4 Superposed Epoch Analysis Method 108

6.3 Results and Discussion 109

6.3.1 Field Direction 109

6.3.2 Superposed Epoch Analysis 110
6.3.3 Offset Between Mean Values and Background 115
6.3.4 Smoothing Period and the Number of Reversals 116
6.3.5 Formation of Inverted Flux 117
6.4 Conclusions and Future Work 118

7 Conclusions and Future Work 125

7.1 Review of Results 126
7.1.1 Classifying the Topology of the HMF 126
7.1.2 Estimating the OSF from *In-Situ* Measurements 128
7.1.3 HMF Topologies Around True Polarity Reversals 129
7.2 Future Work: Ulysses 131

List of Figures

1.1 Schematic from Baumjohann and Treumann (1996) showing the simplified geometry of magnetic reconnection. 8

1.2 Schematic of the internal structure of the Sun. From the centre to the outer atmosphere, the Sun consists of: core (*pale yellow*), radiative zone (*yellow*), convective zone (*orange*), photosphere (*orange-red*), chromosphere (*red*), transition region (*brown*), and the corona (*cream*). (Image from NICT, the National Institute of Information and Communications Technology). 9

1.3 Average temperature and density of the quiet Sun where zero is the solar surface at one solar radius. Plot taken from de Patoul (2012). 10

1.4 Plot from Hathaway (2017) showing the monthly averages of the sunspot numbers. 12

1.5 Plot from Hathaway (2017) showing the butterfly diagram (top panel), which is the distribution of sunspots with latitude. The bottom panel shows the fractional coverage of sunspots as a function of solar latitude and time. 13

1.6 A coronal hole in different wavelengths and in a magnetogram from Macneil (2018). The 2 left panels are from SDO-HMI and the 4 right panels are from SDO-AIA with the wavelengths labelled on each panel. 14

1.7 Plot from Webb and Howard (2012) showing the evolution of a CME observed by the LASCO C2 coronagraph on 2 June 1998. 15

1.8 Figure from Parker (1965) showing the radial distance (x-axis) against the solar wind velocity (v). This shows the five solutions to the solar wind equation. 19

1.9 Figure from Macneil (2018) showing the Parker spiral HMF in the ecliptic plane, viewed from the north pole. The direction of rotation (Ω), solar wind bulk velocity (**v**), magnetic field vector (**B**) and components (B_ϕ and B_r) are all shown. 21

1.10 A schematic of the Sun's magnetic field. The red and blue lines are magnetic field lines of opposite polarity and the dashed green line is the heliospheric current sheet (HCS) separating the two polarities. The left panel shows a Parker spiral magnetic field (Owens and Forsyth, 2013) and the right panel shows the magnetic field with local inversions at 1 AU (credit: Prof. Mathew Owens). 22

1.11 A cartoon of the global structure of the heliosphere from Owens and Forsyth (2013). Within the heliopause, where the solar wind flow is supersonic, a termination shock forms to slow and deflect the solar wind within the heliosheath. Beyond the heliopause, the nearby interstellar medium (known as the very local interstellar medium or VLISM) is diverted around the heliosphere. Whether this interaction includes a stationary bow shock depends on the magnetic field's intensity and alignment within the VLISM. 23

2.1 Figure from Okamoto and Sakurai (2018) showing a sunspot and its spectra observed with the Hinode SOT/SP (Solar Optical Telescope Spectropolarimeter). The panel on the left shows a continuum map of a sunspot scanned around 19 UT on 4/2/2014. The panel in the middle shows the splitting spectrum taken along the white line in the left panel. A large distance in the splitting indicates a strong magnetic field. On the right is a simplified diagram of the splitting of the iron absorption line. The magnetic field strength at location 1 exceeded 6 kG, while the magnetic field strength at location 2 was 3.5-4.5 kG. 25

2.2 Full disk magnetogram from the National Solar Observatory. NISP/SOLIS magnetogram from 18 June 2014 during solar maximum. The grey areas show weak magnetic field, the dark areas show "south" magnetic polarity, and the white areas show "north" magnetic polarity. 26

2.3 Figure adapted from Riley et al. (2019) showing the line-of-sight component of the photospheric magnetic field with small spots added to the polar regions (the added spots are synthetic data). Panel A) shows the view from Earth when Earth is in the solar equatorial plane. Panel B) shows the view from Earth when Earth's position is at 7.25° above the solar equatorial plane. Panel C) shows the view from 30° above the solar equatorial plane. 27

2.4 Schematic from Schatten et al. (1969) showing the PFSS model magnetic field lines. 28

2.5 Schematic from Nikolic (2019) showing PFSS modeled coronal holes, in red and blue, using the CR 2060 GONG synoptic map and the source surface placed at (a) $R_{SS} = 1.3R_{\odot}$, (b) $R_{SS} = 1.5R_{\odot}$, and (c) $R_{SS} = 2.5R_{\odot}$. (d) SOHO EIT 195 Å CR 2060 synoptic map of the solar corona. The red rectangles in (d) mark some coronal holes that are not fully captured by the PFSS model with $R_{SS} = 2.5R_{\odot}$. 36

2.6 Schematic from Lee et al. (2011) showing PFSS modeled coronal holes, in red and blue, using the CR 2060 MDI synoptic map and the source surface placed at $R_{SS} = 1.3R_\odot$, $R_{SS} = 1.5R_\odot$, and $R_{SS} = 2.5R_\odot$. The bottom panel shows the STEREO/EUVI image of CR 2060 synoptic map of the solar corona. The yellow circles mark the coronal hole features missing from the $R_{SS} = 2.5R_\odot$ results and the grey rectangles mark the features that appear in the mapping results but not in the EUV image. 37

2.7 Sketch of the polarity of the heliospheric magnetic field from Vallee (1998). The location of the heliospheric current sheet is shown by the black line (and the dashed line showing the back side of the Sun). Moving around the equatorial plane (shown by the dots) one rotation passes through 4 different polarities, hence 4 magnetic sectors. 38

2.8 Schematic from Kahler et al. (1996) showing (**A**) a field resulting from an inverted unipolar field, and (**B**) a field with a polarity reversal embedded in a sector. 38

2.9 Schematic of the topology of the HMF viewed from the heliographic equatorial plane. The *solid black lines* are the magnetic field lines with *black arrows* indicating the direction. The *grey dashed line* is 1 AU. (**a**) shows an area of open magnetic flux with a locally inverted field. (**b**) shows an area of open magnetic flux as detected from point measurements. 39

2.10 Figure from Owens et al. (2008) showing the increasing Φ_R estimates with increasing radial distance for various spacecraft (colour-coded as shown on the right of the plot). Beyond $R = 2.5AU$, marked by the *vertical dashed line*, there is a clear positive increase in Φ_R with radius. 39

3.1 Schematic showing a single-axis fluxgate magnetometer sensor, see text for description. Image taken from Senthilmurugan et al. (2020). 41

3.2 Schematic showing a Top Hat electrostatic analyser. The top illustration shows a cross-section of the analyser and the bottom illustration shows the detector. Image taken from Paschmann and Daly (1998). 42

3.3 Schematic showing the same top hat analyser from Figure 3.2 with particle trajectories shown by thick black lines. Image taken from Paschmann and Daly (1998). 43

3.4 Exploded view of the ACE spacecraft structure showing the position of all instruments. Image taken from Stone et al. (1998). 51

3.5 6 hours of ACE observations from 4th January 2007. From top to bottom, the panels show: the variation with time of the suprathermal electron pitch angle distribution function ($f(\alpha, t)$, units s^{3}cm^{-6}), the same as the top panel normalised to the maximum and minimum flux at each time step, and the radial magnetic field in GSE coordinates (units nT). 52

3.6 Schematic of the WIND spacecraft with instrument locations. Image credit: NASA. 53

3.7 6 hours of *Wind* observations from 4th January 2007. From top to bottom, the panels show: the variation with time of electron number flux (units cm^{-2}ster^{-1}eV^{-1}s^{-1}), the same as the top panel normalised to the maximum and minimum flux at each time step, and the radial magnetic field in GSE coordinates (units nT). 54

3.8 6 hours of *Wind* observations from 4th January 2007. Each plot shows the variation with time of electron number flux (units cm^{-2}ster^{-1}eV^{-1}s^{-1}) normalised to the maximum and minimum flux at each time step for energies 13eV, 265eV, and 1113eV. 54

3.9 A plot of *Wind's* orbit between April 1998 and April 1999 adapted from a NASA plot. Image credit: Mike Lockwood. 55

3.10 (a) A schematic of the conditions used to remove *Wind* data from within the magnetosheath (shocked solar wind) or magnetosphere in GSE coordinates. The *solid black line* represents the shape of the bow shock (not to scale) and the *red dashed lines* represent the conditions used to remove the undisturbed solar wind data. (b) The percentage of *Wind* data removed per Carrington rotation due to the encounter with the bow shock. (c) Comparison of missing data from spacecraft. The percentage of missing ACE (*red line*) and *Wind* (*black line*) data in each Carrington rotation between 1994 and 2021. The *Wind* missing data includes both data missing from the electron and magnetic fields data sets, and data subsequently removed from within the bow shock. 56

4.1 Diagram from Graham (2018), showing the different solar wind electron populations: core (blue), halo (green), and strahl (red), which have Maxwellian, Kappa, and field-aligned beam forms, respectively. (Top) the two-dimensional velocity distribution functions, in field-parallel ($v_{\|}$) and field-perpendicular ($v_{\perp}$) velocity space, f($v_{\|}$,$v_{\perp}$) and (bottom) the one-dimensional cut through the distribution in the field-parallel direction, f($v_{\|}$). Image credit: Marc Pulupa. 59

4.2 Figure 1 from Hammond et al. (1996), showing three pitch angle distributions seen in the high-speed solar wind. Top two panels show 77 eV electrons (9×10^5 K) while the bottom panel is 115 eV electrons (1.3×10^6 K). Dots are the measured data and filled circles are these data binned into 15° wide pitch angle bins. The solid line in the top panel is a Gaussian fit to all the data, whereas in the bottom panel, it is the sum of two Gaussian's fitted with peaks at α of 0 and 180°. . . . 60

4.3 Schematic modified from Owens and Forsyth (2013) displaying the topology of the HMF as inferred from suprathermal electron (STE) observations. (**a**) the heliographic equatorial plane, with heliospheric magnetic field lines (*black arrows*) and the STE flux (*red arrows*) for different magnetic topologies. (**b**) the suprathermal electron pitch-angle time spectrogram. (**c**) the radial magnetic field time series that would be seen as the structure shown in (**a**) is constant and rotates over the spacecraft. The combination of electron and magnetic data can be used to distinguish between: open flux (points *1* and *3*), newly emerged open flux (point *2*), inverted flux (*4*), and flux that has been disconnected from the Sun (*5*). 63

4.4 A schematic of a suprathermal electron pitch-angle distribution and the criteria used to algorithmically determine the strahl direction. F_{90} is the background flux (taken from the *blue shaded bars*, i.e., pitch angles α near 90°), F_0 is the flux at pitch-angles near 0° (taken from the *grey shaded bars*), and F_{180} is the flux at pitch-angles near 180° (taken from the *yellow shaded bars*). PAB is the percentage above the background flux, and PAO is the percentage above the flux in the opposite direction. Thresholds on these values are used to classify the existence of strahl in the field-parallel direction and/or the field anti-parallel direction. 64

4.5 12 hours of ACE observations from 14th January 2007. Panels show: **A**) the variation with time of the suprathermal electron pitch angle distribution function ($f(\alpha, t)$, units s^{3}cm^{-6}), **B**) the same as **A** normalised to the maximum and minimum flux at each time step, **C**) the radial magnetic field (nT), and **D**) topology indicator of the magnetic field. $+1$ shows times where the field is topologically open and -1 shows times where the field is topologically inverted. 67

4.6 A single Carrington-rotation of ACE observations from 23rd October to 19th November 2008. Panels show: **A**) the suprathermal electron pitch angle distribution function ($f(\alpha, t)$ for an energy E = 272 eV, units s^{3}cm^{-6}), normalized to the maximum and minimum flux at each time step, **B**) the PAB at 0^o PA (*black line*) and 180^o PA (*red line*), and **C**) the PAO at 0^o PA (*black line*) and 180^o PA (*red line*). Note that both PAB and PAO are shown on logarithic scales. 68

4.7 Average over the interval 1994 to 2021 as a function of strahl identification criteria, PAO and PAB. Panels show: **A**) Inverted, **B**) Uninverted, **C**) Counterstreaming and **D**) Undetermined flux percentages. 69

4.8 Selecting strahl identification criteria using previous studies. **A**) Average CS flux measured by ACE between 3/2/2008 - 27/10/2008, the period of study from Skoug et al. (2000). CS values of 16% (*red line*) with 1-sigma range about the reported percentage (*black lines*). **B**) Average CS flux measured by ACE between 1998-2002, the period of study from Anderson et al. (2012). CS values of 10% (*red line*) with 1-sigma range about the reported percentage (*black lines*). **C** Average undetermined flux measured by *Wind* between 1995-1998, the period of study from Pagel, Crooker and Larson (2005). Disconnected flux of 10% (*red line*) with 1-sigma range about the reported percentage (*black lines*). **D**) Average CS flux measured by *Wind* at solar maximum, same solar cycle period used by Gosling et al. (1992). CS values of 14.7% (*red line*) with 1-sigma range about the reported percentage (*black lines*). **E**) Same as plot **D**, but with ACE data. **F**) Values of PAO and PAB that are consistent with previous studies: *black lines* (**A**), *magenta line* (**B**), *yellow horizontal lines* (**C**), *red and blue lines* (**D** and **E**). The *black cross* in the center of the region indicates the conditions used for PAO and PAB in this work. 70

4.9 Adapted from Figure 4.7, average over the interval 1994 to 2021 as a function of strahl identification criteria, PAO and PAB. Panels show: **A**) Inverted, **B**) Uninverted, **C**) Counterstreaming and **D**) Undetermined flux percentages. On each plot, the lines correspond to criteria outlined in Figure 4.8. 72

4.10 Adapted from Figure 4.6, a single CR of ACE observations from 23rd October to 19th November 2008. **A**) the suprathermal electron pitch angle distribution function ($f(v, \theta)$, units s^{3}cm^{-6}), normalized to the maximum and minimum flux at each time step. **B**) the PAB at 0^o PA (*black line*) and 180^o PA (*red line*), and the minimum PAB value of 45% (*blue line*). **C**) the PAO at 0^o PA (*black line*) and 180^o PA (*red line*), and the minimum PAO value of 140% (*blue line*). **D**) the radial magnetic field (nT) in GSE coordinates. **E**) topology indicator of the magnetic field indicating whether the flux is: open (*+1*), CS (*+2*), inverted (*-1*), unclassified/disconnected (*-2*). *0* indicates there is missing data. . . . 73

4.11 Selecting strahl identification criteria. (a) Average OSF over the interval 1994 to 2021 as a function of strahl identification criteria, PAO and PAB. (b) Values of PAO and PAB that are consistent with four previous studies: Gosling et al. (1992) (*red and blue lines* corresponding to ACE and *Wind*, respectively), Anderson et al. (2012) (*magenta line*), Skoug et al. (2000) (*black lines*) and Pagel, Crooker and Larson (2005) (*yellow horizontal lines*). The variation in OSF within the remaining PAO-PAB parameter space is very small. 74

5.1 Time series of OSF estimates over the period of study. The *red line* shows the OSF calculated using Equation 5.1, which does not include the correction for inverted flux. The *black line* shows the OSF calculated using Equation 5.2, which includes the correction for inverted flux. . . . 85

5.2 Time series of OSF estimates over the period of study. The *red line* shows the OSF calculated using Equation 5.6, which assumes that the same proportion of all other topologies makes up the unclassified flux. The *black line* shows the OSF calculated using Equation 5.2, which assumes the unclassified flux is a proxy for disconnected flux. 86

5.3 Time series of OSF estimates and the "actual error" over the period of study. The top panel shows the OSF calculated using Equation 5.2 using data from ACE (*red line*) and *Wind* (*black line*) for CRs where ACE has more than 95 % of data available. The bottom panel shows the "actual error" for each CR from the top panel. 87

5.4 The effect of data gaps on OSF estimate. (a) The percentage error in OSF with changing data availability. The "actual errors" (*black crosses*), are given by direct comparison of simultaneous ACE and *Wind* data. Ranges for the 5th/95th (*blue*), 25th/75th (*red*), and 33rd/66th (*black*) percentiles of "predicted errors" are obtained by applying *Wind* data gaps for a given Carrington rotation to the whole 27-year dataset. (b) "Actual errors" binned in 5 % intervals of data availability (*black crosses*) with a best-fit polynomial (black line). Three *red boxes* highlight points for further study. 88

5.5 The CR of data corresponding to highlighted point 1 in Figure 5.4a. **Ai**) from ACE, the suprathermal electron pitch angle distribution function ($f(v, \theta)$, units s^{3}cm^{-6}), normalized to the maximum and minimum flux at each time step. **Aii**) from ACE, the radial magnetic field (nT) in GSE coordinates. **Bi**) from *Wind*, the suprathermal electron differential flux (EDF), units cm^{-2}ster^{-1}eV^{-1}s^{-1}), normalized to the maximum and minimum flux at each time step. **Aii**) from *Wind*, the radial magnetic field (nT) in GSE coordinates. **C**) combined (ACE in *red* and *Wind* in *black*) topology indicator of the magnetic field indicating whether the flux is: open (*+1*), CS (*+2*), inverted (-*1*), unclassified/disconnected (-*2*). *-3* indicates there is missing data. 89

5.6 The CR of data corresponding to highlighted point 2 in Figure 5.4a. **Ai**) from ACE, the suprathermal electron pitch angle distribution function ($f(v, \theta)$, units s^{3}cm^{-6}), normalized to the maximum and minimum flux at each time step. **Aii**) from ACE, the radial magnetic field (nT) in GSE coordinates. **Bi**) from *Wind*, the suprathermal electron differential flux (EDF), units cm^{-2}ster^{-1}eV^{-1}s^{-1}), normalized to the maximum and minimum flux at each time step. **Aii**) from *Wind*, the radial magnetic field (nT) in GSE coordinates. **C**) combined (ACE in *red* and *Wind* in *black*) topology indicator of the magnetic field indicating whether the flux is: open (*+1*), CS (*+2*), inverted (-*1*), unclassified/disconnected (-*2*). *-3* indicates there is missing data. 90

5.7 The CR of data corresponding to highlighted point 3 in Figure 5.4a. **Ai**) from ACE, the suprathermal electron pitch angle distribution function ($f(v, \theta)$, units s^{3}cm^{-6}), normalized to the maximum and minimum flux at each time step. **Aii**) from ACE, the radial magnetic field (nT) in GSE coordinates. **Bi**) from *Wind*, the suprathermal electron differential flux (EDF), units cm^{-2}ster^{-1}eV^{-1}s^{-1}), normalized to the maximum and minimum flux at each time step. **Aii**) from *Wind*, the radial magnetic field (nT) in GSE coordinates. **C**) combined (ACE in *red* and *Wind* in *black*) topology indicator of the magnetic field indicating whether the flux is: open (*+1*), CS (*+2*), inverted (*-1*), unclassified/disconnected (*-2*). *-3* indicates there is missing data. 91

5.8 An example of the application of data gaps from *Wind* to ACE CRs where there is more than 95 % data availability. **A**) 3 CRs of ACE data, showing the suprathermal electron pitch angle distribution function ($f(v, \theta)$, units s^{3}cm^{-6}), normalized to the maximum and minimum flux at each time step. **B**) single CR of *Wind* data with data gaps, showing the suprathermal electron differential flux (EDF), units cm^{-2}ster^{-1}eV^{-1}s^{-1}), normalized to the maximum and minimum flux at each time step. **C**) same 3 CRs of ACE data from **A** with the data gaps from **B** applied to each CR of data. 92

5.9 As in Figure 5.4a, the percentage error in OSF with changing data availability. The “actual errors” (*black crosses*), are given by direct comparison of simultaneous ACE and *Wind* data. Ranges for the 5th/95th (*blue*), 25th/75th (*red*), and 33rd/66th (*black*) percentiles of “predicted errors” are obtained by applying *Wind* datagaps for a given Carrington rotation to the whole 27-year data set. A more specific portion of Figure 5.4a is shown, with two error bars highlighted for further study. 93

5.10 The CRs of *Wind* data corresponding to highlighted error bars in Figure 5.9. Both panels show a single CR of *Wind* data with different sized data gaps, showing the suprathermal electron differential flux (EDF), units cm^{-2}ster^{-1}eV^{-1}s^{-1}), normalized to the maximum and minimum flux at each time step. **A**) CR of data corresponding to the first, larger error bar in Figure 5.9. **B**) CR of data corresponding to the second, smaller error bar in Figure 5.9. 94

5.11 Time series of OSF estimates over the period of study. (a) The individual ACE (*red line*) and *Wind* (*blue line*) OSF estimates. The *black line* shows the best estimate derived from taking the highest data coverage on a CR by CR basis (b) The best estimate of OSF (*black line*) with error bars computed from the available data coverage. 95

5.12 OSF yearly time series from different time averages of B_r used in the standard OSF calculation (i.e., $\Phi_R = 4\pi R^2\langle|B_r|\rangle$). The *shaded regions* display the different time averages of $|B_r|$ between 1-100 hours. The *red line* shows the best estimate of OSF calculated from the Strahl method. A 20-hour time average of B_r provides the closest agreement. 96

5.13 Comparisons of OSF calculated via the standard method ($\Phi_R = 4\pi R^2\langle|B_r|\rangle$) computed using 20-hour averages of $|B_r|$ with the best estimate from the Strahl method. (a) A scatter plot of yearly averages. The *solid black line* shows $y = x$, and the *dashed black line* is a linear best fit. (b) A scatter plot of CR averages. (c) A histogram of the percentage errors between the Strahl method and Φ_R computed with 20-hour averaged data for yearly intervals, where a positive error signifies an overestimation. (d) The same as *panel c*, but for CR intervals. 99

5.14 Comparison of *in-situ* and photospheric magnetogram estimates of OSF. The best estimate from the current study is shown in *black* with errors as the *grey shaded region*, which is displayed as CR averages. The *dashed magenta line* shows the OSF calculated from Owens et al. (2017), also as CR averages. The *dashed pale blue line* shows the OSF calculated from $\Phi_{R=1\mathrm{AU}}$. The *coloured lines* are magnetogram estimates from KPVT (*red line*), ADAPT (*orange line*), EUV (*cyan line*), Harvey (*blue line*), displayed as 3 CR averages, from Wallace et al. (2019). 100

6.1 Schematic of the heliospheric current sheet from Smith (2001). The shaded region is the current sheet separating the opposite magnetic fields of "Toward" and "Away" topology. 102

6.2 Figure from Genestreti et al. (2012) showing the geometry of magnetic reconnection. The red and blue lines illustrate magnetic field lines of opposite polarity. 104

6.3 Figure adapted from Owens et al. (2011) showing the reconnection of opposite field lines to produce disconnected flux and inverted flux. The top panel shows the reconnection between open field lines which results in disconnected flux. The bottom panel shows the reconnection between open and closed field lines which does not produce disconnected flux. Instead, the field is locally inverted before straightening further into the heliosphere. 105

6.4 Polarity indicator for 5 days of data from 10th-15th June 2008. The *black line* is the hourly smoothed polarity indicator (+1 = toward, -1 = away), the *red line* is the smoothed polarity indicator showing the ± 0.5 minimum values to identify dominantly away/toward sectors, and the *blue crosses* show the location of polarity reversals. 107

6.5 An example of the polarity indicator and B_r for 5 days of data from 10th-15th June 2008. (Top) The *black line* is the hourly smoothed polarity indicator ($+1 =$ toward, -1 $=$ away), the *red line* is the smoothed polarity indicator showing dominantly away/toward sectors, and the *blue crosses* show the location of polarity reversals. (Bottom) The *black line* is the 128s radial magnetic field, the *red line* is an hour running smooth of B_r, and the *blue crosses* show the location of the sign change in the hourly smoothed B_r. 109

6.6 An example of the polarity indicator and B_r for 5 days of data from 9th-14th November 2014. (Top) The *black line* is the hourly smoothed polarity indicator ($+1 =$ toward, -1 $=$ away), the *red line* is the smoothed polarity indicator showing dominantly away/toward sectors, and the *blue crosses* show the location of polarity reversals. (Bottom) The *black line* is the 128s radial magnetic field, the *red line* is an hour running smooth of B_r, and the *blue crosses* show the location of the sign change in the hourly smoothed B_r. 110

6.7 An example of the polarity indicator and B_r for 10 hours of data from 14th June 2008. (Top) The *black line* is the hourly smoothed polarity indicator ($+1 =$ toward, -1 $=$ away), the *red line* is the smoothed polarity indicator showing dominantly away/toward sectors, and the *blue crosses* show the location of polarity reversals. (Bottom) The *black line* is the 128s radial magnetic field, the *red line* is an hour running smooth of B_r, and the *blue crosses* show the location of the sign change in the hourly smoothed B_r. 111

6.8 An example of the polarity indicator and B_r for 3 days of data from 20th-23rd August 2005. (Top) The *black line* is the hourly smoothed polarity indicator ($+1 =$ toward, -1 $=$ away), the *red line* is the smoothed polarity indicator showing dominantly away/toward sectors, and the *blue crosses* show the location of polarity reversals. (Bottom) The *black line* is the 128s radial magnetic field, the *red line* is an hour running smooth of B_r, and the *blue crosses* show the location of the sign change in the hourly smoothed B_r. 112

6.9 Superposed epoch plots of B_r at true polarity reversals. For this example, a subset of data of positive to negative crossing was selected. (Left) two random constituent B_r signatures (*grey lines*) and (Right) the B_r average signature (*red line*). Daily running averages are employed, and true polarity reversals are used as zero epochs. The shaded region shows the area between the 5th/95th percentiles (*black dashed lines*) of the background conditions, found by Monte Carlo sampling as described in Section 6.2.4. 113

6.10 Superposed epoch plots of (a) inverted, (b) uninverted (open), (c) counterstreaming, and (d) unclassified flux percentages, and (e) |B|, (f) |v|, (g) $\mathrm{N}_a/\mathrm{N}_p$, and (h) N_p at true polarity reversals for all 3210 HCS crossings between 1994-2021. Daily running averages are employed, and true polarity reversals are used as zero epochs. The shaded region shows the extent of the standard error of the mean (black dashed line). 114

6.11 The effect of solar cycle on HMF topology about the HCS. Superposed epoch plots of inverted (column a), uninverted (column b), counter-streaming (column c), and unclassified (column d) flux percentages at true polarity reversals. Daily running averages are employed, and true polarity reversals are used as zero epochs. The rows correspond to the use of all data (i), solar minimum (ii), solar maximum (iii), rising phase (iv), and declining phase (v). The shaded region shows the extent of the standard error of the mean (black dashed line). 120

6.12 Effect of solar cycle on solar wind properties about the HCS. Superposed epoch plots of |B| (column a), |v| (column b), N$_a$/N$_p$ (column c), and N$_p$ (column d) at true polarity reversals. Daily running averages are employed, and true polarity reversals are used as zero epochs. The rows correspond to the use of all data (i), solar minimum (ii), solar maximum (iii), rising phase (iv), and declining phase (v). The shaded region shows the extent of the standard error of the mean (black dashed line). . . . 121

6.13 Top panel shows the daily sunspot number variation. The bottom panel shows the CR occurrence of true polarity reversals with a 13 CR running mean (*red line*). 122

6.14 Number of true polarity reversals over the full 1994-2021 (364 CRs) data set with increasing smoothing interval. 122

6.15 Schematic of the transport of open flux resulting from differential rotation of the photosphere, taken from Owens et al. (2011). The top panel shows the rotation speed of the photosphere compared to the corona, which rotates rigidly at the same speed as the midlatitude photosphere. At high latitudes, point a, the corona moves ahead of the photosphere, and flux tubes become longitudinally sheared. Reconnection between open flux and small-scale loops occurs to reduce shear, with open flux foot points "slipping" ahead of the photospheric magnetic field (in the direction of the dashed black arrow). At midlatitudes, point b, reconnection between open flux and small loops occur randomly, resulting in no net motion. At lower latitudes, point c, the photosphere moves ahead of the corona. Open flux is sheared and the open flux foot points move opposite to point a (in the direction of the dashed black arrow). 123

6.16 Schematic of the transport of open flux at an inclined HCS, taken from Owens et al. (2011). The red and blue colours represent the opposite magnetic field polarities, which are separated by an inclined HCS shown as a solid black line. Here the "slipping" of flux tubes (1st panel) force together open flux of opposite polarity (2nd panel). Reconnection between these flux tubes results in a disconnected loop (3rd panel) which will propagate out with the solar wind, reducing the OSF (4th panel). . 124

7.1 Panel (a) shows the radial evolution of the density profiles in the slow solar wind, from Stverak et al. (2009). Panel (b) shows the same slow solar wind radial evolution in intensity from the Ulysses data set. . . . 132

Chapter 1

Introduction

The Sun's open solar flux (OSF) is the component of the Sun's magnetic field that reaches a sufficient height above the visible solar surface (the photosphere) to be dragged into the heliosphere by the solar wind. Since the solar wind is the only stellar wind that we are able to observe, it presents the opportunity to understand the environment of other stars as well as our Sun.

Most of the Sun and its outer atmosphere, the corona, which evolves into the outflowing solar wind, are highly ionised gases, otherwise termed "plasmas". Plasmas form when a gas is heated sufficiently for the atoms to lose one or more electrons. They can also be formed by irradiation by electromagnetic waves of short enough wavelength (high enough energy) to knock an electron out of the atoms. To understand their behaviour and evolution it is necessary to first briefly review some of the fundamentals of plasma physics. Being ionised, plasmas contain charged particles that generate electric and, when they move, magnetic fields, which in turn affect the motion of the charged particles. Electromagnetism describes the motion of individual charged particles and magnetohydrodynamics considers the collective behaviour of a plasma as a fluid. Magnetic reconnection is a common phenomenon in space (and laboratory) plasmas and is important in the context of this thesis as it changes the magnetic fields being dragged out by the solar wind, therefore affecting the OSF.

This chapter sets the scene for the thesis, covering some of the background physics for the research that will be presented. Chapter 2 will provide an overview of the methods of measuring the OSF and the discrepancy between them. In Chapter 3 the instruments and data sets used in the studies presented are introduced, as well as some necessary pre-processing of the data. Chapters 4 - 6 present the scientific analysis carried out for this thesis. In Chapter 7 the work will be summarised and the future directions the work could take are discussed.

1.1 Single-Particle Motion

A plasma is an ionised gas made up of roughly equal numbers of ions (usually protons) and electrons which exhibit a collective behaviour and an overall zero net charge (e.g. Meyer-Vernet, 2007). Because a plasma is quasi-neutral electrically, for a single species of positive ion, the number density of ions is very close to that of electrons. Single-particle motion makes assumptions to avoid the collective effects in a plasma. The plasma is required to have a strong external magnetic field (the contributions to the magnetic fields by the particles considered are considered negligible) and a low density (such that collisions are negligible).

In a region of no electric field and a static magnetic field, **B**, a single charged particle of charge q and mass m moving only perpendicular to the direction of the magnetic field will result in a circular motion with an angular frequency, called the gyrofrequency ω_g:

$$\omega_g = \frac{|q|B}{m} \tag{1.1}$$

with radius of gyration r_g:

$$r_g = \frac{mv_\perp}{|q|B} \tag{1.2}$$

where $v_\perp$ is the velocity of the particle perpendicular to the magnetic field. Note the notation used here that B is the magnitude of the vector **B**.

When viewing the system with the magnetic field directed towards the observer, positively charged particles gyrate clockwise while negatively charged particles gyrate anticlockwise. Particles that have a velocity with both field parallel and perpendicular velocity components follow a spiral path along the magnetic field. The pitch angle, α, of the particle is the angle between the velocity components perpendicular and parallel to the magnetic field.

$$\alpha = \mathrm{arctan}\frac{v_{\perp}}{v_{\parallel}} \tag{1.3}$$

where $v_{\parallel}$ is the velocity of the particle parallel to the magnetic field.

A charged particle (charge q) in the presence of an electric field $\mathbf{E}$, but in the absence of a magnetic field, experiences a force called the Coulomb force $\mathbf{F}_C$ where:

$$\mathbf{F}_C = q\mathbf{E} \tag{1.4}$$

If the charged particle is in motion with a velocity $\mathbf{v}$ and a magnetic field is present, it will experience a force known as the Lorentz force $\mathbf{F}$:

$$\mathbf{F} = q(\mathbf{E} + \mathbf{v} \times \mathbf{B}) \tag{1.5}$$

Note that if the magnetic field is absent, $B = 0$ and the Lorentz force $\mathbf{F}$ reduces to $\mathbf{F}_C$.

1.2 Basic plasma physics

An ideal plasma is quasi-neutral, meaning the plasma would have an overall zero net charge. This condition is met by the typical length scales of the plasma (L) being large enough that any local deviations in charge density can be shielded from the rest of the plasma by the large number of particles.

For each charged particle in a plasma, the electric field must be cancelled out by other charges. An isolated particle (of charge q) gives an electric potential of

$$\phi_C = \frac{q}{4\pi\varepsilon_0 r} \tag{1.6}$$

at a distance r from the particle where ε_0 is the permittivity of free space. This is known as the Coulomb potential. The other particles in the plasma respond to make the plasma electrically neutral by shielding this potential. Theory shows that potential then becomes the Debye potential:

$$\phi_D = \frac{q}{4\pi\varepsilon_0 r} \exp\left(-\frac{r}{\lambda_D}\right) \tag{1.7}$$

where λ_D is a characteristic length scale, the Debye length, which is given by

$$\lambda_D = \left(\frac{\varepsilon_0 k_B / {q_e}^2}{N_e/T_e + \Sigma_j {z_j}^2 N_j/T_j}\right)^{0.5} \tag{1.8}$$

where k_B is Boltzmann's constant, q_e is the electronic charge, N_e the electron number density, T_e the electron temperature, and j is the sum is over all ion species, which have charge $z_j|q_e|$, number density N_j and temperature T_j.

The ion terms are only important in very low-temperature plasmas and so are usually neglected, giving

$$\lambda_D = \left(\frac{\varepsilon_0 k_B T_e}{N_e {q_e}^2}\right)^{0.5} \tag{1.9}$$

The Debye length is the radius of the sphere of influence of an individual charged particle, outside of which its charge is effectively screened by the other parameters. For a quasi-neutral plasma, the typical length scale of the plasma needs to be much larger than the Debye length ($L \gg \lambda_D$) for a plasma to be treated as a collective fluid. In the solar wind, the Debye length is around 1m, while in the solar corona, it is a few cm (Russell, 2003).

1.2.1 Electromagnetism

The motions of charged particles and the associated electric and magnetic fields are described by Maxwell's equations, presented in Maxwell (1864). In fact, very few scientists would recognise Maxwell's original equations which were 20 in number and were reduced to the elegant 4 equations that we know today by Oliver Heaviside. Heaviside's work was originally only in unpublished notes and short articles written between 1891 and 1912 that were brought together into a single book in 2003 (Heaviside, 2003). A recent condensation of the derivation has been presented by Hampshire (2018).

In differential form (they can all be expressed in integral form), these 4 equations are:

$$\nabla \cdot \mathbf{E} = \frac{\rho}{\varepsilon_0} \tag{1.10}$$

$$\nabla \cdot \mathbf{B} = 0 \tag{1.11}$$

$$\nabla \times \mathbf{E} = -\frac{\partial \mathbf{B}}{\partial t} \tag{1.12}$$

$$\nabla \times \mathbf{B} = \mu_0 \left(\mathbf{J} + \varepsilon_0 \frac{\partial \mathbf{E}}{\partial t} \right) \approx \mu_0 \mathbf{J} \tag{1.13}$$

where $\mathbf{J}$ is the free current density and ρ is the net charge density. Note that in a plasma there are only free charges and so the second term on the right of equation 1.13 (the displacement current carried by the polarisation of atoms/molecules containing bound charges) is negligible compared to the free current, $\mathbf{J}$.

Equation 1.10 is known as Gauss' law and states that the electric flux through any closed surface is proportional to the net electric charge enclosed by the surface, which explains the conservation of charge. Equation 1.11 is Gauss' law for magnetism, which states that the magnetic flux across any closed surface is zero. This law is consistent with the observation that magnetic monopoles do not exist. Equation 1.12 is Faraday's law, which states that a time-varying magnetic field will always accompany a spatially varying electric field, with the opposite also being true. Without the displacement current, equation 1.13 is Ampère's law, which describes the way a magnetic field can be generated by currents carried by free charges.

1.2.2 Magnetohydrodynamics

Instead of considering the individual particles in a plasma, it can be considered as a fluid. Magnetohydrodynamics (MHD) is the study of electrically conducting fluid in the presence of electromagnetic fields (Alfvén, 1942). MHD equations combine Maxwell's equations and the Navier-Stokes equations. Ohm's law closes the system of equations.

$$\mathbf{E} + \mathbf{v} \times \mathbf{B} = \eta \mathbf{j} + \frac{1}{ne}(\mathbf{j} \times \mathbf{B}) - \frac{1}{ne}(\nabla \cdot \mathbf{P}_e) + \frac{m_e}{ne^2}\frac{\partial \mathbf{J}}{\partial t} \tag{1.14}$$

Equation 1.14 is the generalised Ohm's law, where η is the resistivity of the plasma, n is the number density, e is the electron charge, m_e is the electron mass, **J** is the current density, and $\mathbf{P}_e$ is electron pressure. On the right-hand side of the equation, the terms are: the resistive term, the Hall-current term, the anisotropic electron pressure term, and a time-dependent term associated with the contribution of electron inertia to the current flow. Ohm's law can be simplified when the 2nd, 3rd, and 4th terms are sufficiently small that they can be ignored (which is true in the solar wind). The simplified Ohm's law derived by neglecting these terms is:

$$\mathbf{j} = \sigma(\mathbf{E} + \mathbf{v} \times \mathbf{B}) \tag{1.15}$$

where $\sigma (= 1/\eta)$ is the electrical conductivity. Substituting in Faraday's law and Ampère's law results in the induction equation:

$$\frac{\partial \mathbf{B}}{\partial t} = \nabla \times (\mathbf{V} \times \mathbf{B}) + \frac{1}{\mu_0 \sigma}\nabla^2 \mathbf{B} \tag{1.16}$$

The first term on the right is the convective term ($\nabla \times (\mathbf{V} \times \mathbf{B})$) and the second term is the diffusive term ($\frac{1}{\mu_0 \sigma}\nabla^2 \mathbf{B}$). The ratio between these two terms determines which is dominating the evolution of the field. This is the magnetic Reynolds number:

$$R_m = \frac{|\nabla \times (\mathbf{V} \times \mathbf{B})|}{|\frac{1}{\mu_0 \sigma} \nabla^2 \mathbf{B}|} \tag{1.17}$$

Taking orders of magnitude of the terms of this equation we get:

$$R_m \sim \mu_o \sigma V_c L_c \tag{1.18}$$

where V_c is the characteristic speed and L_c is the characteristic scale length of the plasma.

If $R_m \ll 1$, diffusion dominates over convection, the magnetic field will diffuse through the plasma. If $R_m \gg 1$, the convective term dominates, and in this limit the field and plasma are coupled together ('frozen-in') in the sense that the field moves with the plasma velocity, $\mathbf{V}_p$, which is the weighted mean of the bulk flow velocities of the ion and electron gases, $\mathbf{V}_i$ and $\mathbf{V}_e$ respectively) weighted by their mass (the mean ion mass, m_i and the electron mass, m_e):

$$\mathbf{V}_p = \frac{m_e \mathbf{V}_e + m_i \mathbf{V}_i}{m_e + m_i} \tag{1.19}$$

Packets of plasma on a given magnetic field line will follow and be confined to that field line. For example, in the solar corona, R_m is of the order $10^8 - 10^{12}$ (Hood and Hughes, 2011) and so the frozen-in flux theorem generally applies. Moving from the corona into the heliosphere, characteristic spatial scales L_C generally increase and hence so, in general, will R_m values. Hence frozen-in applies in most of the corona and heliosphere. However, there are small regions of magnetic shear (current sheets) in the corona and the heliosphere where the spatial scale is small, and in these regions we expect breakdowns in the frozen-in because R_m is small, and even approaches unity, making diffusion important.

1.2.3 Magnetic Reconnection

Magnetic reconnection is a change in the topology of the magnetic field. Here two plasma populations that are confined to separate field lines by 'frozen-in' flux are able to mix (Baumjohann and Treumann, 1996, Hesse and Cassak, 2020). The breakdown of frozen-in occurs because at current sheets the spatial scales in magnetic field structure are small making L_c and R_m small and diffusion becomes important.

Figure 1.1 shows a schematic of the basic reconnection process. The two plasma populations have opposite magnetic field directions (first panel). These two populations are brought together by diffusion until a topology change can take place and the fields that are not initially connected (being aligned to the current sheet) become interconnected and thread the current sheet (middle panel). In the final panel, the magnetic field lines have a new topology.

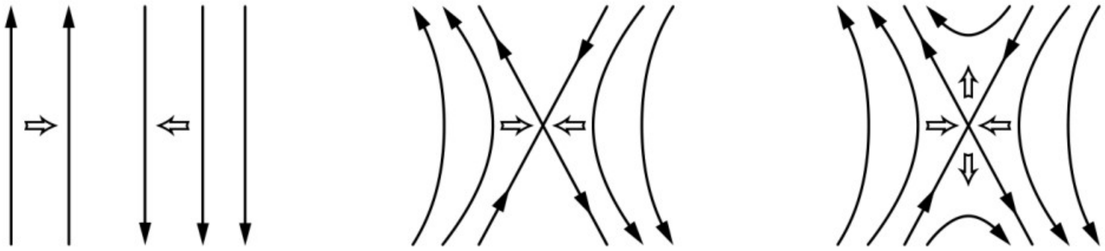

Figure 1.1: Schematic from Baumjohann and Treumann (1996) showing the simplified geometry of magnetic reconnection.

Note that there are "separatrices" that divide the inflow and outflow regions in which the field has both the initial along-the-current-sheet topology and the final threading-the-current-sheet topology. The highly bent field lines produced by reconnection are subject to an MHD force often called the "magnetic tension force", which acts to straighten bent field lines. This results in plasma jets and frozen-in fields being ejected along the current sheet. The process of magnetic reconnection can be self-driven, as the ejection of plasma jets brings in more plasma which brings more magnetic fields to undergo reconnection. However, it also often occurs in bursts. This process plays a key role in many phenomena, such as: coronal heating, flares, and CMEs. It is also critical to the coupling of solar wind energy into the Earth's magnetosphere and was indeed first developed in this context by Dungey (1961), Lockwood (2016).

1.3 The Sun

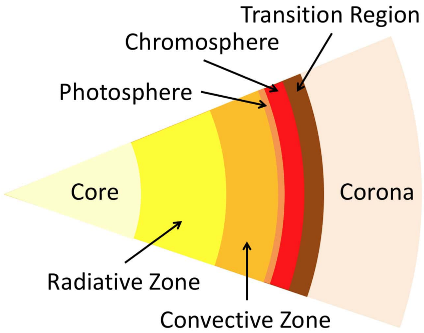

Figure 1.2: Schematic of the internal structure of the Sun. From the centre to the outer atmosphere, the Sun consists of: core (*pale yellow*), radiative zone (*yellow*), convective zone (*orange*), photosphere (*orange-red*), chromosphere (*red*), transition region (*brown*), and the corona (*cream*). (Image from NICT, the National Institute of Information and Communications Technology).

The Sun is a star made primarily of hydrogen and helium, with a mass of 2.0×10^{30} kg and a radius of $\sim 7 \times 10^5$ km (e.g. Meyer-Vernet, 2007). The Sun has multiple layers in its interior and atmosphere, shown in Figure 1.2. At the centre of the Sun is the core, where a temperature of 15 million degrees Celsius and a high density (150 g/cm^3, about 10 times the density of gold) enables nuclear fusion to take place, providing the energy to support the Sun (Zeilik, 2002). Beyond the core is the radiative zone (RZ), through which energy is carried away from the core by photons. The photons are repeatedly absorbed and re-radiated and so, although the photons travel at the speed of light, this radiative transfer process takes of order 100,000 years to transfer energy across the RZ. The temperature in the RZ drops to 2 million °C at its outer edge and the density drops to 0.2 g/cm^3 (less than the density of water). Beyond the radiative zone is the convective zone (CZ), the final layer of the Sun's interior. Here the energy transport switches from radiation to convection, with large circulation cells of various scales bringing the energy to the surface of the Sun (the photosphere) where the temperature drops to 5700K (Hathaway, 2022). The lower temperature of the photosphere means that it is primarily made up of neutral atoms with only a very low ionisation content. The ionisation potentials associated with changes in ionisation state drives convection cells in the CZ, acting in a way that is analogous to the role of latent heat associated with phase changes of water in driving thunderstorm convection cells in Earth's atmosphere. At the base of the convection zone is the tachocline where the solid rotation of the RZ changes to the differential (latitude-dependent) rotation of the convection zone. The Coriolis force means that the differential rotation generates meridional flow with poleward motion near the photosphere and return equatorward flow deeper into the solar interior. The plasma flows in the CZ generate the solar magnetic field through a dynamo process (for more detail see Charbonneau, 2020). The field is thought to be stored in an "overshoot layer" below the tachocline but when it gets large enough can bubble up under buoyancy forces through the CZ and erupt through the photosphere giving active sunspot regions.

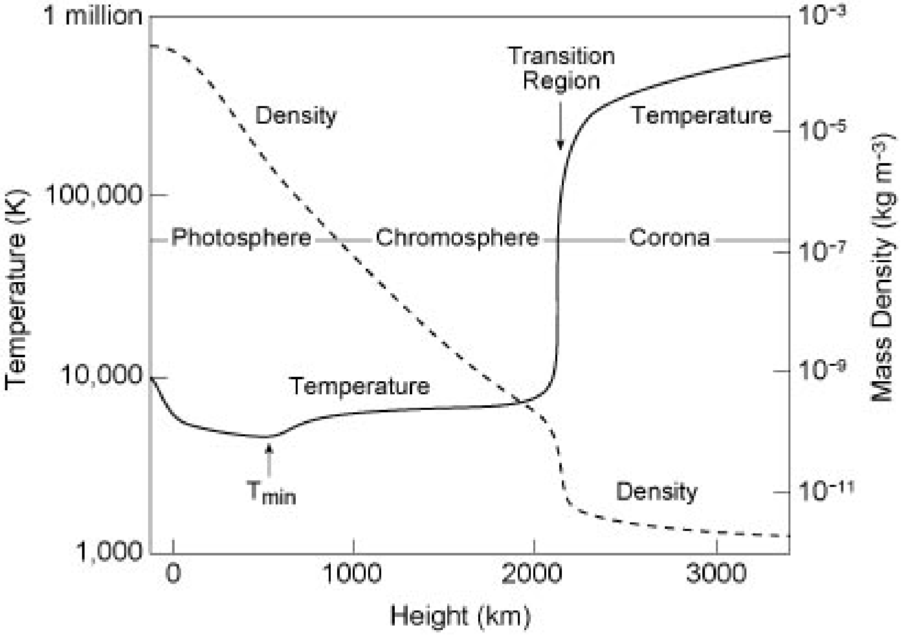

Figure 1.3: Average temperature and density of the quiet Sun where zero is the solar surface at one solar radius. Plot taken from de Patoul (2012).

The photosphere is the visible surface of the Sun, with a 100km thickness. Here the density and opacity are low enough that light is able to escape. The surface away from sunspot regions appears bubbly due to the convection of material in the layer below, referred to as granulation (Kutner, 2003). Above the photosphere sits the chromosphere, a transparent layer with a thickness of 200km. Here the temperature rises from 6000°C to about 20,000°C. Between the chromosphere and the corona, sits the transition region where the temperature rapidly increases, as shown in Figure 1.3, from 20,000°C to 1 million °C over a very short distance of 100km (Hathaway, 2022). The corona is the outermost layer of the Sun's atmosphere, with a low density and extremely high temperature. The mechanisms by which energy is transferred to heat the plasma in the corona to these high temperatures are still unknown and our lack of knowledge about the heating mechanism is referred to as the "coronal heating problem". Unlike the differentially rotating photosphere, the corona broadly rotates as a whole with the solar magnetic field that orders it. Finally, the solar wind is the non-static extension of the solar atmosphere, which is discussed further in Section 1.4.

1.3.1 Solar Cycle

The solar dynamo generates the Sun's magnetic field, which yields sunspots, and so drives the 11-year solar cycle. The cycle was discovered based on the quasi-periodic variation of sunspot numbers by Schwabe (1844), shown in Figure 1.4. Figure 1.5 shows the positions of sunspots for each rotation of the Sun. Sunspots appear in two latitude bands on either side of the equator. At the start of the solar cycle, sunspots emerge at high latitudes, before migrating toward the equator throughout the cycle. During the cycle, new sunspots form at lower latitudes than earlier in the cycle.

As first noted by Hale and Nicholson (1925), the magnetic polarity of leading sunspots reverses on average every 11 years (although it can vary between 9 and 14 years), making a complete solar magnetic cycle around 22 years long (e.g. Owens et al., 2015). Because the magnetic field emerges through the photosphere in loops from the CZ, sunspots mainly occur in pairs of opposite polarity (magnetic north and south),

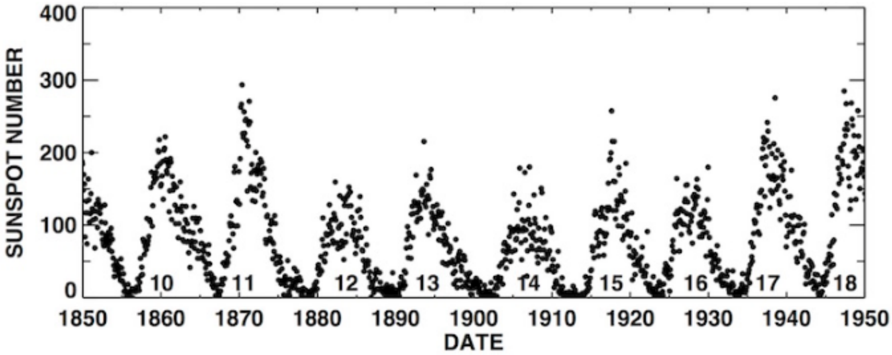

Figure 1.4: Plot from Hathaway (2017) showing the monthly averages of the sunspot numbers.

with one of the pair "leading" as the Sun rotates. In one cycle, most leading spots will be magnetic north in the northern hemisphere, and in the next cycle, most of the leading sunspots will be magnetic south in the northern hemisphere (Zeilik, 2002, Kutner, 2003). This is also true for leading sunspots in the southern hemisphere. The polarity of the leading/trailing spots depends on the direction of the azimuthal component of the field in the CZ, which is in the opposite direction in even-numbered solar cycles to that in odd-numbered cycles. The 11-year cycle appears in most solar phenomena and is found in almost all historic solar records. This demonstrates the existence of a timing engine in the Sun which controls or influences all aspects of solar phenomena (Balogh et al., 2014).

1.3.2 Coronal Holes

Coronal holes are open magnetic field regions that appear as dark areas in X-ray and EUV images of the Sun (Wang et al., 1996). Figure 1.6 shows an example of a coronal hole measured with different wavelengths. The coronal hole is darkest in the 193 Å and 211 Å, which are both in the EUV part of the electromagnetic spectrum.

Coronal holes are sources of fast solar wind (typical speeds around 750km s^{-1}). They appear dark in EUV because they are cooler, and less dense than the surrounding coronal plasma. They are regions of open, unipolar magnetic fields, which allow the solar wind to escape into the heliosphere. Near solar minimum, the Sun's poles are

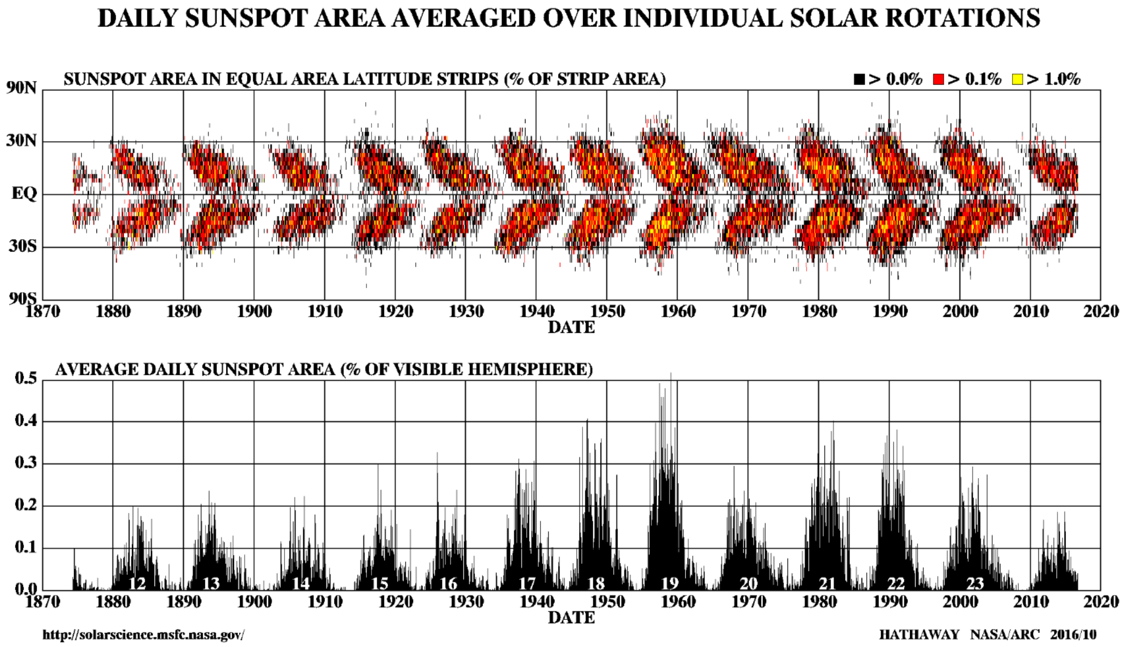

Figure 1.5: Plot from Hathaway (2017) showing the butterfly diagram (top panel), which is the distribution of sunspots with latitude. The bottom panel shows the fractional coverage of sunspots as a function of solar latitude and time.

dominated by large coronal holes with persistent fast wind streams (Wang et al., 1996). At solar maximum, the magnetic field polarity around the poles goes through a reversal, and the polar coronal holes disappear and smaller ones appear throughout the disc (Meyer-Vernet, 2007). The reversal of the polar coronal holes is related to the reversal of leading sunspot polarities in the Hale cycle.

1.3.3 Coronal Mass Ejections

Coronal mass ejections (CMEs) are ejections of plasma from the corona into the heliosphere. Figure 1.7 shows an example of a CME observed by a coronagraph (an imager with an occulting disc that acts in the same way as the moon during an eclipse and allows us to see the solar corona). CMEs eject billions of tonnes of coronal matter and they carry magnetic flux that is stronger than the background solar wind interplanetary magnetic field (Kahler, 1992). Various scenarios have been proposed, but all invoke the idea that CMEs are the result of magnetic reconnection between rising flux ropes

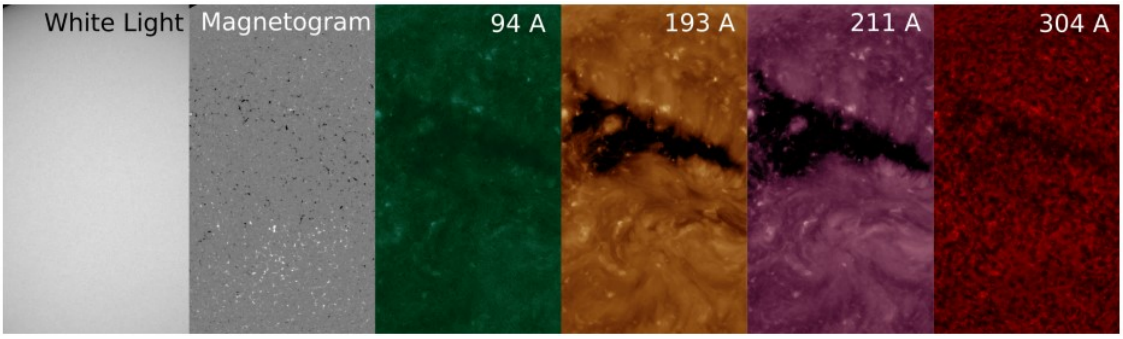

Figure 1.6: A coronal hole in different wavelengths and in a magnetogram from Macneil (2018). The 2 left panels are from SDO-HMI and the 4 right panels are from SDO-AIA with the wavelengths labelled on each panel.

near the solar surface and typically originate from eruptions in active regions. CMEs are visible in coronagraphs off the solar limb out to many solar radii, $R_\odot$, and are responsible for the most damaging disturbances associated with space weather (Meyer-Vernet, 2007). Space weather is the umbrella term used to describe solar phenomena that can have major impacts on terrestrial life and infrastructure.

1.3.4 Flares

Flares are typically associated with CMEs, although they are not necessarily caused by CMEs as the nature of their relation is variable and still debated. A flare is defined as a sudden, rapid, and intense variation in brightness. A flare occurs when magnetic energy built up from twisted magnetic fields in the solar atmosphere is suddenly released (Zeilik, 2002). The initial energy release is dominated by the acceleration by high energy particles, which are detected from their hard x-ray, gamma-ray, and radio signatures (Schrijver and Siscoe, 2010).

Radiation from a flare is emitted across virtually the entire electromagnetic spectrum, which consists of (Norgard, 2017):

- Radio waves: 10 kHz - 300 MHz
- Microwave radiation: 300 MHz - 300 GHz
- Infrared (IR) radiation:

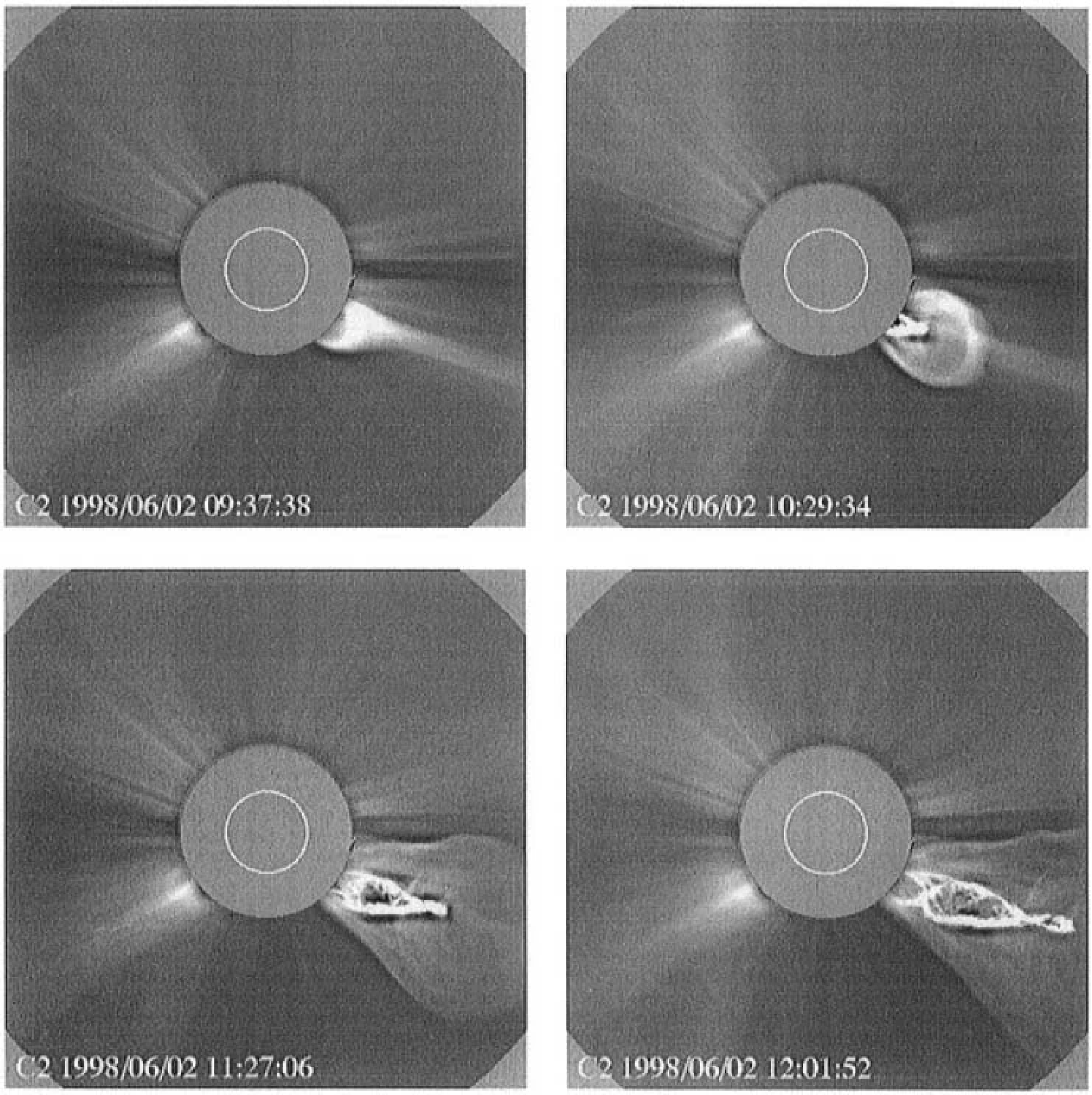
C2 1998/06/02 09:37:38
C2 1998/06/02 10:29:34
C2 1998/06/02 11:27:06
C2 1998/06/02 12:01:52

Figure 1.7: Plot from Webb and Howard (2012) showing the evolution of a CME observed by the LASCO C2 coronagraph on 2 June 1998.

  - Far IR: 1 - 42.9 THz
  - Intermediate IR: 42.9 - 100 THz
  - Near IR: 100 - 429 THz
- Visible light: 429 - 750 THz
  - Red: 429 THz
  - Green: 549 THz
  - Blue: 688 THz

- Ultraviolet (UV) radiation:
    - Near UV: $\approx$ 750 THz - 3 PHz/ $\approx 3 - 10eV$
    - Far UV: 3 - $\approx$ 30 PHz/ $\approx 10 - 100eV$
- X-ray radiation:
    - Soft X-rays: $\approx$ 3 PHz - 3 EHz/ $\approx 10eV - 10keV$
    - Far UV: 3 - $\approx$ 300 EHz/ $\approx 10keV - 1MeV$
- Gamma radiation:
    - Soft gamma rays: $\approx$ 1 - $\approx$ 100 EHz/ $\approx$ 1 - $\approx$ 300 keV
    - Hard gamma rays: $\approx$ 100 - 1000 EHz/ $\approx$ 300 keV - 1 MeV

Flares are classified by the intensity of the emission observed at 1AU. They are classified as: B (10^{-7} Wm^{-2}), C (10^{-6} Wm^{-2}), M (10^{-5} Wm^{-2}), or X (10^{-4} Wm^{-2}) (Bornmann et al., 1996). M-class and X-class flares are sufficiently large that they can cause minor to extensive radio blackouts on the side of the Earth facing the Sun. These are caused by charged electrons in the upper atmosphere temporarily disrupting the radio waves.

1.4 Solar Wind and the Heliosphere

The solar wind is the continuous supersonic outflow of plasma from the Sun's corona (Cranmer, 2019). It was first realised that the solar wind was continuous because of its observed effect on comets passing near the Sun (Biermann, 1951). The tail of a passing comet was observed to point away from the Sun with accelerations too high to be explained by radiation pressure. This led to the first physical model of a continuous outflow from the Sun which was termed the solar wind by Parker (1959).

Solar wind speeds are categorised as either slow or fast, however, there is no universal cutoff in velocity between fast and slow wind. Slow wind typically has speeds less than

450 km s^{-1} and fast wind typically has speeds around 750 km s^{-1} at 1AU (Bothmer and Daglis, 2007). Slower wind is generally cooler, more dense, and more variable than fast wind. While faster wind originates from coronal holes, slower wind emerges from around the equator.

The solar wind plasma is largely collisionless, highly conductive, and has $R_m > 1$, so the magnetic flux is frozen-in to the plasma (see Section 1.2.2). The solar wind carries the Sun's frozen-in magnetic field out into the heliosphere to form the heliospheric magnetic field. The environments of all bodies in the heliosphere are thus affected by the solar wind.

1.4.1 Models of Solar Wind Expansion

There are two primary approaches to the study of the solar wind: fluid (or hydrodynamic) and kinetic. The fluid approach views the solar wind as a flow outwards caused by the pressure imbalance between the Sun and the interstellar medium, whereas the kinetic approach views the solar wind as the evaporation of the coronal plasma (Echim et al., 2011).

Parker's Hydrodynamic Model

Parker (1958) theoretically demonstrated that the solar corona could not be in hydrostatic equilibrium at large distances, so it must be continually expanding. Parker developed a hydrodynamic model based on this demonstration, which he called the solar wind. This model is based on the assumptions:

- the solar wind behaves like an ideal gas
- electromagnetic forces are negligible ($\mathbf{E} \to 0, \mathbf{J} \times \mathbf{B} \to 0$)
- the plasma is isothermal
- the system is spherically symmetric

- the solar wind flows radially away from the Sun
- Solar wind mass flux across a spherical surface constant
- changes in the solar wind are slower than the rate of solar wind generation

Parker (1958) derived the following equation of motion, using the equations for the conservation or mass and momentum, which describes how the speed of the outflowing coronal plasma varies with radial distance:

$$\frac{1}{\mathbf{v}}\frac{d\mathbf{v}}{dr}\left(\mathbf{v}^2 - \frac{2k_BT}{m_p}\right) = \frac{4k_BT}{m_pr} - \frac{GM_S}{r^2}, \tag{1.20}$$

where $\mathbf{v}$ is the velocity, r is the radial distance, k_B is the Boltzmann constant, T is temperature, m_p is the proton mass, G is the gravitational constant, and M_S is the mass of the Sun. At the critical radius (r_c) the outward pressure gradient becomes dominance over the gravitational forces.

$$r_c = \frac{GM_Sm_p}{4k_BT} \tag{1.21}$$

At distances smaller than the critical distance the solar wind flow remains subsonic, while at large distances it becomes supersonic.

There are five classes of solutions to Parker's equation of motion, shown in Figure 1.8. Solution *AC* is not a viable solution as it indicates that the solar plasma does not extend into the heliosphere, due to its confinement to the lower radial distances. Similarly, solution *BD* is constrained to higher radial distances, indicating that the solar plasma does not connect to the corona. Solution *BC* is not viable as it suggests supersonic flows at the base of the corona, where observations show they are subsonic. Solutions *AD* and *AB* both predict the subsonic flows at the corona, but differ by how the solar wind behaves at higher radii. As $r \to \infty$ *AD* predicts a finite pressure that is unlikely to balance interstellar space. Therefore, Parker concluded that the solar wind must behave as *AB* describes, with the solar wind accelerating to supersonic speeds

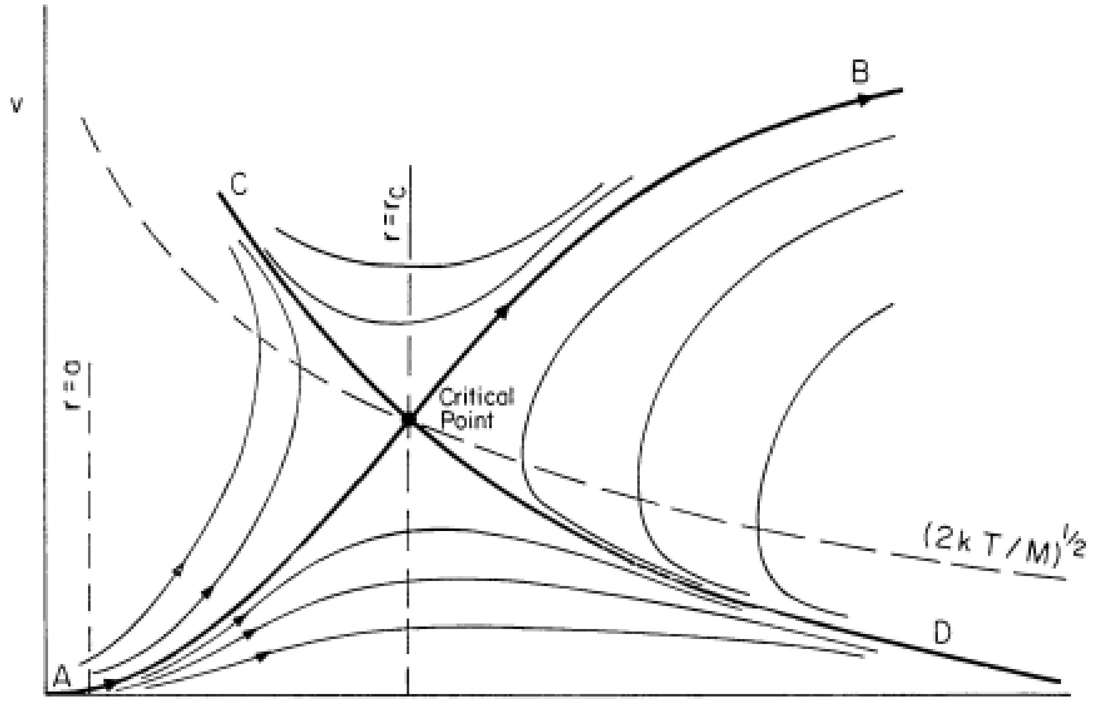

Figure 1.8: Figure from Parker (1965) showing the radial distance (x-axis) against the solar wind velocity (v). This shows the five solutions to the solar wind equation.

with increasing radial distance. Observations support this, as the solar wind at 1AU is supersonic with typical speeds of 450 km/s.

Exospheric Model

The exospheric model is a kinetic model of the solar wind plasma, which views the solar wind as the evaporation of the coronal plasma. This model was originally proposed by Chamberlain (1960) who reported that the solar corona becomes collisionless beyond 2.5 solar radii, where it expands out into space to form the exosphere, encompassing the entire solar system.

For an electron in the system (all particles are treated individually) to progress past the base of the exosphere it must have a sufficient velocity (v_{esc}) to escape the electrostatic and gravitational potentials of the Sun, which is given by:

$$v_{esc} = \sqrt{\frac{2GM_S}{r_0}}, \tag{1.22}$$

where G is the gravitational constant and M_S is the solar mass.

Chamberlain's model, known as the "solar breeze model", assumes that the protons move without collisions along radial magnetic field lines in the gravitational field of the Sun and a polarisation electric field. This assumption is needed to maintain quasi-neutrality in planetary and stellar ionospheres that are in hydrostatic equilibrium (Echim et al., 2011).

1.4.2 Heliospheric Magnetic Field

The heliospheric magnetic field (HMF) is rooted in the Sun's photosphere and extends out into the solar system, where it enables the Sun to magnetically interact with planetary magnetospheres. The HMF is the fraction of the magnetic flux that threads the solar photosphere and extends to a sufficient heliocentric distance that it is dragged out by the solar wind as a result of frozen-in flux (see Section 1.2.2) (e.g. Levine et al., 1977, Owens and Forsyth, 2013).

Parker's model has shown that the corona is continuously expanded, this the magnetic field lines are expected to be dragged out radially by the expanding plasma. Assuming the magnetic field lines have fixed footpoints in the photosphere, which rotate with the surface of the Sun, the large scale HMF twists to form an Archimedean spiral, thus known as the Parker spiral (Parker, 1958), as shown in Figure 1.9. This spiral obeys the expression:

$$\frac{B_\phi}{B_r} = \frac{-\Omega r \mathrm{sin}\theta}{v_r} \tag{1.23}$$

where v_r is the radial component of the solar wind bulk velocity, B_ϕ and B_r are the azimuthal and radial component of the magnetic field, Ω is the mean solar rotation speed, and θ is the heliospheric latitude of the observer. Therefore, the spiral is more/less tightly wound at: increasing/decreasing radial distance, decreasing/increasing v_r, and closer/further from the ecliptic plane. At 1AU, where solar wind speeds $\sim 450km/s$, $B_\phi/B_r \approx -1$, therefore the Parker angle between them is $\sim 45°$.

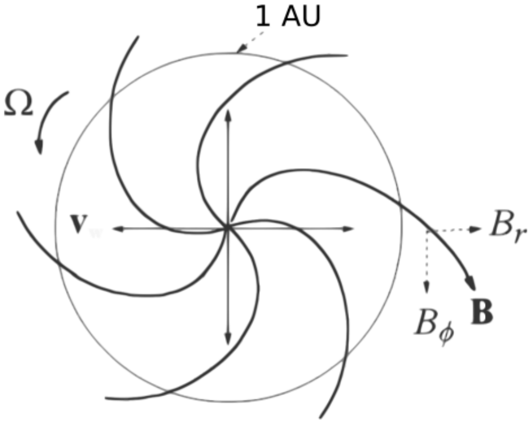

Figure 1.9: Figure from Macneil (2018) showing the Parker spiral HMF in the ecliptic plane, viewed from the north pole. The direction of rotation (Ω), solar wind bulk velocity (**v**), magnetic field vector (**B**) and components (B_ϕ and B_r) are all shown.

OSF and the Source Surface

The altitude at which coronal loops are carried out is set by the acceleration profile of the slow solar wind, which increases the solar wind speed from near zero at $0.5R_\odot$ and reaches full velocity at about $15R_\odot$ (Srivastava et al., 1999). Since the majority of the photospheric magnetic flux results in closed loops relatively near to the Sun - which do not contribute to the HMF - it is useful to define a "source surface" where the HMF begins. Magnetic loops that return to the Sun without extending beyond the source surface are called "closed" and more distended loops that enter the heliosphere are called "open": the distinction between the two is that open field lines thread the coronal source surface (Wang and Sheeley, 1995). Thus the total unsigned magnetic flux threading the source surface is referred to as the open solar flux (OSF). However, there are no abrupt changes in the plasma or field parameters that mark the location of the source surface and a number of definitions have been used. The simplest is that the source surface is a heliocentric sphere of a fixed radius (Schatten, 1968a,b). The choice of that radius is arbitrary (typically placed between $2R_\odot$ to $3R_\odot$) and it is therefore important when we compare different OSF estimates they employ the same definition of the source surface.

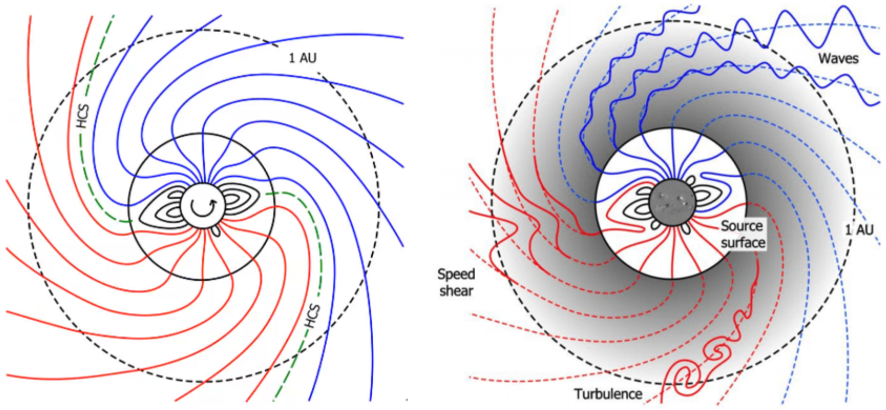

Figure 1.10: A schematic of the Sun's magnetic field. The red and blue lines are magnetic field lines of opposite polarity and the dashed green line is the heliospheric current sheet (HCS) separating the two polarities. The left panel shows a Parker spiral magnetic field (Owens and Forsyth, 2013) and the right panel shows the magnetic field with local inversions at 1 AU (credit: Prof. Mathew Owens).

As described by Maxwell's equation $\nabla \cdot \mathbf{B} = 0$, magnetic fields always form closed loops and there is no net source of magnetic flux. Thus positive (outward) and negative (inward) flux cancel over any closed surface. Therefore, for Parker spiral HMF (Parker, 1958), the unsigned magnetic flux threading the source surface (the OSF) equals that threading a sphere of heliocentric radius R, here referred to as the total heliospheric magnetic flux (total HMF) and denoted Φ_R.

Outer Boundary of the Heliosphere

When the solar magnetic field reaches the edge of the heliosphere, it interacts with the interstellar magnetic field. As shown in Figure 1.11, the heliosphere is a bubble created by the solar wind pushing against the interstellar medium. At the edge of this bubble, known as the heliopause, the pressure from the solar wind balances with the pressure from the interstellar medium.

At this boundary, the magnetic field lines become distorted and stretched as they interact with the magnetic fields from outside the heliosphere. This interaction can lead to the formation of a complex magnetic structure known as the heliosheath. In the heliosheath, the solar magnetic field lines are no longer organised in a simple, radial

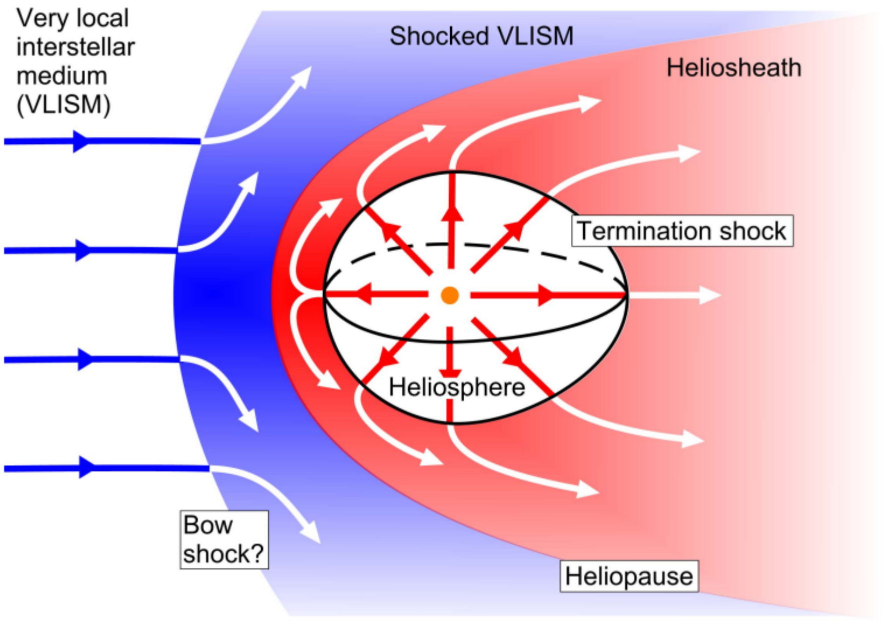

Figure 1.11: A cartoon of the global structure of the heliosphere from Owens and Forsyth (2013). Within the heliopause, where the solar wind flow is supersonic, a termination shock forms to slow and deflect the solar wind within the heliosheath. Beyond the heliopause, the nearby interstellar medium (known as the very local interstellar medium or VLISM) is diverted around the heliosphere. Whether this interaction includes a stationary bow shock depends on the magnetic field's intensity and alignment within the VLISM.

pattern but become more turbulent and tangled. While the magnetic field lines from the Sun may not extend far into the heliosheath, their influence and interaction with the interstellar magnetic field are still significant at the boundary (Owens and Forsyth, 2013).

1.5 Summary and Context

This chapter introduced some of the background physics for the research presented in the remaining chapters. Chapter 2 will provide an overview of the methods of measuring the OSF and the discrepancy between them. In Chapter 3 the instruments and datasets used throughout the analysis are introduced, as well as some pre-processing of the data. Chapters 4 - 6 present the scientific analysis carried out for this thesis. In Chapter 7 the work will be summarised and the future directions the work could take are discussed.

Chapter 2

Background Material

In the previous chapter key concepts in the study of the Sun's magnetic field were introduced. In this chapter, the Open Solar Flux (OSF) problem is introduced, which describes the discrepancy between *in-situ* and source surface OSF estimates. The methods of determining the OSF from *in-situ* and magnetogram observations are described as well as some limitations.

2.1 Magnetograms

Magnetograms are measurements of the field strength, polarity (+ or -), and location of the photospheric magnetic field, derived from magnetograph observations. The solar magnetic field is measured by exploiting the Zeeman effect, where the presence of a magnetic field changes the polarity of the measured light (Beckers, 1968). In the presence of a magnetic field, a spectral line at a single wavelength splits into a group of 3 lines of different wavelengths as shown in the right panel of Figure 2.1. The splitting of these spectral lines can be measured to determine the field strength and polarity along the line-of-sight (Lang, 1995). In a magnetogram image of the Sun, see Figure 2.2, the grey areas show weak magnetic field, the dark areas show "south" magnetic polarity (directed towards the center of the Sun), and the white areas show "north" magnetic polarity (directed towards Earth).

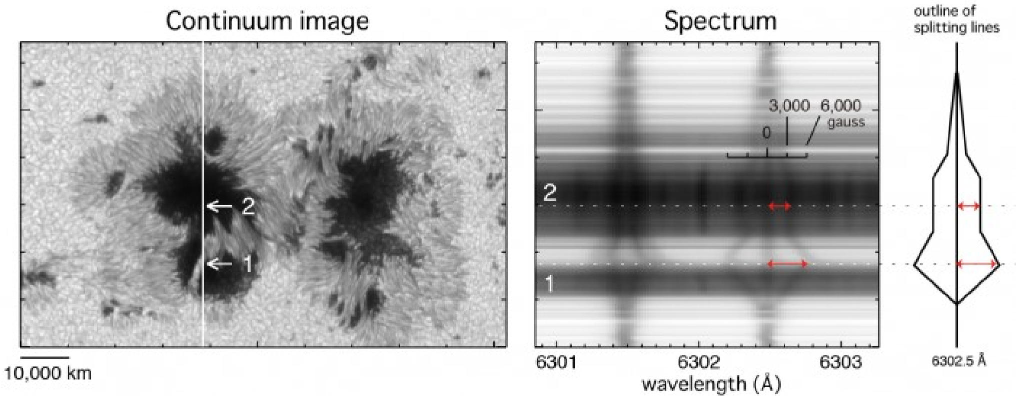

Figure 2.1: Figure from Okamoto and Sakurai (2018) showing a sunspot and its spectra observed with the Hinode SOT/SP (Solar Optical Telescope Spectropolarimeter). The panel on the left shows a continuum map of a sunspot scanned around 19 UT on 4/2/2014. The panel in the middle shows the splitting spectrum taken along the white line in the left panel. A large distance in the splitting indicates a strong magnetic field. On the right is a simplified diagram of the splitting of the iron absorption line. The magnetic field strength at location 1 exceeded 6 kG, while the magnetic field strength at location 2 was 3.5-4.5 kG.

Until the very recent *Solar Orbiter* mission (Mueller et al., 2013), these observations were limited entirely to the Earth-facing side of the Sun and captured from the ecliptic plane, resulting in poor viewing geometry for the polar field. Figure 2.3A shows the lack of visibility of the poles from the ecliptic plane. Figure 2.3B shows the small increase in visibility of one pole when Earth is positioned at 7.25° above the solar equator (caused by the Sun's rotation axis being tilted by about 7.25 degrees from the axis of the Earth's orbit). With Solar Orbiter, the poles will be much more visible, see Figure 2.3C, as it will have a view from 30 degrees above the solar equator (Riley et al., 2019). Current observations available from magnetograms would be missing the flux from these polar regions, resulting in an underestimation of the OSF from magnetograms.

2.1.1 OSF from Magnetograms

To obtain an estimate of OSF, photospheric magnetic field observations are collected over a complete solar rotation (approximately 27 days from Earth's point of view) to give full longitudinal coverage. Previous assumptions about the poles affect how

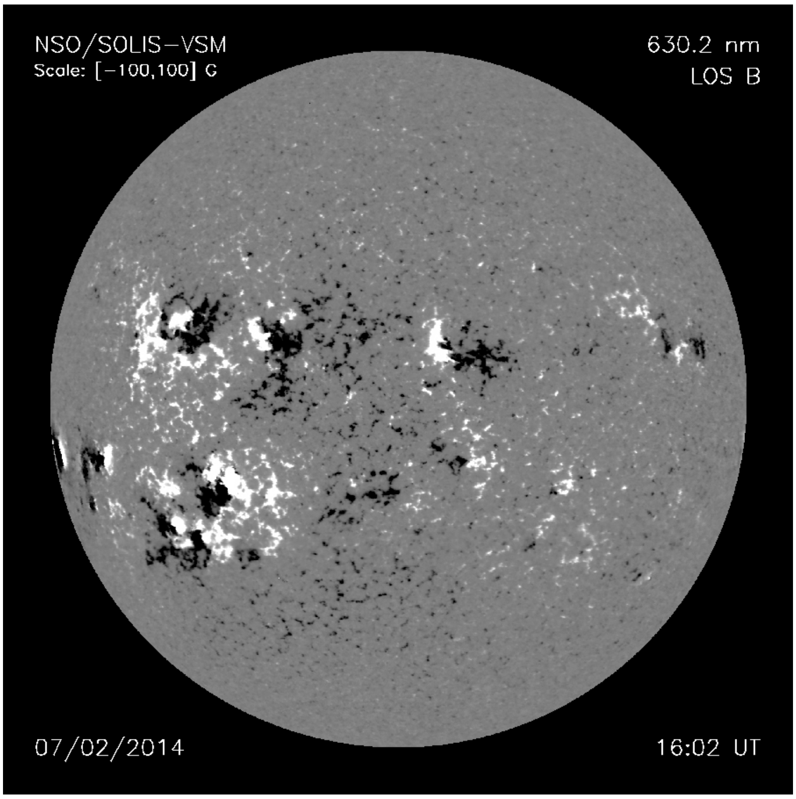

Figure 2.2: Full disk magnetogram from the National Solar Observatory. NISP/SOLIS magnetogram from 18 June 2014 during solar maximum. The grey areas show weak magnetic field, the dark areas show “south” magnetic polarity, and the white areas show “north” magnetic polarity.

they are accounted for in magnetic field synoptic maps as the polar fields need to be reconstructed. Magnetic field synoptic maps attempt to represent the magnetic field over the full surface of the Sun using observations from Earth’s viewing direction only. These reconstructions include extrapolating mid-latitude fields poleward (Riley et al., 2001), diffusing available noisy data to improve the signal-to-noise ratio (Riley et al., 2012), and allowing flux to migrate self-consistently poleward (Linker et al., 2017).

From the resulting photospheric magnetic field synoptic map (see Figure 2.5d for an example of a synoptic map), the magnetic field is extrapolated to the top of the corona to estimate the OSF. This extrapolation is achieved using a coronal magnetic field model, such as a potential field source surface (PFSS: Schatten et al., 1969) model (discussed further in Section 2.1.2). These methods necessarily contain arbitrary choices that affect the OSF, most notably, the assumed radius of the source surface, at which

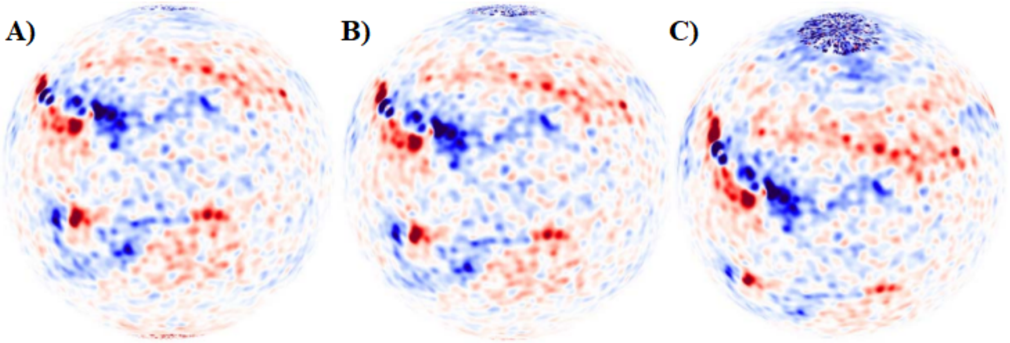

Figure 2.3: Figure adapted from Riley et al. (2019) showing the line-of-sight component of the photospheric magnetic field with small spots added to the polar regions (the added spots are synthetic data). Panel A) shows the view from Earth when Earth is in the solar equatorial plane. Panel B) shows the view from Earth when Earth's position is at 7.25° above the solar equatorial plane. Panel C) shows the view from 30° above the solar equatorial plane.

magnetic flux is assumed to be open to the heliosphere. For coronal MHD, there is no source surface per se, but how the solar wind flow is imposed affects the OSF.

Model-free estimates of OSF have also been derived from magnetograms by assuming all the OSF resides within visually identified coronal holes (e.g. Linker et al., 2017, Wallace et al., 2019), dark regions in extreme ultraviolet (EUV) and X-ray images (Cranmer, 2009). The OSF estimate is then just the signed flux integrated over those dark regions.

Using this assumption of all OSF residing in these observable coronal holes, the radius of the source surface can be calibrated by matching OSF foot points with the observed coronal hole area, with the assumption that the source surface is a heliocentric sphere. However, the assumption that all OSF foot points appear as dark regions may not allow for some areas appearing bright at the edge of coronal holes, specifically when viewing away from the disc center. It also fails to include observed outflows from active regions bordering coronal holes which can also contribute to the slow solar wind (van Driel-Gesztelyi et al., 2012).

2.1.2 PFSS model

The potential field source surface (PFSS) model is a coronal magnetic field model developed by Schatten et al. (1969). Figure 2.4 shows a representation of the PFSS model. Region 1 represents the magnetic field at the photosphere which can be derived from magnetogram data. In Region 2 the magnetic field is dominant over the plasma, so the magnetic field can be derived from the Laplace equation $\nabla^2\phi = 0$, which assumes that Region 2 is current-free. Between Region 2 and Region 3 is the "source surface" at which all magnetic fields are constrained to be radial to model the effect of the outflowing solar wind. Beyond the source surface the magnetic field lines that are open follow a Parker spiral configuration, i.e. the flow pressure dominates over the magnetic pressure.

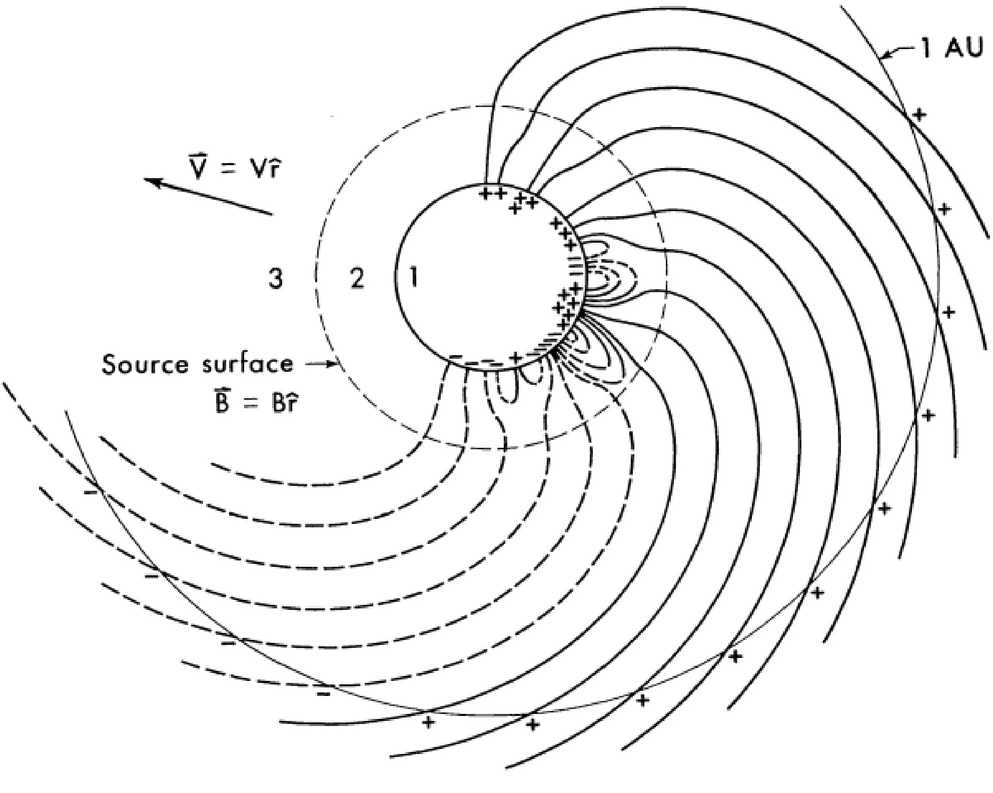

Figure 2.4: Schematic from Schatten et al. (1969) showing the PFSS model magnetic field lines.

While the convention at the inner boundary was originally to match the potential field expansion to the line-of-sight component of the photospheric field (Altschuler and

Newkirk, 1969), this assumes that the current-free approximation is valid at the depth the photospheric field is measured. Wang and Sheeley (1992) criticised this assumption and instead advocated for the photospheric field to be corrected for the line-of-sight projection before being matched to only the radial component of the potential field. This is because magnetogram measurements can detect deeper atmospheric layers where the field is non-potential.

In the PFSS model, the radius of the "source surface", R_{SS}, is a free parameter. Since R_{SS} determines the amount of open flux, the choice of radius can have a significant effect on the modelled field. Schatten et al. (1969) employed a R_{SS} of $1.6R_S$ ($0.6R_S$ above the photosphere) with the justification of observations of the highest closed loops in eclipse data having mean heights of $1.6R_S$ above the limb of the Sun. However, recent studies typically use a radius of around $2.5R_S$ (e.g. Riley et al., 2006, Linker et al., 2017) through optimising the computed OSF with *in-situ* measurements (Hoeksema et al., 1983).

Figure 2.5 is a figure from Nikolic (2019) showing the derived coronal holes for the CR 2060 GONG synoptic map (14th August to 10th September 2007) for $R_{SS} = 1.3, 1.5$ and $2.5R_\odot$ and the synoptic map of the corona (d) from the SOHO EIT 195 Å observations. In Figure 2.5d the red rectangles mark the location of some coronal holes that are no longer captured by the PFSS model when $R_{SS} = 2.5R_\odot$, which is a typical radius used in recent studies as stated previously. Figure 2.6 is a figure from Lee et al. (2011) showing the PFSS solutions for the same CR 2060, but using the MDI synoptic map instead. The results from Figures 2.5 and 2.6 both support the conclusion that the customary $R_{SS} = 2.5R_\odot$ is too high for this period of study, based on the derived and observed CHs and open magnetic flux. This highlights one of the difficulties in achieving a completely accurate PFSS solution from full disk synoptic maps.

One modification of the PFSS model is a current sheet model presented by Schatten (1972). This model extends the potential field beyond a given radius that requires the presence of current sheets. The magnetic field is first calculated up to the source surface, $1.6R_\odot$ for this study. At the source surface, the sign of all negative magnetic field lines is switched to make all magnetic field lines positive (pointing outward). A new set of harmonic coefficients is calculated for the unipolar outward-directed field before the orientation of the reversed field lines is restored. The introduction of these current sheets prevents the formation of closed loops beyond the source surface.

In the standard PFSS, the quasi-dipole distribution of $|B_r|$ is present, with the highest values at the poles and the lowest at the equator. With the implementation of the current sheet model, $|B_r|$ is able to equilibrate over the sphere.

2.2 In-situ Observations

In-situ solar wind observations are carried out by taking direct measurements at point locations using spacecraft. However, these single-point measurements are unable to directly distinguish between spatial and temporal variations in a plasma.

The solar wind is highly structured due to the different solar wind types and sources. Without solar rotation, the HMF would have a radial orientation with the two hemispheres having inward and outward directions (assuming the solar magnetic field is a rotation-aligned dipole). The current sheet separating the polarities has a large-scale warp, often referred to as a "ballerina skirt" (Wilcox et al., 1980), which creates intermittent sectors with opposite polarities or sector structure (Vokhmyanin and Ponyavin, 2013, Hudson et al., 2014), for example in Figure 2.7.

Different sectors can be identified from *in-situ* measurements by a change in magnetic field polarity. Using single-point measurements, a change in magnetic field polarity and a locally inverted magnetic field line would both give an indication of a sector boundary. Distinguishing between a sector boundary and locally inverted magnetic fields can avoid the false detection of sector boundaries.

2.2.1 Early In-Situ Results

Kahler et al. (1996) investigated the magnetic field polarities surrounding intrasector field reversals (IFRs). IFRs are defined as a period inside a sector where the magnetic field direction is consistent with the polarity opposite that of the sector itself. Sector boundaries were identified based on a comparison between the source surface model with plots of hourly magnetic field data at 1 AU. The IFRs used for this study were selected to be sufficiently distant from sector crossings (e.g. at least 1 day after the crossing for an IFR of 2-3 days). Around half of the IFRs were cases where the polarities matched those of the surrounding sectors, indicating locally inverted fields (a.k.a. "switchbacks" or "folded flux"), see Figure 2.8A. IFRs with polarity reversals, Figure 2.8B, were found to be strongly associated with periods of bidirectional electron flows, meaning these fields occur with closed fields.

Kahler et al. (1998) studied the distributions of sector durations with solar activity, using the solar wind electron heat flux (usually carried away from the sun by electrons) directions to determine the field polarities. In addition to the expected large-scale sectors they also detected a number of small-scale sectors. They examined cases of false polarities, where the directions of the field imply polarities opposite to those determined from the heat-flux directions, i.e. folded/inverted fields. These inverted fields were found to have no associated bidirectional electrons.

Crooker et al. (2004) examined intervals of mismatch between sector boundaries identified by suprathermal electron ($\gtrsim$ 80 eV) pitch angle spectrograms and in magnetic field data alone. They analysed 8 cases of inverted flux between December 1994 and August 1995, each lasting between 15-53 hours (7 of the cases were between 15-24 hours). In most cases, the inversions do not point along the Parker spiral opposite to its true polarity, instead the field hovers nearly orthogonal to it. These mismatches support the presence of locally inverted magnetic fields.

2.2.2 OSF from In-situ Measurements

Total HMF estimates are derived from *in-situ* solar wind spacecraft measurements by integrating the observed radial magnetic field (B_r) over a heliocentric sphere of radius equal to the observation distance. Smith and Balogh (1995) outlined a key finding enabling the estimation of total HMF from single-point *in-situ* measurements: using the *Ulysses* spacecraft they found that the magnitude of the B_r, corrected for heliocentric distance, was independent of latitude. From the Ulysses data, they identified sectors with only negative polarities and averaged $B_r R^2$ over 3 solar rotations. They compared this with magnetic field measurements from IMP8 (measurements taken of the equatorial field), from which they also isolated only the negative polarities and averaged $B_r R^2$ over 3 solar rotations. Smith and Balogh (1995) found good agreement between the two data sets, concluding there was no significant latitude dependence.

This result was explained by Suess and Smith (1996) and Suess et al. (1996) who noted that close to the Sun the plasma beta is low, so magnetic pressure dominates. Thus the solar wind flows will be slightly non-radial in this region until tangential (and hence latitudinal) magnetic pressure is equalised, resulting in the constancy of radial magnetic field magnitude over a heliocentric sphere. Thereafter, radial flow means that the latitudinal invariance of $|B_r|$ is preserved out into the heliosphere.

Longitudinal coverage is then obtained by integrating over a solar rotation (approximately 27 days for L1 spacecraft), expressed as $\langle |B_r| \rangle_{27\mathrm{day}}$. The total heliospheric flux threading the heliocentric sphere at the radius of observation, R, can then be calculated as $\Phi_R = 4\pi R^2 \langle |B_r| \rangle_{27\mathrm{day}}$. Note that while we here use $4\pi R^2 |B_r|$, the total unsigned HMF, sometimes the total signed HMF ($2\pi R^2 B_r$) is used instead, such as in Lockwood et al. (1999).

A subtle, but critical, point is that the time resolution at which one performs the modulus of B_r as it makes a significant difference to the total HMF estimate, and this is something of a free parameter (Lockwood et al., 2009*b*). Note that Smith and Balogh (1995) avoided this by not actually using the modulus but, rather, averaging (signed)

B_r over what they defined by eye to be toward and away sectors of the HMF. This was also less pressing for Smith and Balogh (1995) as they were using Ulysses data, which is primarily out of the ecliptic. In ecliptic data, this is a bigger deal as these false sectors are more abundant. But, as pointed out by Lockwood and Owens (2013), using B_r averaged over sectors raises a problem of objectively distinguishing what is a genuine sector boundary (a change in B_r polarity that maps all the way back to the coronal source surface) from inverted HMF flux in the heliosphere (which do not map back to the source surface). Making that distinction is a key issue addressed in the present thesis.

The existence of this inverted HMF flux also adds complexity to OSF estimates. Figure 2.9 shows a sketch of the topology of the HMF from the heliographic equatorial plane. 2.9a shows an area of open magnetic flux with a locally inverted field. A spacecraft taking point measurements at 1AU, following the grey dashed line, would cross the same magnetic field line 3 times. This would result in the open magnetic flux being perceived as shown in 2.9b, which would result in an increased value for the OSF.

In order to estimate OSF from *in-situ* observations, it is necessary to relate the total HMF to the OSF. It is often implicitly assumed that the two properties are identical, i.e. $\mathrm{OSF} = \Phi_R$. As previously mentioned, this is true for an ideal Parker spiral, but not for the "real" solar wind. Using observations from a wide range of heliospheric spacecraft, Owens et al. (2008) reported that Φ_R estimates increased with R, see Figure 2.10. This indicates that the assumption $\mathrm{OSF} = \Phi_R$ cannot be valid. The "flux excess" with heliospheric distance was also addressed by Lockwood et al. (2009*b*,*c*) using a "kinematic correction" to account for the effect of large-scale longitudinal structure of the solar wind flow which could generate inverted HMF via stream sheer. Applying this correction gives a result in reasonable agreement with Owens et al. (2017), described below.

Erdos and Balogh (2014) described an alternate method aimed at correcting for R-dependence of total HMF estimates. Their approach was to consider only the HMF component along the ideal Parker spiral direction. This method showed very good agreement between total HMF estimated from spacecraft at different latitudes and distances. However, this does not necessarily mean that the total HMF values provide accurate OSF estimates. HMF inversions are not explicitly removed by this procedure, as they are often aligned with the Parker spiral orientation. More importantly, an arbitrary time averaging for B_r of 6 hours was used without justification. Using different time averaging reveals the same free-parameter issue which plagues the standard $\Phi_R = 4\pi R^2 \langle |B_r| \rangle_{27\mathrm{day}}$ method (Owens et al., 2017).

2.3 OSF Problem

The Sun's open solar flux (OSF) is the component of the Sun's magnetic field that reaches a sufficient height to be dragged into the heliosphere by the solar wind. Photospheric estimates currently disagree with the OSF estimates by *in-situ* spacecraft. As source surface observations are the basis for all long lead time space weather forecasts, the ability to reconstruct the OSF acts as a basic test of coronal models (Linker et al., 2017).

As described by Section 1.4.2, it is expected that the unsigned magnetic flux threading the source surface should be equal to the unsigned magnetic flux threading a sphere of heliocentric radius R. What is observed, however, is that OSF estimates derived from remote sensing observations (magnetograms) are around a factor of two lower than Φ_R. This discrepancy is partially due to local HMF inversions (or 'switchbacks') (Kahler and Lin, 1994, Crooker et al., 1996, Kahler et al., 1996, Balogh et al., 1999, Crooker et al., 2004, Owens et al., 2013, Bale et al., 2019, Horbury et al., 2020), which result in the magnetic flux threading a 1-AU sphere (and contributing to $\Phi_{R=1\mathrm{AU}}$) but not the source surface (and thus not contributing to the OSF), see Figure 2.9. However, even using methods to correct for inverted HMF (Owens et al., 2017, Frost et al., 2022) in Φ_R, *in-situ* based estimates of OSF are still systematically larger than those obtained from photospheric observations (Linker et al., 2017, Wallace et al., 2019).

2.4 Summary

This chapter has introduced the various methods of measuring the Sun's magnetic field. Magnetograms take full-disk measurements of the Sun's magnetic field, but these are limited to the Earth-facing side of the Sun with limited visibility of the poles. To obtain an OSF estimation from magnetograms, a coronal model is needed to extrapolate the magnetic field to the top of the corona. *In-situ* solar wind observations are direct measurements of the magnetic field, however, these are limited to single-point measurements that are unable to distinguish between spatial and temporal variations in a plasma. The limitations of these measurements of the Sun's magnetic field contribute to the OSF problem, where magnetogram observations are unable to accurately reconstruct the OSF observed by *in-situ* spacecraft. The remainder of this thesis solely focuses on the *in-situ* magnetic field measurements.

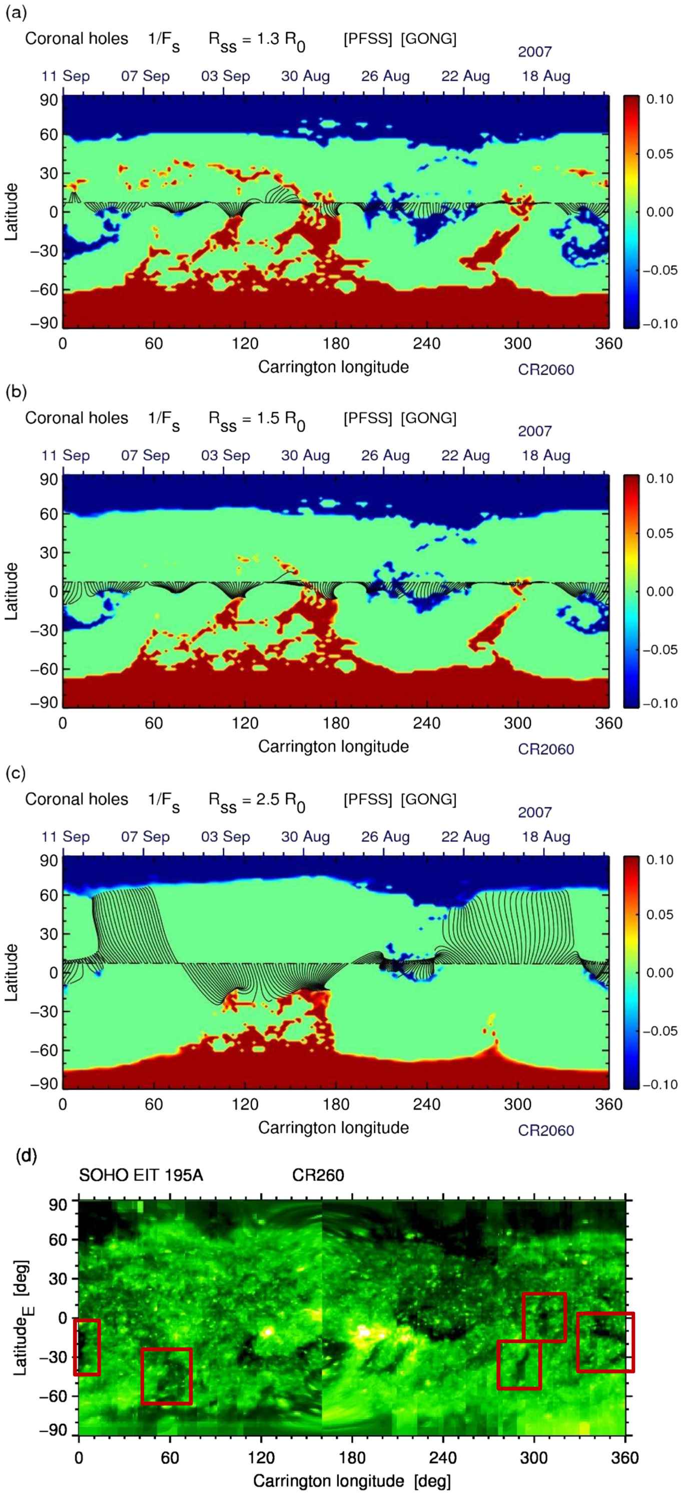
(a)
Coronal holes 1/F_s R_ss = 1.3 R_0 [PFSS] [GONG]
2007
11 Sep 07 Sep 03 Sep 30 Aug 26 Aug 22 Aug 18 Aug
90 60 30 0 −30 −60 −90
Latitude
0 60 120 180 240 300 360
Carrington longitude
CR2060
0.10 0.05 0.00 −0.05 −0.10
(b)
Coronal holes 1/F_s R_ss = 1.5 R_0 [PFSS] [GONG]
2007
11 Sep 07 Sep 03 Sep 30 Aug 26 Aug 22 Aug 18 Aug
Latitude
Carrington longitude
CR2060
(c)
Coronal holes 1/F_s R_ss = 2.5 R_0 [PFSS] [GONG]
2007
11 Sep 07 Sep 03 Sep 30 Aug 26 Aug 22 Aug 18 Aug
Latitude
Carrington longitude
CR2060
(d)
SOHO EIT 195A CR260
Latitude_E [deg]
Carrington longitude [deg]

Figure 2.5: Schematic from Nikolic (2019) showing PFSS modeled coronal holes, in red and blue, using the CR 2060 GONG synoptic map and the source surface placed at (a) $R_{SS} = 1.3R_\odot$, (b) $R_{SS} = 1.5R_\odot$, and (c) $R_{SS} = 2.5R_\odot$. (d) SOHO EIT 195 Å CR 2060 synoptic map of the solar corona. The red rectangles in (d) mark some coronal holes that are not fully captured by the PFSS model with $R_{SS} = 2.5R_\odot$.

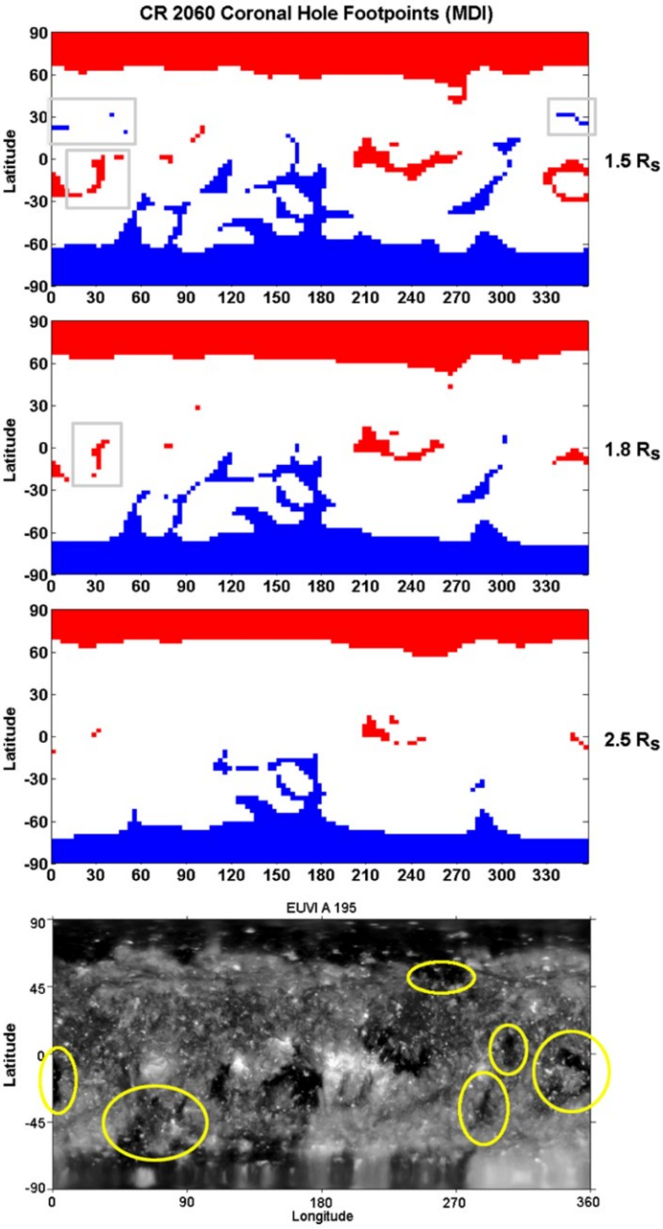
CR 2060 Coronal Hole Footpoints (MDI)
Latitude
90
60
30
0
-30
-60
-90
0
30
60
90
120
150
180
210
240
270
300
330
1.5 R_S
1.8 R_S
2.5 R_S
EUVI A 195
45
-45
90
180
270
360
Longitude

Figure 2.6: Schematic from Lee et al. (2011) showing PFSS modeled coronal holes, in red and blue, using the CR 2060 MDI synoptic map and the source surface placed at $R_{SS} = 1.3R_\odot$, $R_{SS} = 1.5R_\odot$, and $R_{SS} = 2.5R_\odot$. The bottom panel shows the STEREO/EUVI image of CR 2060 synoptic map of the solar corona. The yellow circles mark the coronal hole features missing from the $R_{SS} = 2.5R_\odot$ results and the grey rectangles mark the features that appear in the mapping results but not in the EUV image.

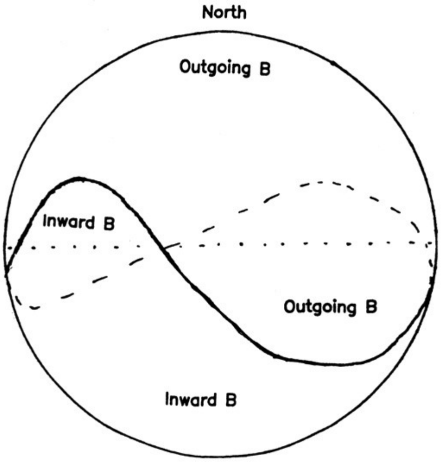

Figure 2.7: Sketch of the polarity of the heliospheric magnetic field from Vallee (1998). The location of the heliospheric current sheet is shown by the black line (and the dashed line showing the back side of the Sun). Moving around the equatorial plane (shown by the dots) one rotation passes through 4 different polarities, hence 4 magnetic sectors.

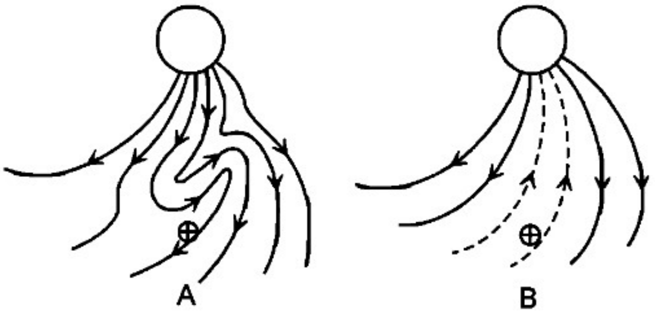

Figure 2.8: Schematic from Kahler et al. (1996) showing (**A**) a field resulting from an inverted unipolar field, and (**B**) a field with a polarity reversal embedded in a sector.

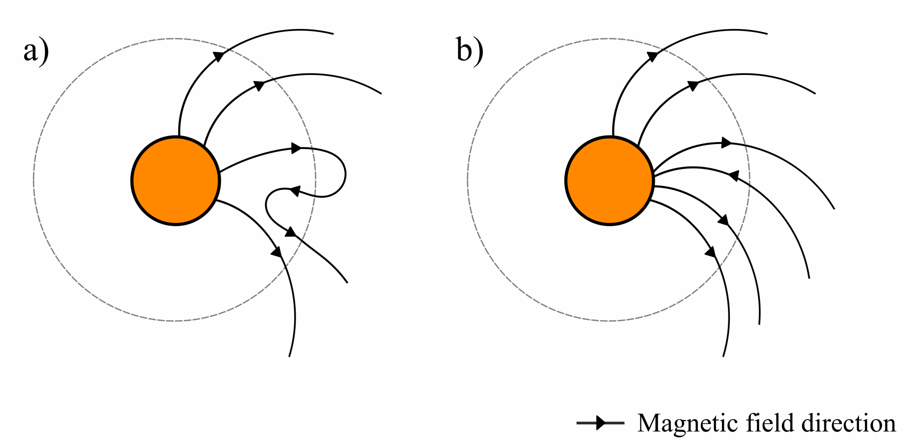

Figure 2.9: Schematic of the topology of the HMF viewed from the heliographic equatorial plane. The *solid black lines* are the magnetic field lines with *black arrows* indicating the direction. The *grey dashed line* is 1 AU. (**a**) shows an area of open magnetic flux with a locally inverted field. (**b**) shows an area of open magnetic flux as detected from point measurements.

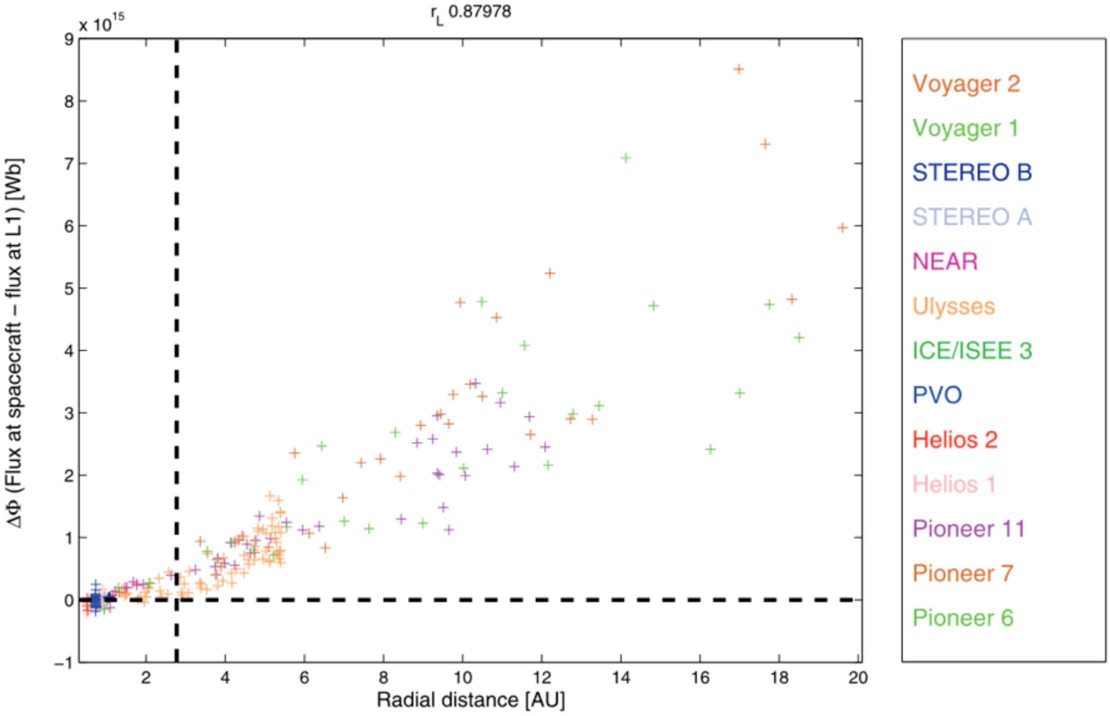

Figure 2.10: Figure from Owens et al. (2008) showing the increasing Φ_R estimates with increasing radial distance for various spacecraft (colour-coded as shown on the right of the plot). Beyond $R = 2.5AU$, marked by the *vertical dashed line*, there is a clear positive increase in Φ_R with radius.

Chapter 3

Instrumentation and Data

In this chapter, the space missions, instruments, and datasets used in this thesis are described. First, a description of some key instruments on board the spacecraft will be given. Next, each spacecraft's mission will be introduced, before the specific instruments are given and the data used within this thesis described. While the ACE spacecraft was always operating around L1, the *Wind* spacecraft carried out various maneuvers that carried it into the magnetosheath and/or magnetosphere so it was not always in the undisturbed solar wind. The removal of this data is detailed and a brief overview is given of the data obtained from ACE and/or *Wind* where they were taking measurements in the undisturbed solar wind.

3.1 Detectors

Measurements of the solar wind are made using various instruments onboard ACE and *Wind*. Below are general descriptions of these instruments and how they work.

3.1.1 Fluxgate Magnetometer

Fluxgate magnetometers are widely used for measuring magnetic fields due to their simplicity and low power consumption. They are made up of a highly magnetically permeable ring core wrapped with two orthogonal coil windings (drive and sense) (Acuna, 1974), shown in Figure 3.1.

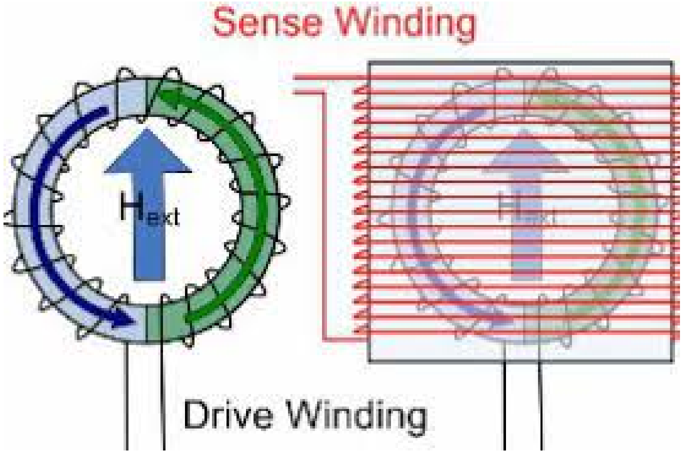

Figure 3.1: Schematic showing a single-axis fluxgate magnetometer sensor, see text for description. Image taken from Senthilmurugan et al. (2020).

An alternating current is applied to the drive winding, which induces oppositely directed magnetic fields in each half of the core. The alternating current drives the core through a magnetic saturation cycle which repeatedly flips the polarity. The resulting flipping magnetic field in the core induces an alternating current in the sense winding. In the absence of an external magnetic field, the current in the coils is identical. In the presence of an external magnetic field, the half-core containing a magnetic field opposite to the external field will come out of saturation sooner than the other half-core (containing a field in the same direction as the external field). This creates a variable current in the sense winding which is dependent on the external magnetic field's strength and polarity. A single coil is only able to detect the magnetic field in one plane. By combining three orthogonal fluxgate magnetometers, the three-dimensional magnetic field vector can be obtained.

3.1.2 Top-Hat Electrostatic Analysers

Top-hat analysers selectively measure charged particles that meet specific energy and angular criteria. Figure 3.2 shows the geometry of the top hat analyser. The analyser consists of two nested curved plates, often referred to as "hemispheres", with a parallel plate collimator mounted at the entrance, allowing electrons of approximately tangential velocity to enter the instrument (Paschmann and Daly, 1998).

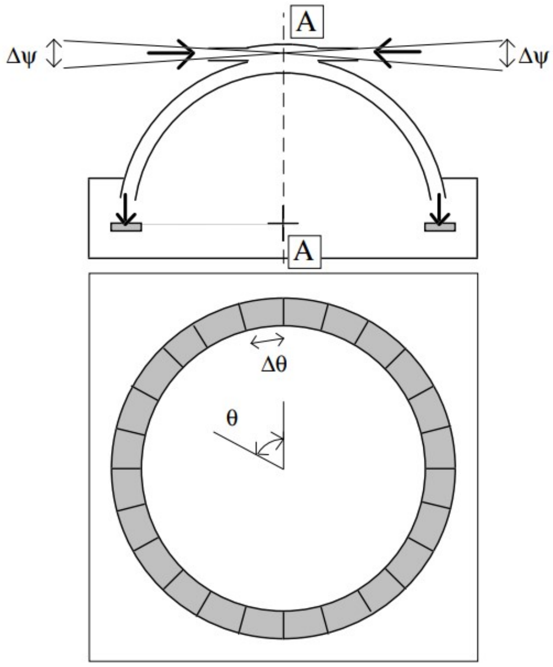

Figure 3.2: Schematic showing a Top Hat electrostatic analyser. The top illustration shows a cross-section of the analyser and the bottom illustration shows the detector. Image taken from Paschmann and Daly (1998).

Electrons that enter the analyser are deflected by an applied electric field between the plates. This electric field only allows electrons within the selected range of energies and azimuthal angles to pass through the analyser to be detected, see Figure 3.3. Electrons outside the desired range of energies collide with the walls of the instrument. By varying the applied voltage, electrons of different energies can be observed. The detector counts the number of particles in the selected energy and angle range by the part of the detector that the particles hit. Since this only detects particles in one plane, a 3-D distribution is built by the detector scanning the sky, usually, by the spacecraft spinning.

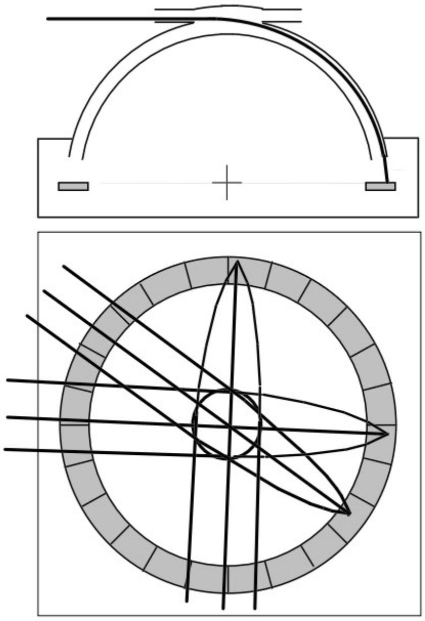

Figure 3.3: Schematic showing the same top hat analyser from Figure 3.2 with particle trajectories shown by thick black lines. Image taken from Paschmann and Daly (1998).

3.2 ACE Mission

The Advanced Composition Explorer (ACE) was launched on August 25th, 1997 with the primary objective being to examine the composition of the corona, interstellar medium, and galactic matter. ACE was placed in an L1 orbit, allowing it to provide continuous measurements of the solar wind, low-energy solar and interplanetary particles, and cosmic rays (Stone et al., 1998). ACE's instrument and spacecraft design requirements were originally for a 2-year mission, however, the mission is still ongoing at the time of writing, over 25 years after launch. It has been predicted that ACE has enough propellent on board to maintain an orbit at L1 until ~2024 (Christian and Davis, 2019).

On board ACE there are 9 instruments, see Figure 3.4: CRIS (cosmic-ray isotope spectrometer), SIS (solar isotope spectrometer), ULEIS (ultra-low energy isotope spectrometer), SEPICA (solar energetic particle ionic charge analyser), EPAM (electron, proton, and alpha monitor), SWIMS (solar wind ion mass spectometer), SWICS (solar wind ion composition spectrometer), SWEPAM (solar wind electron, proton, and alpha monitor), and MAG (magnetometer) (Stone et al., 1998). In this thesis, we only use data from SWEPAM and MAG, both of which are described below.

3.2.1 SWEPAM

The Solar Wind Electron, Proton, and Alpha Monitor (SWEPAM) was designed to measure the three-dimensional characteristics of the bulk solar wind (Stone et al., 1998). The SWEPAM instruments on board ACE are recycled and modified spares from the Ulysses mission, specifically the electron and ion sensors.

Electrons and ions are measured separately by spherical section electrostatic analysers, SWEPAM-E and SWEPAM-I, which produce full 3D observations due to the spacecraft spinning. The spacecraft spins at 5 rpm, with the spin axis generally pointed along the Earth-Sun line. This means the plane from which the particles enter the instrument is rotated every 12 seconds. SWEPAM observes suprathermal electrons 1.6-1350eV (12% energy resolution) and ions 260eV/q-36keV/q (2.5%) once every 128s/64s for electrons and ions respectively (McComas et al., 1998).

Publicly available data from SWEPAM include proton number density, solar wind bulk speed, the radial component of the proton temperature, alpha/proton ratio, solar wind velocity, and spacecraft position. Data is available at 64 s and 1-hour resolution.

3.2.2 MAG

The magnetic field experiment (MAG) on ACE provides continuous measurements of the local magnetic field in the interplanetary medium. MAG is made up of twin, boom-mounted, triaxial flux-gate magnetometers located on opposite solar panels (Stone et al., 1998). Like SWEPAM, MAG is a reconditioned flight spare this time from the WIND MFI instrument, with modifications to increase the sampling rate of the instrument.

Wide-range magnetic field measurements are taken between ± 0.001 and ± 65536 nT at a rate of 24 vector samples s^{-1} in snapshot memory, and 3-6 vector samples s^{-1} in a continuous data stream. In Range 0, with a dynamic range of ± 0.001nT, the sensitivity is quoted as $\sim 0.5 \times 10^{-3}$ nT Hz^{-1} (Smith et al., 1998).

3.2.3 ACE Data

ACE data used in this thesis are magnetic field data obtained from the MAG magnetometer (magnetic fields experiment, Smith et al., 1998) and electron data from SWEPAM (solar wind electron, proton, and alpha monitor, McComas et al., 1998). We obtain electron pitch angle distribution (PAD) functions (units s^3cm^-6) from the SWEPAM data set at an energy of 272 eV, well into the suprathermal energy range. Radial magnetic field data is obtained from the MAGSWE data set from the MAG instrument.

Figure 3.5 shows an example of 6 hours of data from 4th January 2007 from SWEPAM and MAG. The top panel shows the velocity distribution function (VDF) as a function of pitch angle (PA) and time at a fixed energy (272eV). The pitch angle of a charged particle is the angle between the particle's velocity vector and the local magnetic field. The middle panel of Figure 3.5 is the same as the top panel, but it has been normalised to the maximum and minimum flux at each time step. The SWEPAM data is divided into 20 PA bins, each 9 degrees wide. The bottom panel shows the radial magnetic field in GSE coordinates. GSE (Geocentric Solar Ecliptic) coordinates have the x-axis pointing from the Earth toward the Sun, the y-axis in the ecliptic plane pointed towards dusk, and the z-axis parallel to the ecliptic pole (Russell, 1971).

The first 20 months of the MAGSWE data set was discovered to have a resolution of 128 s, however, the remaining data has a 64 s (i.e., spin-averaged) resolution. In addition to this resolution difference, the SWEPAM data was offset from MAGSWE by 15 s. To correct this offset and to ensure a consistent resolution, while also allowing us to use the entire data set available, the SWEPAM and MAGSWE data were re-sampled to a resolution of 128 s at a consistent time step. This re-sampling was carried out by first up-sampling the data to 1 s resolution by forward-filling the values and then down-sampling the data to the 128 s resolution by averaging the groups of 1 s intervals.

By re-sampling the data in this way, the correct weighting of each data point was taken into consideration.

3.3 Wind Mission

The Interplanetary Physics Laboratory, known as the *Wind* spacecraft, was launched on November 1st, 1994 as part of the Global Geospace Science (GGS) program, with the primary objective to study the interplanetary medium and the effects of disturbances on the magnetosphere (Ogilvie and Desch, 1997). At the beginning of the mission, *Wind*'s trajectory carried it into various regions of space including into the Earth's magnetosheath and magnetosphere. From early 2004 *Wind* was placed in an orbit around L1. While the mission was originally planned for 3 years, it is currently still ongoing at the time of writing, 28 years after launch.

On board the *Wind* spacecraft there are 8 instruments, see Figure 3.6: Magnetic Field (MFI), Radio and Plasma Waves (WAVES), Solar Wind Plasma (SWE), 3D Plasma (3DP), Energetic Particles (EPACT), Solar Wind Composition (SMS), Gamma-Ray Spectrometers (TGRS and KONUS) (Ogilvie and Desch, 1997). In this work, we only use data from 3DP, SWE, and MFI.

3.3.1 3DP

The 3D Plasma (3DP) experiment was designed to make measurements of the 3D distribution of plasma and energetic electrons and ions from a few eV to several hundred keV (Lin et al., 1995). The instrument was made up of three detectors: semi-conductor detector telescopes (SST), electron electrostatic analysers (EESA), and ion electrostatic analyzers (PESA). Work in this thesis only required electron data from EESA, which is made up of two top-hat symmetrical spherical section electrostatic analysers.

The high energy detector (EESA-H) covers electrons from around 200eV-30keV and the low energy detector (EESA-L), which we used the data from in this thesis, covers electrons from 3eV-1keV. EESA-L has a 180° field of view, so sweeps the full sky every spacecraft spin. *Wind* has a spin rate of 20 rpm (spin period of 3s) around an axis that is normal to the ecliptic plane. EESA completes 32 or 64 energy sweeps per spacecraft spin, with each energy having a resolution $\Delta E/E \approx 0.3$ (Lin et al., 1995).

3.3.2 SWE

The Solar Wind Plasma (SWE) experiment was designed to measure solar wind electrons and ions (Ogilvie et al., 1995). SWE is made up of a pair of Faraday cup (FC) sensors, a vector electron ion spectrometer (VEIS), and a strahl detector. Only data from the FCs was used for this thesis.

The FC sensors make 3D measurements of the solar wind plasma, from which the velocity, density, and temperature of the solar wind can be determined. The two FCs are located on the top and bottom of the spacecraft and each observe in a cone of half-angle 60°. As it rotates, a full 3D scan is captured in 1s. Proton velocity measurements are made between 200-1250 km s^{-1} with a precision of $\pm 3\%$, proton number density measurements between 0.1-200/cc with a precision of $\pm 10\%$, and alpha/proton number density between 0-100% with a precision of $\pm 10\%$. Data from the SWE Faraday cups is publicly available at 98s resolution.

3.3.3 MFI

The Magnetic Field Investigation (MFI) was designed to measure the interplanetary magnetic field (Lepping et al., 1995). MFI is made up of twin, boom-mounted, triaxial flux-gate magnetometers.

As with ACE, wide-range magnetic field measurements are made between ± 0.001 and ± 65536 nT at a rate of 44 vector samples s^{-1} in snapshot memory and 10.87 vector samples s^{-1} standard. The sensitivity threshold is quoted as $\simeq 0.5 \times 10^{-3}$ nT/$\sqrt{\text{Hz}}$ in Range 0 (Lepping et al., 1995).

3.3.4 Wind Data

Wind data used in this thesis are magnetic field (from MFI) and electron data from the 3DP (three-dimensional plasma analyser, Lin et al., 1995) EESA-L (low energy electron electrostatic analyser), and solar wind data from the solar wind plasma experiment (SWE). We obtain the electron PAD data with an energy of 265 eV (the closest energy available to the 272 eV used from ACE). The electron data provided by 3DP is the electron number flux with units $\mathrm{cm}^{-2}\mathrm{ster}^{-1}\mathrm{eV}^{-1}\mathrm{s}^{-1}$. We also used magnetic field and velocity data from 3DP. From SWE we used the alpha and proton number densities.

Figure 3.7 shows an example of 6 hours of data from 4th January 2007 from EESA-L. The top panel shows the electron number flux (ENF) as a function of pitch angle (PA) and time at a fixed energy (265eV). The middle panel is the same as the top panel, but it has been normalised to the maximum and minimum flux at each time step. The PA data is divided into 8 PA bins, each 22.5 degrees wide. The bottom panel shows the radial magnetic field in GSE coordinates.

Figure 3.8 shows an example of the same 6 hours of data from 4th January 2007 from EESA-L. Each panel shows the electron number flux (ENF) as a function of pitch angle (PA) and time at a selected energy. Each time step had been normalised to the maximum and minimum flux. The top panel shows the ENF at energy 13eV, the middle panel is at energy 265eV, and the bottom panel is at energy 1113eV. The lowest energy (13eV) is too low for Strahl detection as it is dominated by the thermal plasma and, hence is not field-aligned. The highest energy (1113eV) also does not show the Strahl as it's far above the required energy range. The 265eV is an acceptable energy for detecting the Strahl, as it forms a clear field-aligned beam.

Wind Bow Shock Identification

During the first 10 years of the mission, *Wind*'s orbit routinely took it inside the bow shock of the Earth, as shown in the later dates from Figure 3.9. As the studies presented in this thesis are only interested in the undisturbed solar wind observations, we remove these periods, as summarised by Figure 3.10. In geocentric solar ecliptic (GSE) coordinates, any data Sunward of the $x = 0$ line (positive x) with a radial distance from Earth of less than $30R_{\mathrm{E}}$ is flagged for removal, and any data to anti-Sunward of the $x = 0$ line (negative x) that falls within the condition of $\sqrt{y^2 + z^2} = 50R_{\mathrm{E}}$ is also flagged for removal. These conditions were deemed to be relatively conservative according to the Shue model (Shue et al., 1997), which gives the bow shock stand-off distance from Earth at approximately $11R_{\mathrm{E}}$ and described by $\sqrt{y^2 + z^2} = 28R_{\mathrm{E}}$ at the nose (Lin et al., 2010). The result of removing this data is shown in Figure 3.10, which displays the percentage of data that has been removed over each Carrington rotation (27.27 day period). The figure cuts off at 2005, beyond which *Wind* had no further bow shock encounters.

3.4 Data Calibration

We use ACE data from 1998-2017, beyond which there is no level-3 pitch angle distribution data publicly available, and *Wind* data from 1994-2021. To allow a direct comparison between ACE and *Wind* for the 19 years of overlap we studied (1998-2017), the *Wind* data set was re-sampled from the native 98s resolution to the same 128s time step applied to ACE.

Interplanetary coronal mass ejections (ICMEs) were not removed from the data. It has been noted that ICMEs can make up a significant fraction of the total magnetic flux threading the 1 AU sphere (Riley, 2007). However, we here treat ICMEs as part of the solar wind flow and note that an ICME encountered at 1 AU will previously have threaded the source surface and therefore have also (temporarily) contributed to the HMF (Owens and Crooker, 2006).

3.5 Conclusion

The data introduced in this chapter will be used later for various analyses. In Chapter 4, the radial magnetic field and the electron PA data from both ACE and *Wind* were used to determine the topology of the magnetic field. In Chapter 5, the topologies from Chapter 4 were used to calculate the Open Solar Flux. Finally, Chapter 6 uses the topologies from Chapter 4, the magnetic field, velocity, and the alpha and proton densities to investigate the variation of solar wind properties around true polarity reversals.

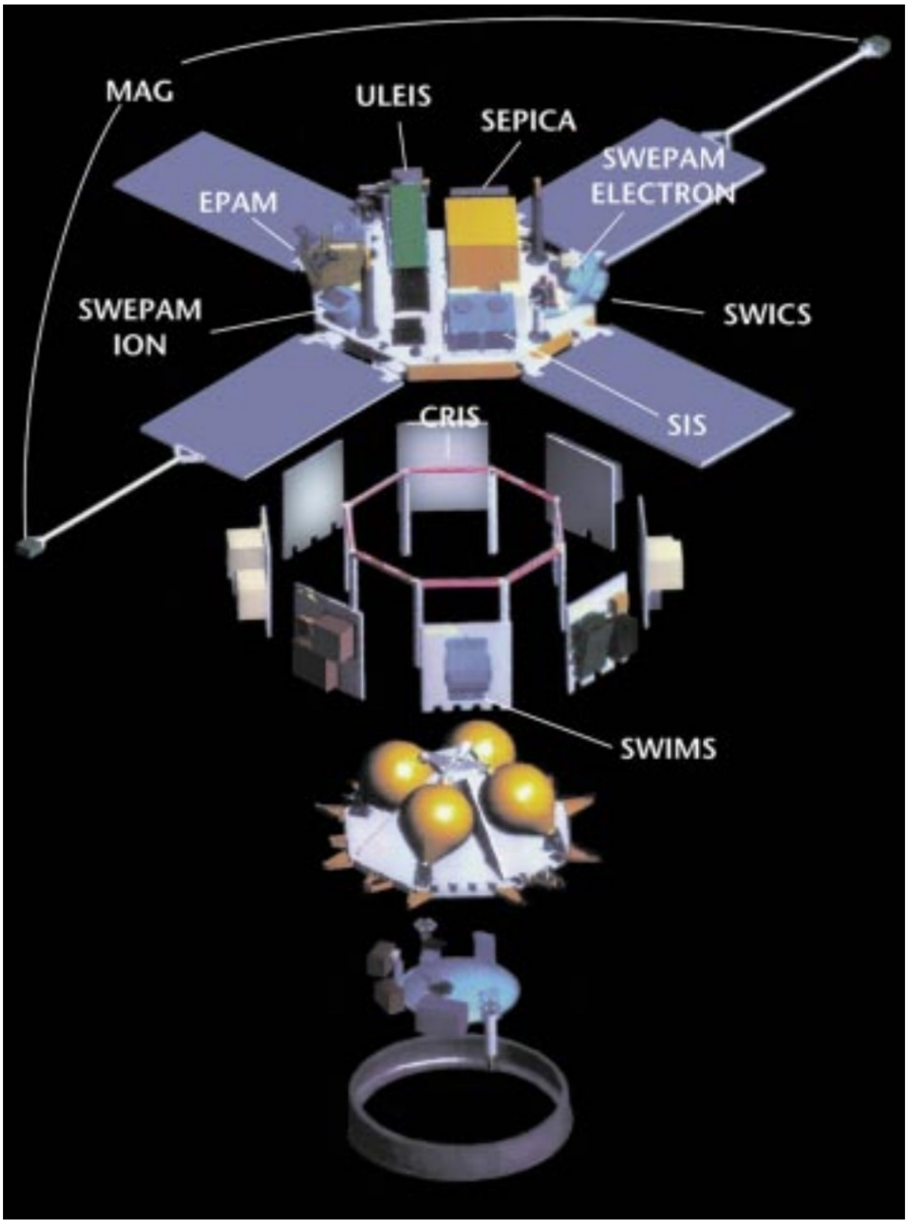
MAG
ULEIS
SEPICA
SWEPAM ELECTRON
EPAM
SWEPAM ION
SWICS
SIS
CRIS
SWIMS

Figure 3.4: Exploded view of the ACE spacecraft structure showing the position of all instruments. Image taken from Stone et al. (1998).

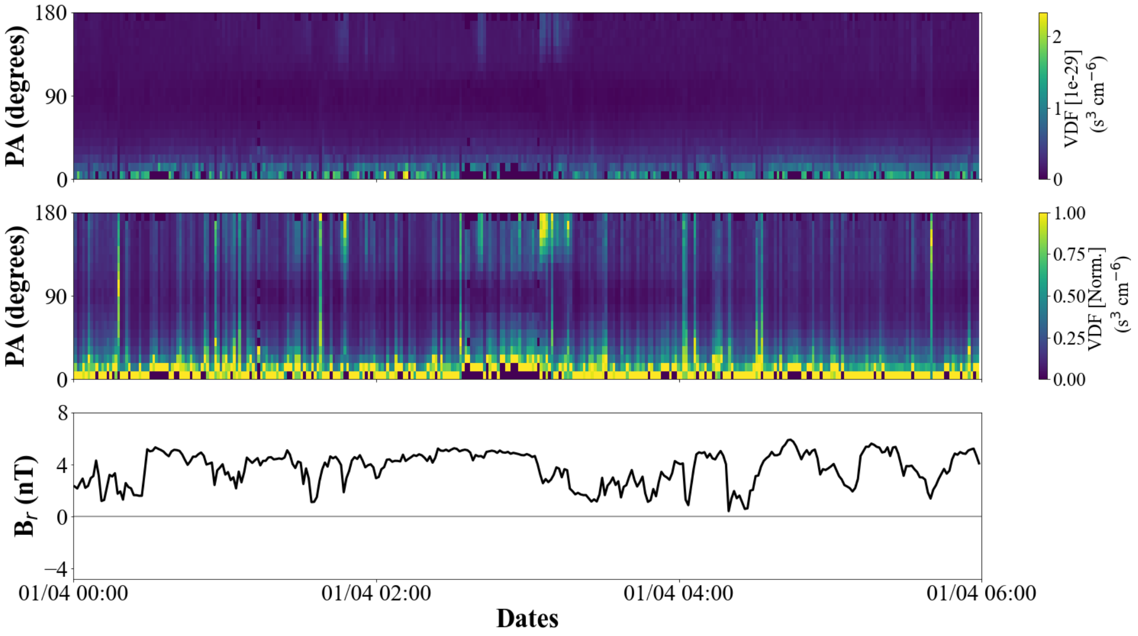

Figure 3.5: 6 hours of ACE observations from 4th January 2007. From top to bottom, the panels show: the variation with time of the suprathermal electron pitch angle distribution function ($f(\alpha, t)$, units s^{3}cm^{-6}), the same as the top panel normalised to the maximum and minimum flux at each time step, and the radial magnetic field in GSE coordinates (units nT).

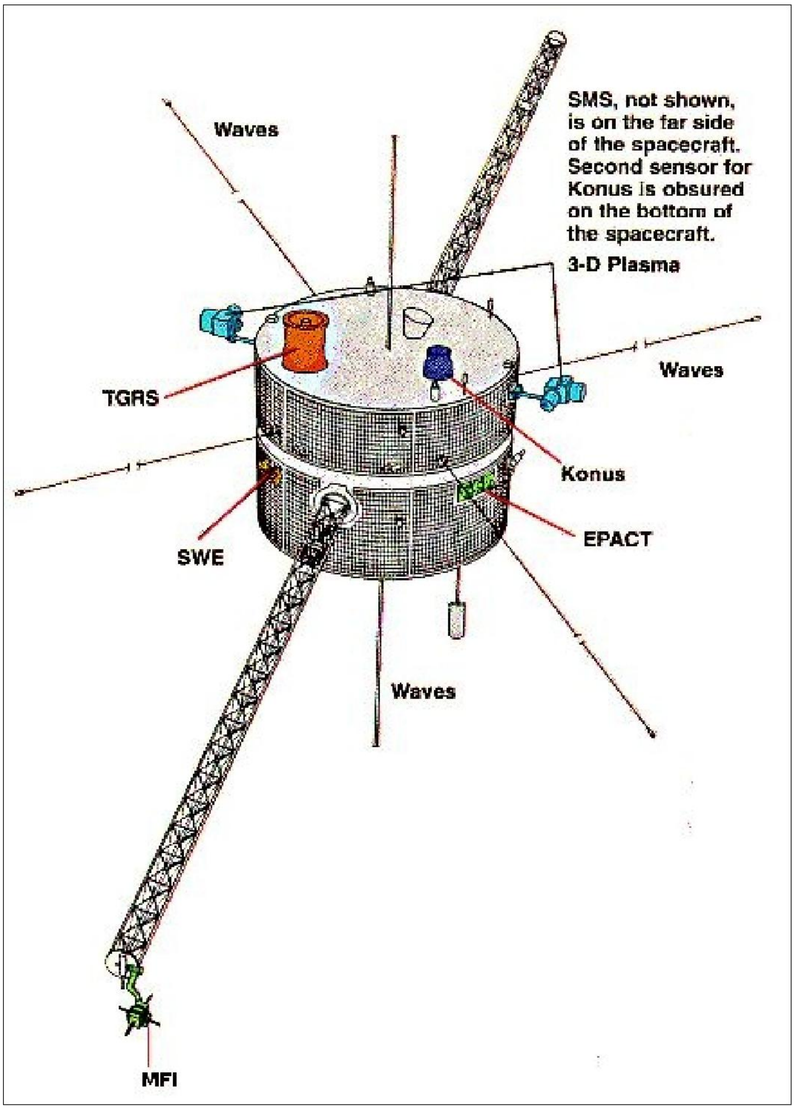
Waves
SMS, not shown, is on the far side of the spacecraft. Second sensor for Konus is obsured on the bottom of the spacecraft.
3-D Plasma
Waves
TGRS
Konus
EPACT
SWE
Waves
MFI

Figure 3.6: Schematic of the WIND spacecraft with instrument locations. Image credit: NASA.

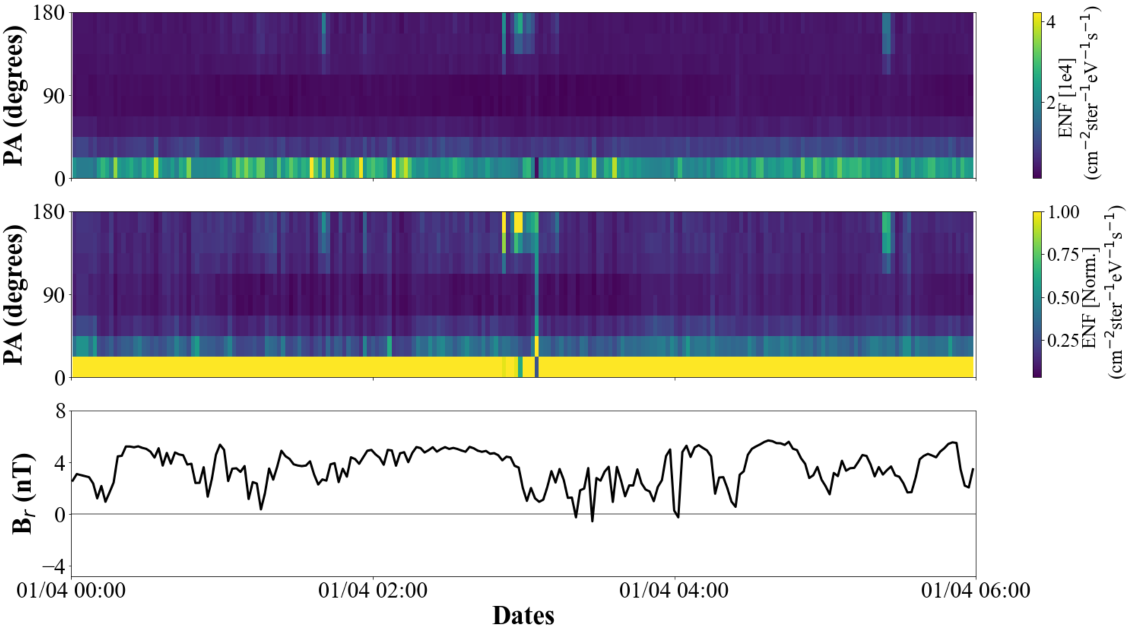

Figure 3.7: 6 hours of *Wind* observations from 4th January 2007. From top to bottom, the panels show: the variation with time of electron number flux (units cm^{-2}ster^{-1}eV^{-1}s^{-1}), the same as the top panel normalised to the maximum and minimum flux at each time step, and the radial magnetic field in GSE coordinates (units nT).

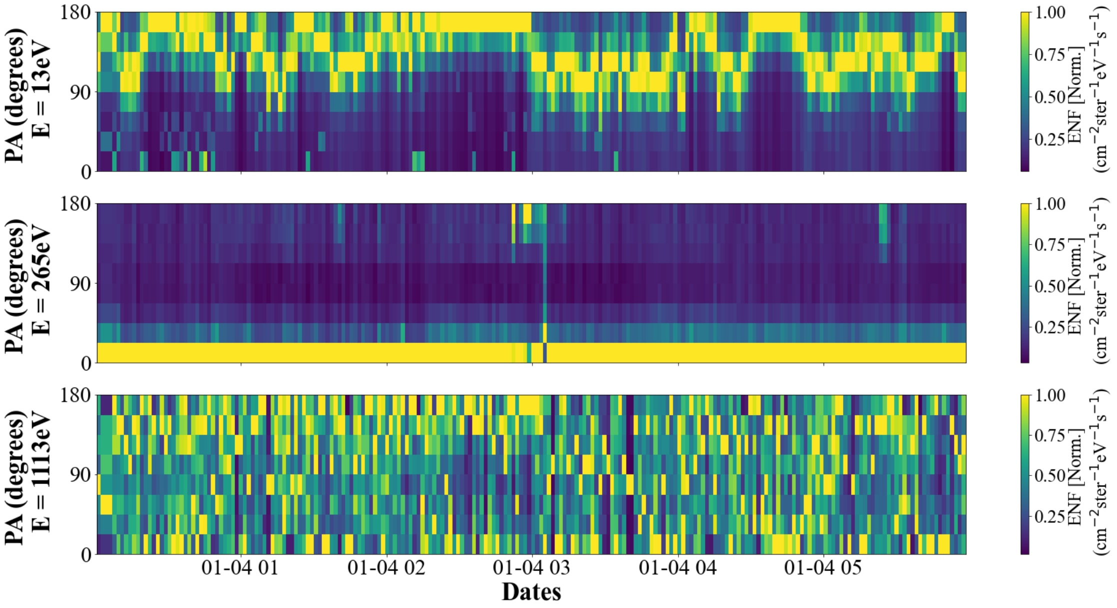

Figure 3.8: 6 hours of *Wind* observations from 4th January 2007. Each plot shows the variation with time of electron number flux (units cm^{-2}ster^{-1}eV^{-1}s^{-1}) normalised to the maximum and minimum flux at each time step for energies 13eV, 265eV, and 1113eV.

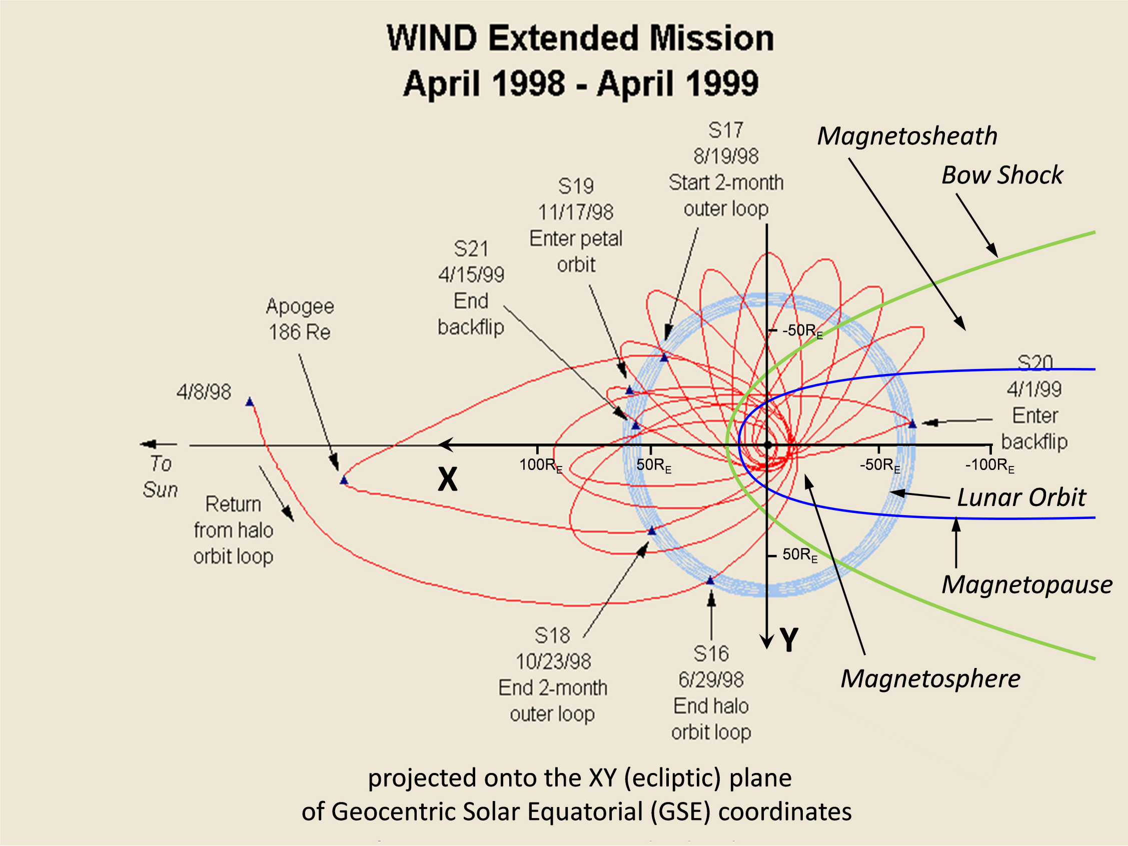
WIND Extended Mission
April 1998 - April 1999
S17
8/19/98
Start 2-month
outer loop
Magnetosheath
Bow Shock
S19
11/17/98
Enter petal
orbit
S21
4/15/99
End
backflip
Apogee
186 Re
4/8/98
-50R_E
S20
4/1/99
Enter
backflip
To
Sun
X
100R_E
50R_E
-50R_E
-100R_E
Lunar Orbit
Return
from halo
orbit loop
50R_E
Magnetopause
Y
S18
10/23/98
End 2-month
outer loop
S16
6/29/98
End halo
orbit loop
Magnetosphere
projected onto the XY (ecliptic) plane
of Geocentric Solar Equatorial (GSE) coordinates

Figure 3.9: A plot of *Wind's* orbit between April 1998 and April 1999 adapted from a NASA plot. Image credit: Mike Lockwood.

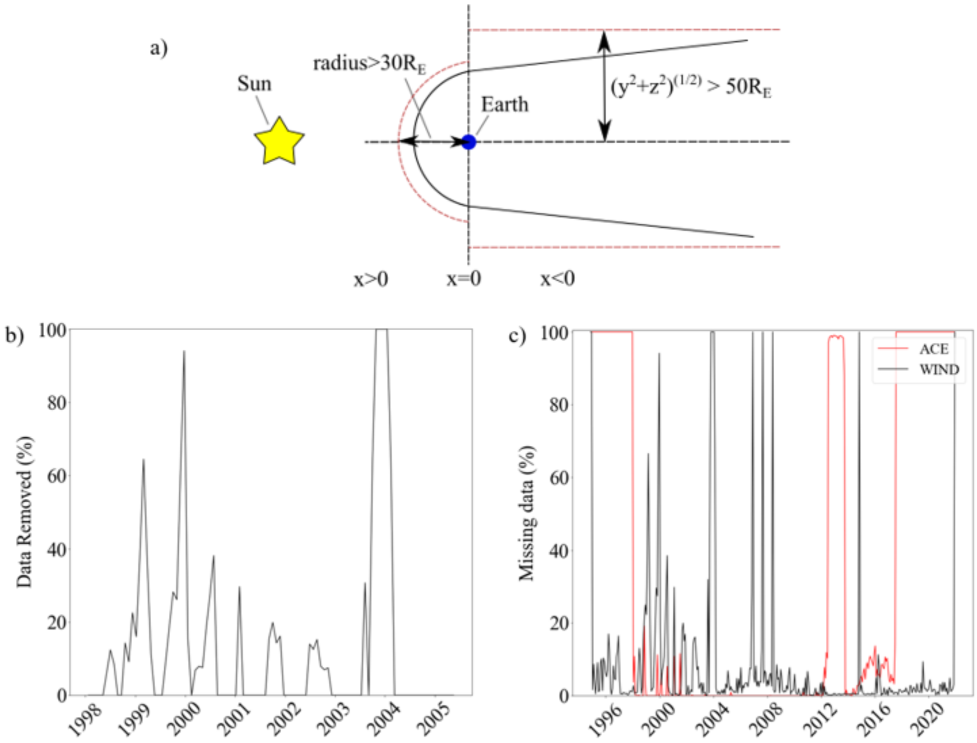

Figure 3.10: (a) A schematic of the conditions used to remove *Wind* data from within the magnetosheath (shocked solar wind) or magnetosphere in GSE coordinates. The *solid black line* represents the shape of the bow shock (not to scale) and the *red dashed lines* represent the conditions used to remove the undisturbed solar wind data. (b) The percentage of *Wind* data removed per Carrington rotation due to the encounter with the bow shock. (c) Comparison of missing data from spacecraft. The percentage of missing ACE (*red line*) and *Wind* (*black line*) data in each Carrington rotation between 1994 and 2021. The *Wind* missing data includes both data missing from the electron and magnetic fields data sets, and data subsequently removed from within the bow shock.

Chapter 4

Classifying the Topology of the HMF

The heliospheric magnetic field (HMF) is the extension of the magnetic field in the solar atmosphere (the corona) into space (e.g., Levine et al., 1977, Owens and Forsyth, 2013). That magnetic field is generated by the churning plasma, known as the solar dynamo, in the Sun's core. It is thought that the magnetic field is wound up and stored in the 'overshoot layer' just under the convective zone, where the rotation of the convection penetrates the top of the radiative zone (Charbonneau, 2020). When and where that field gets sufficiently large, magnetic buoyancy makes it rise up through the convective zone and emerge through the photosphere. Here it can be observed using a magnetograph, an instrument that uses Zeeman splitting of spectral lines to generate maps of the photospheric magnetic field called magnetograms (Beckers, 1968). Some loops of this emerged flux continue to rise through the solar atmosphere and eventually get dragged away from the sun in the solar wind flow of plasma, driven by the very high temperatures of the solar corona. This HMF fills a huge volume that surrounds the entire solar system, which we call the heliosphere. The outer boundary of the heliosphere is where the solar wind, and the embedded HMF, meets interstellar space.

Understanding the portion of the coronal field that maps into the heliosphere (what we term open solar flux, OSF) is central to space weather, as the OSF forms the heliosphere, magnetically connects the Sun to the planets, and dominates the motion of energetic particles. In order to determine the OSF, the Sun's magnetic field must be classified by topology. *In-situ* electron and magnetic field data are used to determine the global topology of the HMF using the combined measurements from the Wind and ACE spacecraft spanning 1994 – 2021.

This chapter describes the topologies used for the OSF correction in Chapter 5 and the superposed epoch analysis in Chapter 6. The work presented in this chapter has been adapted in part from Frost et al. (2022), the goal of which was to correct the OSF for local field inversions and quantify the errors associated with this.

The problem is introduced in Section 4.1, which reviews previous methods of topology classification. In Section 4.2 the combination of magnetic field and suprathermal electron data is used to determine the topology of the magnetic field. In Section 4.3 the method is outlined, which identifies the relationship between the different electron pitch angles (PAs) required to determine the topology of the magnetic field. This takes into account the different data resolutions and the number of PA bins needed to identify a Strahl signature from both spacecraft. In Section 4.4 the conditions identified in Section 4.3 are constrained using the observational results from 4 studies: Gosling et al. (1992), Anderson et al. (2012), Skoug et al. (2000) and Pagel, Crooker and Larson (2005). Finally, the main results are summarised in Section 4.5.

4.1 Introduction

Heat flux carried by electrons is an important process in the corona and solar wind as it transports energy over large distances and is a major factor in setting the spatial variation of temperature which drives the outflow of plasma in the solar wind. Solar wind electron distributions can be separated into three components: a thermal core, a suprathermal near-isotropic halo, and a suprathermal field-aligned "strahl" (Feldman et al., 1975), as illustrated in Figure 4.1. The thermal core has a temperature of $10^5 K$ and it makes up approximately 95% of the total solar wind electron density. The halo population has a temperature of $7 \times 10^5 K$ and the strahl has a similar temperature in the field-aligned direction (but is anisotropic with a lower field-perpendicular temperature). Together, strahl and halo make up the remaining 5% of the solar wind electron population (Maksimovic et al., 2005).

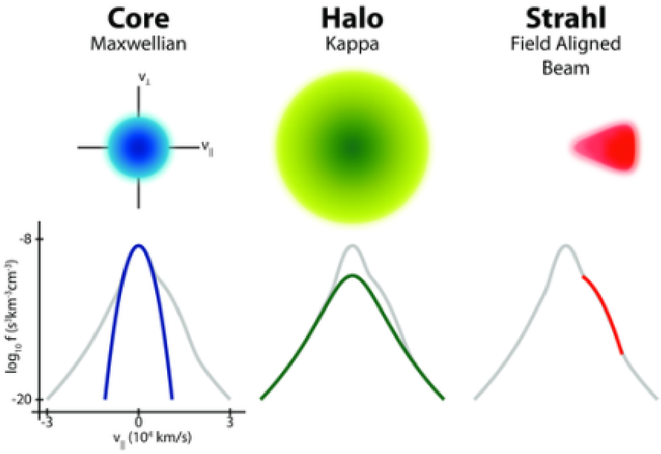

Figure 4.1: Diagram from Graham (2018), showing the different solar wind electron populations: core (blue), halo (green), and strahl (red), which have Maxwellian, Kappa, and field-aligned beam forms, respectively. (Top) the two-dimensional velocity distribution functions, in field-parallel ($v_\parallel$) and field-perpendicular ($v_\perp$) velocity space, f($v_\parallel$,$v_\perp$) and (bottom) the one-dimensional cut through the distribution in the field-parallel direction, f($v_\parallel$). Image credit: Marc Pulupa.

The work presented here takes advantage of the properties of the field-aligned strahl. As the strahl particles move away from the Sun, scattering collisions become sufficiently infrequent that both their energy and magnetic moment are conserved. The conservation of energy and magnetic moment results in a distribution of suprathermal electrons that is focused by the decreasing field into a beam along the magnetic field (Hammond et al., 1996).

At 1 AU in the solar wind, the mean free path is comparable with the typical length scales of the system and electrons should experience negligible coulomb collisions (ŠtveráK et al., 2008). With Sun's magnetic field decreasing with distance, the strahl beam will continue to narrow with heliocentric distance (in the absence of other influences). From observations, strahl beams are often significantly larger than predicted,

$> 20^{\circ}$, so adiabatic focusing cannot be the sole effect experienced by these particles (ŠtveráK et al., 2008).

Since the strahl component carries heat flux outward (away) from the Sun's corona, the presence of this field-aligned beam can be taken as evidence of connectivity to the Sun (Lin and Kahler, 1992, Kahler and Lin, 1994).

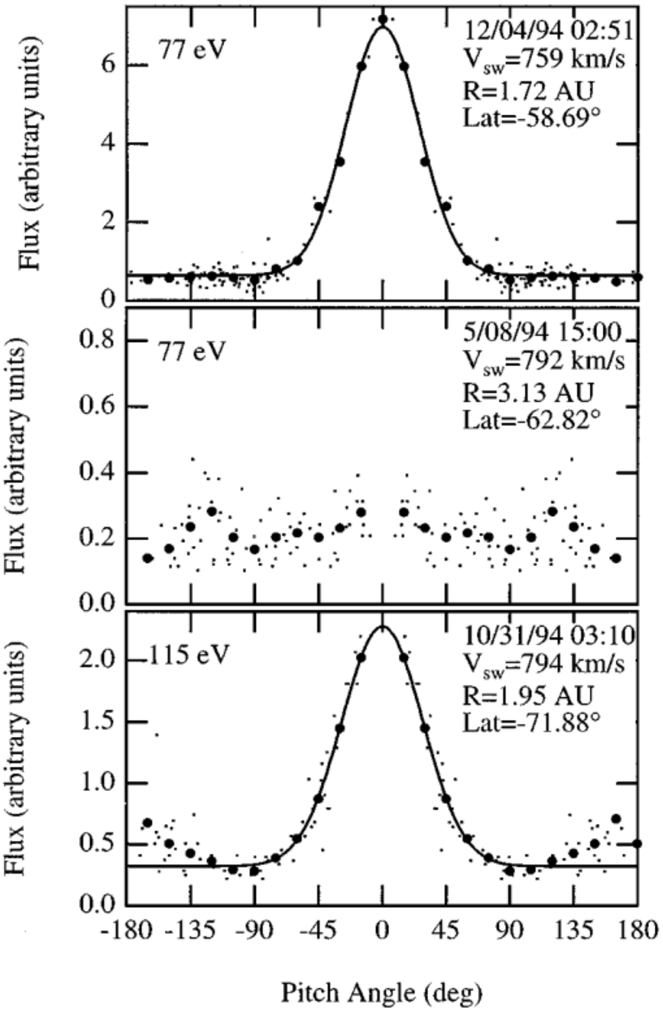

Figure 4.2: Figure 1 from Hammond et al. (1996), showing three pitch angle distributions seen in the high-speed solar wind. Top two panels show 77 eV electrons (9×10^{5} K) while the bottom panel is 115 eV electrons (1.3×10^{6} K). Dots are the measured data and filled circles are these data binned into 15° wide pitch angle bins. The solid line in the top panel is a Gaussian fit to all the data, whereas in the bottom panel, it is the sum of two Gaussian's fitted with peaks at α of 0 and 180°.

Hammond et al. (1996) outlines how the distribution of the strahl electrons can be used to determine the topology of the field. Figure 4.2 shows the distribution functions of electrons at energies, typical of strahl electrons, as a function of pitch angle, $\alpha = \tan^{-1}(v_{\parallel}/v_{\perp})$. Because strahl electrons move either parallel or anti-parallel to the field **B** they have distributions centred on α of zero (parallel to **B**, $v_{\parallel} > 0$) or 180 degrees (anti-parallel to **B**, $v_{\parallel} < 0$).

In the top panel of Figure 4.2, the strahl peak is well resolved at $\alpha = 0$. At other times the strahl appears to be absent, lacking a clearly resolved peak, as in the middle panel. Less often, a small counter-streaming component is seen, as in the lower panel, which shows a strong flux around the parallel direction ($\alpha = 0$) and a lower flux around the anti-parallel direction $\alpha = \pm 180°$. Only data with a clearly defined peak such as those shown in the top and bottom panels of Figure 4.2, are used.

The method employed in this chapter and Chapter 5 to categorise the strahl electrons, is a method adapted from Owens et al. (2017), based on the relative flux intensity combined with the radial magnetic field to determine the topology of each single-point magnetic field measurement. More detail follows in the next section.

4.2 Determining Field Topology

Using the field-aligned strahl, it is possible to determine if a magnetic field line is directly connected to the Sun's surface or is locally inverted. Figure 4.3 shows how the combination of electron strahl and magnetic field data can be used to distinguish between: open flux (points 1 and 3), recently emerged open flux (i.e. open flux that emerged through the source surface relatively recently and forms loops that are less distended into the heliosphere) (point 2), inverted flux (4), and flux that has been disconnected from the Sun (5).

For point '1' the radial magnetic field is negative in a "Toward" ("T") field sector, i.e. the magnetic field is directed towards the Sun: the strahl is directed anti-parallel to the direction of the magnetic field because it is directed away from the Sun. Thus the field is open and does not show evidence of local inversion. The equivalent case for an

"Away" ("A") (positive B_r sector) is shown in '3'.

Point '2' gives an example of counterstreaming strahl, where the strahl is travelling in both parallel and anti-parallel directions. In the literature, field lines with counterstreaming electron fluxes have often been referred to as "closed" (e.g. Gosling et al., 1987). There are two problems with using this terminology here. Firstly there is no topological difference between these field lines with counterstreaming strahl and field lines that carry only unidirectional strahl (for example, strahl does not distinguish field lines that extend well into the heliosphere from those that form closer loops). Secondly, we here use the term "closed" to mean field lines that do not extend beyond the solar corona when defining the coronal source surface. The real difference between the unidirectional strahl (points 1 and 3) and the bi-directional strahl (point 2) is the distance along the field line loop and hence how far the loop extends out into the heliosphere. It is more than a matter of convenient definition that we class field lines with counterstreaming electrons as "open". The reason is that they contribute to the tangential pressure in the heliosphere near to the Sun which gives the latitudinal independence of the radial field (Suess and Smith, 1996, Suess et al., 1996) that is employed when estimating OSF from *in-situ* data. In this thesis, we refer to field lines with counterstreaming strahl as "newly-opened" because the counterstreaming reveals that they have been open for a shorter time (i.e., they first emerged through the source surface relatively recently), such that the field-aligned distance to both of the loop's foot-points in the solar corona is short enough that strahl electrons from both can reach the spacecraft with sufficient fluxes to be detected. The evolution from newly-opened to open by this definition is therefore not sudden and described by a time constant, and could be treated in the same way that Lockwood and Owens (2014) accounted for the evolution of streamer belt flux into coronal hole flux.

Point '4' gives an example of an HMF inversion, where the radial field component is negative (directed towards the Sun) and the strahl is parallel to the magnetic field (so also directed towards the Sun in the folded region, even though its ultimate direction of travel is away from the Sun).

Finally, point ‘5’ gives an example of magnetic field that is disconnected from the Sun, which would give a complete absence of strahl, called a “heat flux dropout” (McComas et al., 1989, Pagel, Crooker and Larson, 2005, Pagel, Crooker, Larson, Kahler and Owens, 2005). Note, that in some cases the strahl may be missing although the field line is not completely disconnected from the Sun. This usually occurs when the loop has been disconnected at the nearer foot-point but is still connected topologically by the other foot-point. If the field-aligned distance to the still-connected foot-point is large enough the strahl will be scattered to undetectable low fluxes and no strahl is seen.

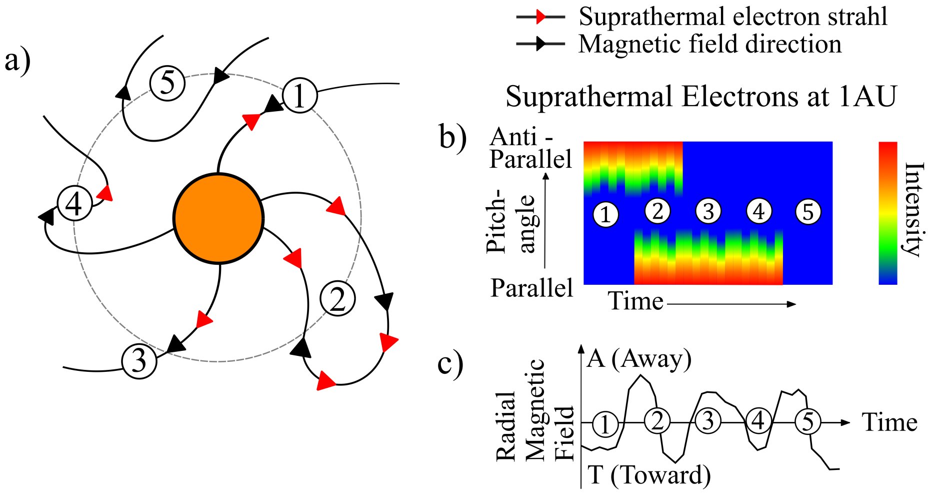
Suprathermal electron strahl
Magnetic field direction
a)
⑤
①
④
②
③
Suprathermal Electrons at 1AU
b)
Anti - Parallel
Pitch-angle
Parallel
① ② ③ ④ ⑤
Time
Intensity
c)
Radial Magnetic Field
A (Away)
T (Toward)
① ② ③ ④ ⑤
Time

Figure 4.3: Schematic modified from Owens and Forsyth (2013) displaying the topology of the HMF as inferred from suprathermal electron (STE) observations. (**a**) the heliographic equatorial plane, with heliospheric magnetic field lines (*black arrows*) and the STE flux (*red arrows*) for different magnetic topologies. (**b**) the suprathermal electron pitch-angle time spectrogram. (**c**) the radial magnetic field time series that would be seen as the structure shown in (**a**) is constant and rotates over the spacecraft. The combination of electron and magnetic data can be used to distinguish between: open flux (points *1* and *3*), newly emerged open flux (point *2*), inverted flux (*4*), and flux that has been disconnected from the Sun (*5*).

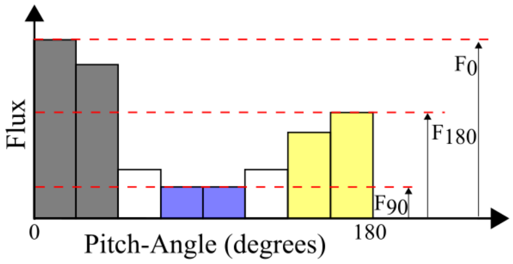

$$PAB_0 = 100 * (|F_0 - F_{90}|)/F_{90}$$
$$PAB_{180} = 100 * (|F_{180} - F_{90}|)/F_{90}$$
$$PAO_0 = 100 * (|F_0 - F_{180}|)/F_{180}$$
$$PAO_{180} = 100 * (|F_{180} - F_0|)/F_0$$

Figure 4.4: A schematic of a suprathermal electron pitch-angle distribution and the criteria used to algorithmically determine the strahl direction. F_{90} is the background flux (taken from the *blue shaded bars*, i.e., pitch angles α near 90°), F_0 is the flux at pitch-angles near 0° (taken from the *grey shaded bars*), and F_{180} is the flux at pitch-angles near 180° (taken from the *yellow shaded bars*). PAB is the percentage above the background flux, and PAO is the percentage above the flux in the opposite direction. Thresholds on these values are used to classify the existence of strahl in the field-parallel direction and/or the field anti-parallel direction.

4.3 Method

From the combined ACE/*Wind* dataset, HMF topologies can be determined from the combination of *in-situ* magnetic field and strahl data algorithmically for each 128 s interval. Figure 4.4 shows a schematic of a single integration interval of *Wind* suprathermal electron pitch angle data for, in this example, 272 eV and in 8 pitch angle (PA) bins (ACE contains 20 PA bins) equally spaced between 0 and 180 degrees in relation to the direction of the local magnetic field. First, the background flux is calculated from the average of the centre 2 PA bins, F_{90}, and the parallel flux is calculated from the average of the first 2 PA bins, giving F_0. The same method is applied for the anti-parallel flux, F_{180}. Next, the existence of a strahl or strahls is determined. To check for the existence of a parallel strahl, we compute the percentage by which F_0 exceeds F_{90}, termed the percentage above background, PAB$_0$. The equivalent parameter, PAB$_{180}$, is computed for the anti-parallel strahl. If neither PAB$_0$ or PAB$_{180}$ meet the required threshold, the interval is unclassified. If only PAB$_0$ or PAB$_{180}$ meets the threshold, the interval is HMF with a single (direct) connection to the Sun and will be either inverted or uninverted HMF, depending on the HMF polarity.

When both PAB$_0$ and PAB$_{180}$ meet the required threshold to define strahl, there arises the possibility that the interval should be classified as counterstreaming (CS) strahl, suggesting newly emerged loops in the heliosphere (however, see also Gosling et al., 2001). An additional threshold is introduced, comparing the magnitudes of the two strahl, in terms of the percentage above the opposite (PAO). If both PAO$_0$ and PAO$_{180}$ are below the required threshold, the interval is CS. Otherwise, if PAO$_0$ or PAO$_{180}$ exceeds the required threshold, the interval represents a single connection in the direction of the highest flux and will be either inverted or uninverted HMF, depending on the HMF polarity. Optimisation of PAB and PAO thresholds to agree with previous studies will be investigated in more detail in the next section.

4.3.1 Calibration Between Spacecraft

The topology classifications derived from ACE and *Wind* were compared to find optimal strahl classification criteria to give a good agreement between the two. We compared ACE and *Wind* topologies over the period 1998-2011 when there was good data coverage from both spacecraft. In Figure 3.10c, between 1998-2011, the ACE data is essentially continuous and Wind has less than 10 % missing data from most CRs. In order to apply the same PAB and PAO criteria to both spacecraft for strahl identification, we need to account for the different pitch-angle (PA) resolution of the data.

A number of different PA bin combinations and weightings were attempted to give consistent strahl identification across both spacecraft. The closest agreement is found by using two PA bins for *Wind* to define F_0, F_{90} and F_{180}, as shown in Figure 4.4, and four PA bins for ACE.

4.4 Results and Discussion

4.4.1 Topology of the Magnetic Field

Using the method outlined in Section 4.3, the HMF topology of each point measurement can be determined. Figure 4.5 shows an example of the topology determined from 12 hours of ACE data on 14th January 2007. Panel **A** shows the velocity distribution function (VDF) as a function of pitch angle and time as a fixed energy and hence velocity v, $f(\alpha, t)$, of suprathermal electrons at 272 eV from the ACE SWEPAM instrument (McComas et al., 1998). Panel **B** shows the same as **A**, but it has been normalised to the maximum and minimum flux at each time step. The yellow and green band seen clearly in **B**, centered on PA 180^o (anti-parallel to the field) is the electron strahl beam.

Panel **C** shows that initially, the radial field is toward the Sun, and the strong strahl, being anti-parallel to the field is away from the Sun. This is therefore Topology 1 in Figure 4.3. Around 07 UT there is some very weak counterstreaming strahl flux as well. However, that weak flux does not exceed the threshold needed for this to be classified as counterstreaming: this situation arises because we need thresholds that ensure analysis of Wind and ACE data are consistent in their detection of counterstreaming.

Around 12 UT, the field changes to anti-sunward ($B_r > 0$), however, the dominant strahl flux remains anti-parallel and so is sunward. This is inverted flux, similar to point 4 in Figure 4.3, but for a field line that leaves the solar corona in the opposite direction to that illustrated by 4 in Figure 4.3. Again a very weak counterstreaming electron signature can be seen but does not exceed the threshold for classification.

Just before 14 UT the field flips back to sunward ($B_r < 0$) and again the Strahl remains anti-parallel so the Strahl direction has returned to anti-sunward, and the situation seen at the start of the interval is resumed. It is interesting to note that the very weak counterstreaming strahl expands towards 90° pitch angle towards the end of the interval, which indicates a greater degree of scattering and we can infer that the HMF field loops observed are extending deeper into the heliosphere.

Hence Figure 4.5 shows an interval of open flux sunward HMF in which there is a brief interval (between about 12 and 14 UT) when folded, inverted flux is detected. For periods such as this, classifying the topology is relatively straightforward. However, for intervals without a clear uni-directional strahl there is the complication of determining if the strahl is stronger in a single direction or if it is a true counterstreaming field. This is where the PAB and PAO conditions outlined in Figure 4.4 are required.

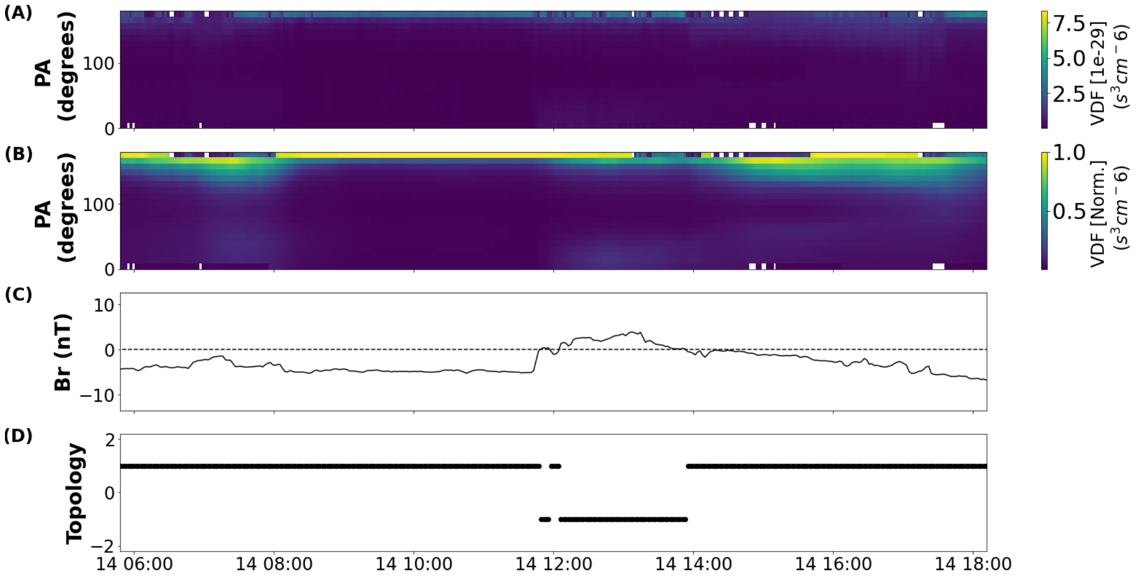

Figure 4.5: 12 hours of ACE observations from 14th January 2007. Panels show: **A**) the variation with time of the suprathermal electron pitch angle distribution function ($f(\alpha, t)$, units s^{3}cm^{-6}), **B**) the same as **A** normalised to the maximum and minimum flux at each time step, **C**) the radial magnetic field (nT), and **D**) topology indicator of the magnetic field. $+1$ shows times where the field is topologically open and -1 shows times where the field is topologically inverted.

Figure 4.6 shows a single carrington rotation (CR) of ACE observations from October-November 2008. As in Figure 4.5B, Figure 4.6A shows the pitch angle distribution function of suprathermal electrons at 272 eV from ACE. Panel B shows the variation of the percentage above the background (PAB) for both strahl in the parallel (0^o, *black line*) and the anti-parallel (180^o, *red line*) direction. Panel C shows the variation of the percentage above the opposite (PAO) for both strahl in the parallel (0^o, *black line*) and the anti-parallel (180^o, *red line*) direction. Figure 4.6 shows that PAB and PAO can vary from close to zero up to about 200$\%$ and this range is found to cover almost all

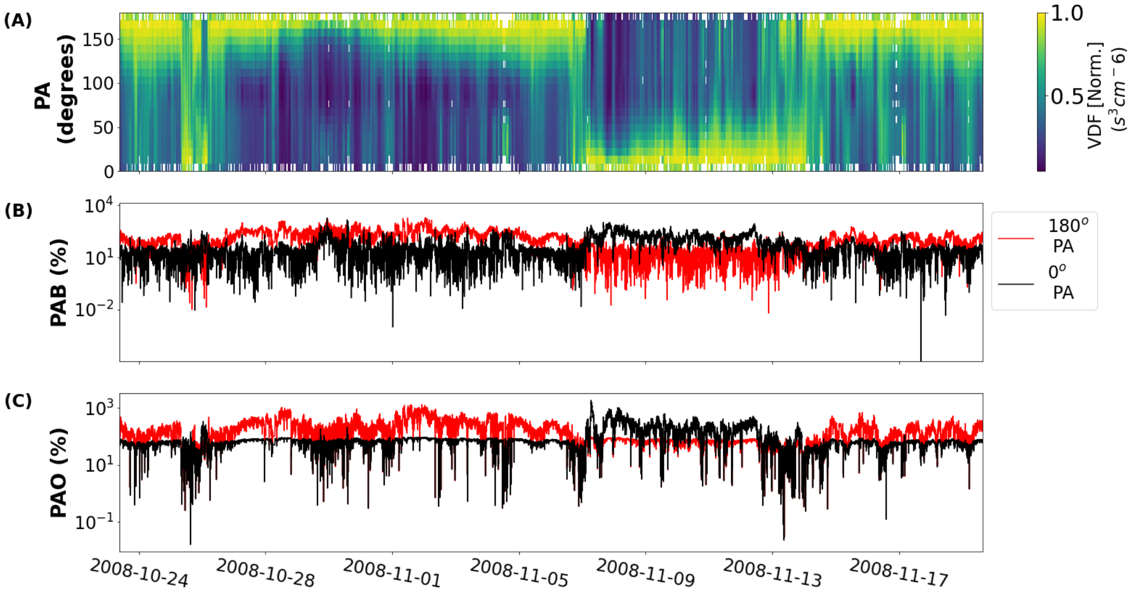

Figure 4.6: A single Carrington-rotation of ACE observations from 23rd October to 19th November 2008. Panels show: **A**) the suprathermal electron pitch angle distribution function ($f(\alpha, t)$ for an energy E $=$ 272 eV, units s^3cm^{-6}), normalized to the maximum and minimum flux at each time step, **B**) the PAB at 0^o PA (*black line*) and 180^o PA (*red line*), and **C**) the PAO at 0^o PA (*black line*) and 180^o PA (*red line*). Note that both PAB and PAO are shown on logarithmic scales.

the full data series employed here, so we look at the effect of adopting thresholds for PAB and PAO that cover this range 0-200$\%$.

Figure 4.7 shows the variation of the percentage occurrence of inverted, uninverted/open, counterstreaming, and undetermined flux with changing PAB and PAO thresholds. For each combination of PAB and PAO, the average occurrence percentage of each topology was calculated for the entire 1994-2021 period of the combined ACE-Wind data set. It should be noted here that the WIND energy channel used here is 292 eV as this is closest to the ACE energy of 272 eV. Since PAO and PAB are ratios, fluxes will be similarly influenced by this small energy difference and so ratios are only marginally influenced by it.

In the bottom left of the plots (where both PAB and PAO are low), there is a high percentage of inverted (plot A) and a high percentage of uninverted (plot B). Low PAB makes it easier for more intervals to meet the condition needed for a strahl to exist, resulting in a greater amount of inverted and uninverted and fewer undetermined

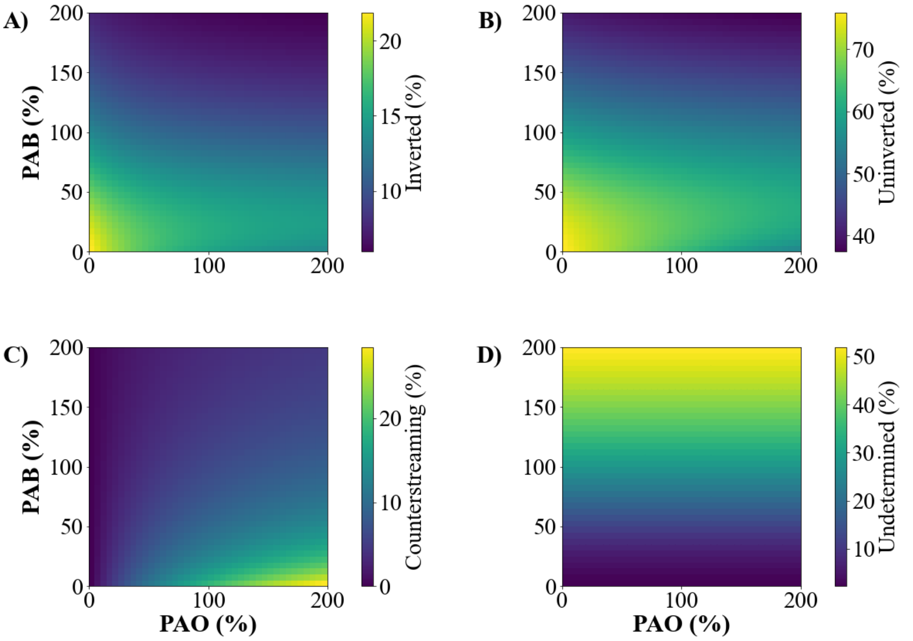

Figure 4.7: Average over the interval 1994 to 2021 as a function of strahl identification criteria, PAO and PAB. Panels show: **A**) Inverted, **B**) Uninverted, **C**) Counterstreaming and **D**) Undetermined flux percentages.

intervals. Low PAO requires both strahl directions to be nearly identical to be identified as CS, therefore the amount of strahl is at a minimum here (plot C). At higher PAO (and low PAB) the conditions for a strahl to be classified as CS is easier to meet as the strahl can be up to double the size of the opposite direction and still meet this condition. This increases the amount of CS (plot C) and decreases the inverted (plot A) and uninverted (plot B) percentages, while undetermined (plot D) remains the same. As PAB increases, the criteria for a strahl to exist becomes more restrictive, resulting in higher amounts of undetermined (plot D) and lower amounts of the other topologies. Varying the PAB and PAO greatly changes the ratio of the topologies. Therefore, these variables need to be constrained using comparisons with the results of previous studies.

4.4.2 Constraining the Strahl Conditions

In order to automatically and reproducibly classify each data point in the approximately 27-year data set, we require an algorithmic method to identify suprathermal electron strahl and the resulting magnetic field topologies. As discussed above, Owens et al.

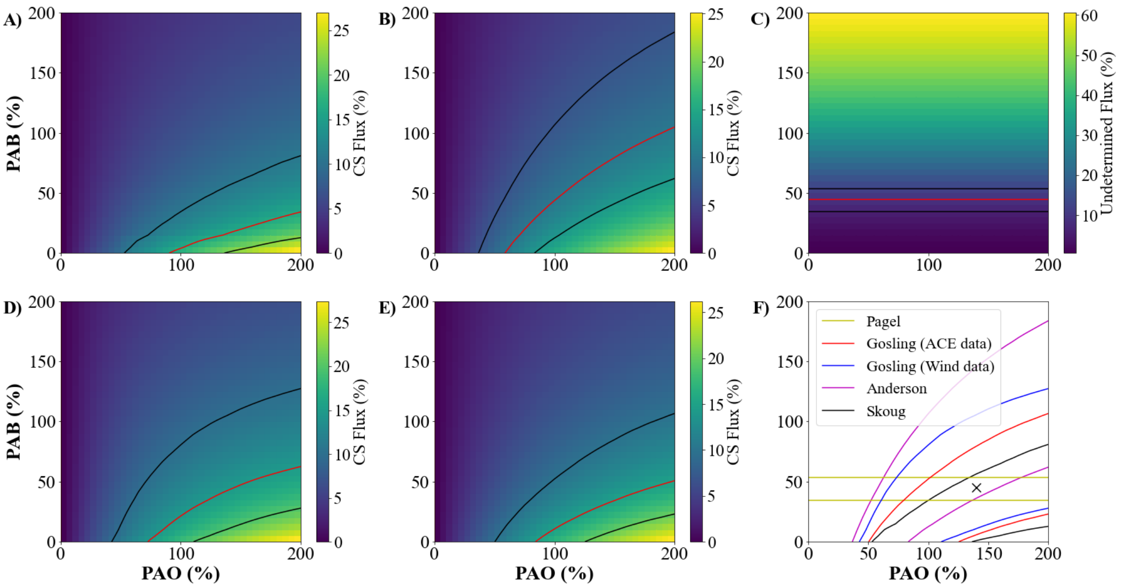

Figure 4.8: Selecting strahl identification criteria using previous studies. **A**) Average CS flux measured by ACE between 3/2/2008 - 27/10/2008, the period of study from Skoug et al. (2000). CS values of 16% (*red line*) with 1-sigma range about the reported percentage (*black lines*). **B**) Average CS flux measured by ACE between 1998-2002, the period of study from Anderson et al. (2012). CS values of 10% (*red line*) with 1-sigma range about the reported percentage (*black lines*). **C** Average undetermined flux measured by *Wind* between 1995-1998, the period of study from Pagel, Crooker and Larson (2005). Disconnected flux of 10% (*red line*) with 1-sigma range about the reported percentage (*black lines*). **D**) Average CS flux measured by *Wind* at solar maximum, same solar cycle period used by Gosling et al. (1992). CS values of 14.7% (*red line*) with 1-sigma range about the reported percentage (*black lines*). **E**) Same as plot **D**, but with ACE data. **F**) Values of PAO and PAB that are consistent with previous studies: *black lines* (**A**), *magenta line* (**B**), *yellow horizontal lines* (**C**), *red and blue lines* (**D** and **E**). The *black cross* in the center of the region indicates the conditions used for PAO and PAB in this work.

(2017) used a simple method based on the electron flux close to the 0 and 180-degree pitch-angle bins and applied a threshold as a percentage of the "background" flux, taken to be the flux close to 90-degree pitch-angle bin. A (somewhat arbitrary) threshold of 30 % was then used as a threshold to identify a Strahl and counterstreaming intervals. That same basic approach is adopted here but, in addition to the pitch-angle bin choices detailed in the previous section, we investigate the effect of the choice of the strahl thresholds. In particular, we seek to select values that replicate previous studies which have utilised classification by expert observers.

Using IMP8 data, Gosling et al. (1992) reported an average CS occurrence of 14.7 % for each year around solar maximum from August 1978 to December 1990. Skoug et al. (2000) reported an occurrence of 16 % of CS for a 9-month period, days 34 - 300 of 1998, using ACE data. Using an automated identification method, Anderson et al. (2012) gave a CS occurrence of 10 % from ACE data between 1998 to 2002.

For each of these studies, we determine the PAB and PAO thresholds which are consistent with the reported CS and disconnected flux rates to within $\pm 33\,\%$ (i.e. a 1-sigma range about the reported percentage). Figure 4.8 shows how the PAB and PAO thresholds were constrained. The heat maps show the variation of CS (and unclassified for Figure 4.8C) with varying PAB and PAO, and the solid lines trace the values of CS (and unclassified) consistent with the previous studies.

For the Skoug et al. (2000) and Anderson et al. (2012) studies, we can reproduce the exact periods of study here. Figure 4.8A shows the parameter space consistent with Skoug et al. (2000) which reported a CS occurrence rate of 16 % over days 34-300 of 1998. The red line in Figure 4.8A indicates the PAB and PAO values that produce this 16 % CS occurrence, and the black lines on the plot (and the black lines in Figure 4.8F) indicate thresholds of ± 33 % (explicitly 10.7 % and 21.3 %).

Figure 4.8B shows the parameter space consistent with Anderson et al. (2012) which reported a CS occurrence rate of 10 % over the period 1998-2002. The red line Figure 4.8B indicates the PAB and PAO values which produce this 10 % CS occurrence, and the black lines on the plot (and the magenta lines in Figure 4.8F) indicate thresholds of ± 33 % (explicitly 7.7 % and 13.3 %).

For Gosling et al. (1992), the actual period of study is not present in our data set. Since the CS occurrence rate is reported for the years around solar maximum, we take an equivalent period from ACE and *Wind*. Explicitly, we isolate one year of data from the peaks of Solar Cycles 23 and 24, namely 2000 and 2014 (peak of solar maximum as identified by sunspot number SILSO World Data Center, 2022), for each spacecraft and use that to constrain the CS occurrence. The red lines in Figure 4.8D and Figure 4.8E indicates the PAB and PAO values which produce the reported 14.7 % CS occurrence using data from *Wind* and ACE respectively. The black lines on the plots (and the blue and red lines in Figure 4.8F) indicate thresholds of ± 33 % (explicitly 9.8 % and 19.5 %).

Finally, Pagel, Crooker and Larson (2005) reported a 10 % occurrence of disconnected flux from 1995 to 1998 using data from *Wind*. The red line in Figure 4.8C indicates the PAB and PAO values that produce this 10 % disconnected flux occurrence, and the black lines (and yellow horizontal lines in Figure 4.8F) indicate thresholds of ± 33 %.

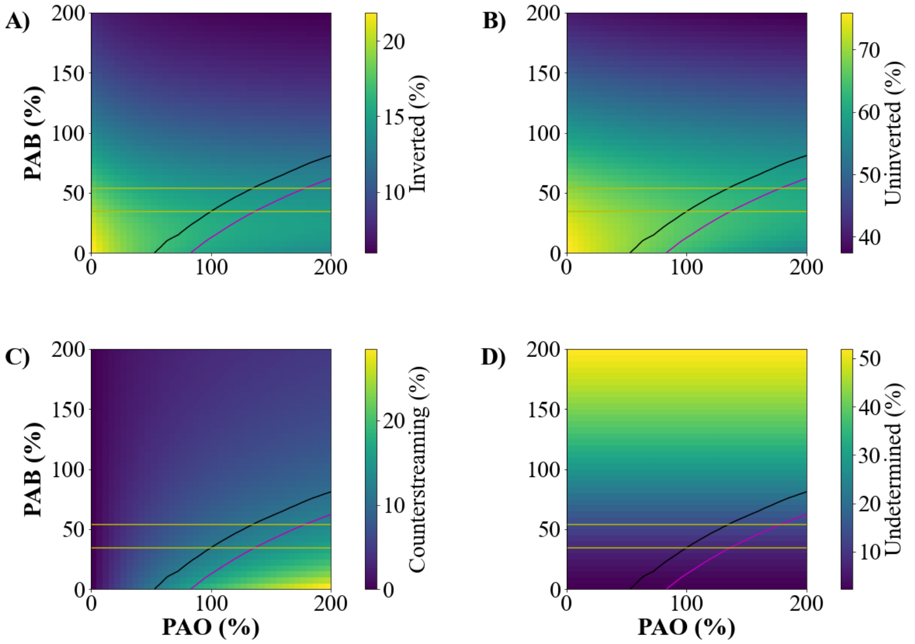

Figure 4.9: Adapted from Figure 4.7, average over the interval 1994 to 2021 as a function of strahl identification criteria, PAO and PAB. Panels show: **A**) Inverted, **B**) Uninverted, **C**) Counterstreaming and **D**) Undetermined flux percentages. On each plot, the lines correspond to criteria outlined in Figure 4.8.

Figure 4.8F shows the region of PAB and PAO values that are in agreement with the previous studies. For the purpose of this study, the PAB and PAO values are taken from the center of this region as 45 % and 140 %. Figure 4.9 shows the variation of the percentage occurrence of inverted, uninverted/open, counterstreaming, and undetermined flux with changing PAB and PAO thresholds, as shown in Figure 4.7. Adding the constrained conditions from Figure 4.8F, we can see that the variation of the topologies within this region are very small, indicating that these acceptable values will provide consistent magnetic field topologies using this method.

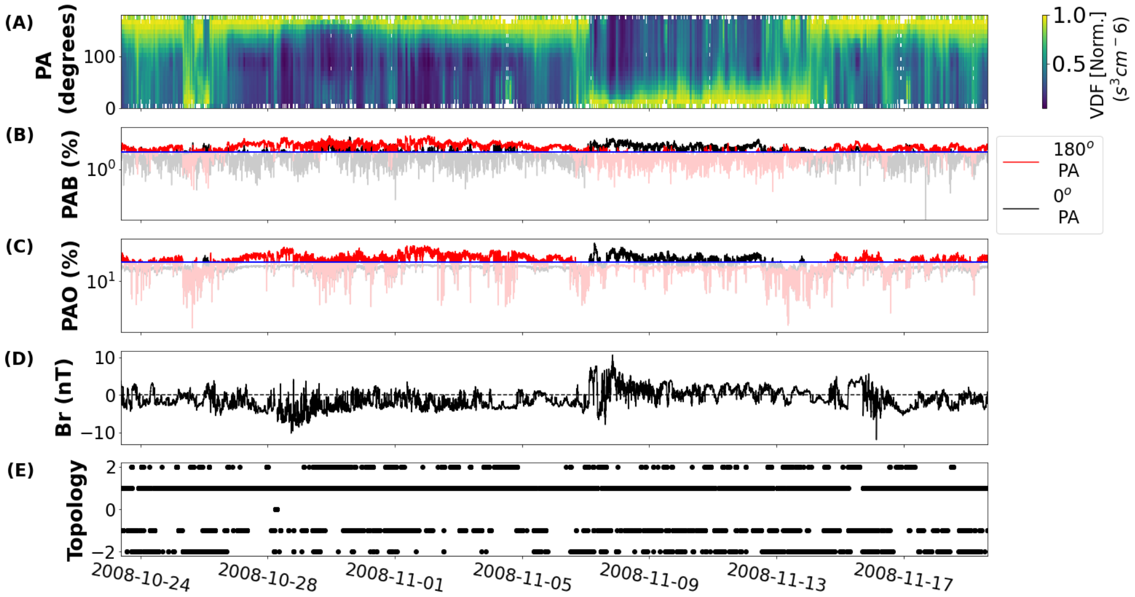

Figure 4.10: Adapted from Figure 4.6, a single CR of ACE observations from 23rd October to 19th November 2008. **A**) the suprathermal electron pitch angle distribution function ($f(v,\theta)$, units s^{3}cm^{-6}), normalized to the maximum and minimum flux at each time step. **B**) the PAB at 0^o PA (*black line*) and 180^o PA (*red line*), and the minimum PAB value of 45% (*blue line*). **C**) the PAO at 0^o PA (*black line*) and 180^o PA (*red line*), and the minimum PAO value of 140% (*blue line*). **D**) the radial magnetic field (nT) in GSE coordinates. **E**) topology indicator of the magnetic field indicating whether the flux is: open (*+1*), CS (*+2*), inverted (*-1*), unclassified/disconnected (*-2*). *0* indicates there is missing data.

Figure 4.10 also shows the application of these minimum constraints, using the same CR of ACE data as Figure 4.6. Panels B and C show the variation of PAB and PAO compared to the minimum constrained values plotted as the blue lines. Combining these PAB and PAO values with the sign of the radial magnetic field in panel D, gives the topologies. Panel E shows the topology indicator, which identifies each data point independently whether the flux is: open (*+1*), CS (*+2*), inverted (*-1*), unclassified/disconnected (*-2*). If there is any missing data this is indicated as *0*. In this CR, the available data consists of 65.4% open flux, 16.1% inverted flux, 7.7% CS flux, 10.8% unclassified/disconnected flux.

4.4.3 Effect of Strahl Criteria on OSF

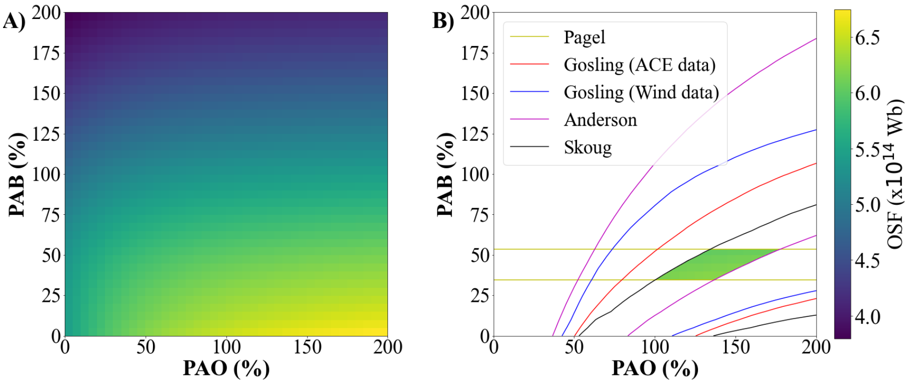

Figure 4.11: Selecting strahl identification criteria. (a) Average OSF over the interval 1994 to 2021 as a function of strahl identification criteria, PAO and PAB. (b) Values of PAO and PAB that are consistent with four previous studies: Gosling et al. (1992) (*red and blue lines* corresponding to ACE and *Wind*, respectively), Anderson et al. (2012) (*magenta line*), Skoug et al. (2000) (*black lines*) and Pagel, Crooker and Larson (2005) (*yellow horizontal lines*). The variation in OSF within the remaining PAO-PAB parameter space is very small.

In order to test the effect of these constraints, the OSF was computed using the method outlined in Section 5.2. Figure 4.11a shows the average OSF computed over the whole 1994 to 2021 interval for different PAO and PAB thresholds. Understanding the general variation is best approached by considering the limiting cases.

The top portion of Figure 4.11a shows high values of PAB, which means the criterion for strahl is more restrictive. This increases the occurrence of unclassified intervals, which are subtracted from Φ_R to compute OSF. Thus the lowest OSF estimates are produced in this region of parameter space. The bottom-left corner is low PAB and low PAO. Low PAB means that more strahl intervals will be identified at both 0 and 180-degree pitch angles. This reduces the unclassified (and hence disconnected) flux and increases OSF. However, the low PAO means that both strahl need to be nearly identical to be classed as CS (which would contribute to the OSF). Since the PAO condition is difficult to meet, this will result in fewer CS intervals, which will instead be classified as either uninverted or inverted HMF. As uninverted and CS HMF add to the OSF, and only inverted HMF and unclassified subtract, the possibility of increasing inverted HMF at the expense of CS can only serve to decrease the OSF. Moving to the bottom right of Figure 4.11a means increasing PAO. High PAO allows the strahl in opposite directions to be categorised as CS even when one strahl is up to double the flux of the other. This increases CS and reduces the occurrence of inverted HMF, increasing the OSF.

Thus the choice of PAB and PAO, even within fairly conservative limits, can vary the OSF by approximately 50 %. It is therefore vital to constrain both PAO and PAB thresholds if we wish to use strahl electrons to make an accurate correction for inverted flux to OSF estimates from *in-situ* observations of the HMF. We do that by reference to the results from four previously published observational studies.

4.5 Conclusions

Combining the field-aligned strahl and the radial magnetic field direction, it is possible to determine if a magnetic field line is directly connected to the Sun's surface. Using the sign of the radial magnetic field, we can determine if the field is directed toward or away from the Sun. The orientation of the strahl (either parallel or anti-parallel to the field) indicates whether the field is topologically open (where the magnetic field direction and strahl orientation are toward and anti-parallel, or away and parallel) or locally inverted (toward and parallel, or away and anti-parallel).

The orientation of the field-aligned strahl is determined by the constrained PAB and PAO described here. Using the results from four previous studies, the PAB and PAO values were constrained to a small window, the center of which we take the PAB and PAO values of 45 % and 140 % respectively. Within the presented region of acceptable PAB and PAO values, we have shown the effect on the topologies of the magnetic field, of which there is little variation. In addition, we have also reported that the OSF varies very little ($\pm 0.22 \times 10^{14}$ Wb or 3.5 %), suggesting that it is not a major source of uncertainty.

The topologies of the magnetic field determined from the method outlined in this chapter, from the complete 1994-2021 data set, will used in Chapter 5 for the calculation of the Open Solar Flux and in Chapter 6 for the superposed epoch analysis at true polarity reversals.

Chapter 5

Estimating the OSF from In-Situ Measurements

The OSF is the portion of the coronal field that maps into the heliosphere, magnetically connects the Sun to the planets, and dominates the motion of energetic particles. This OSF component can be determined via two methods: *in-situ* and magnetograms.

While the OSF determined from these methods should be the same, they actually differ by a factor of 2 or more. One possible cause for this disparity is the existence of local inversions (also known as switchbacks).

This chapter describes the OSF correction using the topologies from Chapter 4. The work presented in this chapter has been adapted in part from Frost et al. (2022), the goal of which was to correct the OSF for local field inversions and quantify the uncertainties associated with this.

The problem is introduced in Section 5.1, which reviews previous methods of determining the OSF. In Section 5.2 the method for calculating the OSF is outlined, which is adapted from the method used in Owens et al. (2017). In Section 5.3, the OSF is calculated from the combined ACE and *Wind* data set using the method outlined in Section 5.2. Error analysis is carried out to investigate the effect of data gaps on combining the two spacecraft, and a time average is found which gives a close approximation to the OSF with inversions removed presented here. In addition, the corrected OSF is compared to magnetogram OSF estimates to determine if the correction brings them closer to agreement. Finally, the main results are summarised in Section 5.4.

5.1 Introduction

The heliospheric magnetic field (HMF) is rooted in the Sun's photosphere and extends into the solar system, where it enables the Sun to interact with planetary magnetospheres. The HMF is the fraction of the magnetic flux that threads the solar photosphere and extends to a sufficient altitude that it is dragged out by the solar wind (e.g. Levine et al., 1977, Owens and Forsyth, 2013). Since the majority of the photospheric magnetic flux results in closed loops relatively near to the Sun - which do not contribute to the HMF - it is useful to define a "source surface" where the HMF begins. For convenience, this is typically defined as a fixed height above the photosphere (typically a few solar radii), though in reality will not be a fixed spherical surface (Schatten, 1968a,b), at which the coronal magnetic field becomes open to the heliosphere. Assuming such a source surface can be defined, the open solar flux (OSF) is then, by definition, the total unsigned magnetic flux that threads it (Wang and Sheeley, 1995).

As a consequence of $\nabla \cdot \mathbf{B} = 0$, the net magnetic flux through any closed surface is zero. Since fields always, eventually, form closed loops and there is no net source of magnetic flux, positive and negative flux cancel over any closed surface. Therefore, for a perfect Parker spiral (Parker, 1958) HMF, the unsigned magnetic flux threading the source surface equals that threading a sphere at 1 AU. What is observed, however, is that source surface OSF estimates derived from remote sensing observations are a factor of two or more lower than estimates derived from *in-situ* measurements at 1 AU (Linker et al., 2017, Wallace et al., 2019).

5.1.1 Methods of Estimating OSF

In order to understand the differences between OSF estimates from magnetograms and *in-situ* measurements, it is first important to understand how these estimates are obtained. Magnetograms are maps of the solar magnetic field at the photosphere (Beckers, 1968), derived from remote sensing observations. Until the very recent *Solar Orbiter* mission (Mueller et al., 2013), these observations were limited entirely to the Earth-facing side of the Sun and captured from the ecliptic plane, resulting in poor viewing geometry for the polar field. To obtain an estimate of OSF, photospheric magnetic field observations are collected over a complete solar rotation (approximately 27 days from Earth's point of view) to give full longitudinal coverage, assumptions are made about the polar fields, then the resulting photospheric magnetic field map is extrapolated to the top of the corona to estimate the OSF. This is typically achieved using a coronal magnetic field model, such as a potential field source surface (PFSS, Schatten et al., 1969) model. Similar to *in-situ* estimates, these photospheric models contain arbitrary choices that affect the OSF, most notably, the height of the source surface. Model-free estimates of OSF have also been derived from magnetograms by assuming all the OSF resides within coronal holes (e.g. Linker et al., 2017, Wallace et al., 2019), dark regions in extreme ultraviolet (EUV) and x-ray images (Cranmer, 2009). Using this assumption of all OSF residing in these regions, the source-surface height can be calibrated by matching OSF foot points with observed coronal hole area.

In-situ estimates are derived from spacecraft, by integrating point measurements of the radial magnetic field (B_r) over a sphere. Longitudinal coverage is obtained by integrating over a solar rotation. However, when estimating global OSF from point measurements, it is also necessary to assume a latitudinal invariance in the magnitude of B_r, which will be explained in more detail later in the section.

5.1.2 Previous studies

Linker et al. (2017) calculated MHD and PFSS solutions of the coronal magnetic field using 14 different magnetic maps produced from 5 different observatory magnetograms. Within PFSS models, the source surface height is a free parameter, so this can be raised to lower the OSF and the modelled coronal hole area. All models that met the observational constraint of coronal hole areas matching the open field regions were found to underestimate the HMF. Conversely, models that produced OSF in agreement with the *in-situ* estimate produced open field regions that were larger than coronal holes observed in EUV. This study concluded that either: observatory maps underestimate the Sun's magnetic flux, or a significant amount of OSF does not originate in regions that are dark in EUV.

Wallace et al. (2019) computed the OSF using two different remote methods, using full Sun magnetic maps extrapolated from magnetograms and EUV-derived coronal hole maps, and compared with results obtained from *in-situ* HMF observations. Both methods display deviations in OSF from *in-situ* spacecraft data, especially at solar maximum. This study concluded that coronal models capture the observed large-scale coronal hole structure over most of the solar cycle, but as a result, something other than coronal hole areas is the source of these discrepancies.

Smith and Balogh (1995) outlined the heliospheric flux estimate (HFE) of calculating the OSF from *in-situ* measurements. Using point measurements, the OSF can be calculated using a few key assumptions. Firstly, the variation in longitude is taken into account by averaging the radial magnetic field over 27 days (rotation of the Sun), expressed as $\langle |B_r| \rangle_{27day}$. Within this assumption, the time resolution at which you take the modulus can make a significant difference since this is something of a free parameter (Lockwood et al., 2009*b*). Secondly, that the Sun's magnetic field is assumed to be independent of latitude at the source surface and beyond. This is deemed to be valid as Ulysses measurements show that R^2B_r (the radial component of the HMF multiplied by the square of the radial distance) is independent of latitude (Smith and Balogh, 1995, 2003). Using these assumptions, the total heliospheric flux threading the heliocentric sphere at the radius of observation, R, can be calculated: $\Phi_r = 4\pi R^2 \langle |B_r| \rangle_{27day}$. This is the HFE. $4\pi R^2 |B_r|$ is the total unsigned open flux from the Sun, however, this can also be expressed as the signed open flux ($2\pi R^2 B_r$) such as in Lockwood et al. (1999). The final assumption is that the OSF calculated at the source surface is the same as this standard method, i.e. $\Phi_{SS} == \Phi_r$, which is true for an ideal Parker spiral, as previously mentioned.

Lockwood et al. (2009*b*,*c*) investigated the "flux excess" effect, where OSF estimates increase with heliocentric distance, indicating that the assumption $\Phi_{SS} == \Phi_r$ is not valid. This increase was reported to be consistent with the variation of OSF estimates highlighted by Owens et al. (2008). Owens et al. (2008) compared OSF estimates from multiple spacecraft, where spacecraft at smaller radii give lower OSF estimates than those at larger radii. Lockwood et al. (2009*b*,*c*) apply a "kinematic correction" to account for the effect of large-scale longitudinal structure of the solar wind flow. Applying this correction gives a result in close agreement to Owens et al. (2017).

Erdos and Balogh (2014) investigated the density of OSF over long periods at various locations in the heliosphere, using magnetometers onboard different spacecraft. With the aim to correct for the effect of fluctuations of the magnetic field, the magnetic field component perpendicular to the Parker field line was neglected. At all distances, the radial magnetic field was normalised to 1 AU, and the effects of fluctuations of the field (a result of the varying heliospheric distances) were reduced. This study showed a remarkably close agreement between flux densities measured from different latitudes, reiterating the conclusion that the magnetic flux is uniformly distributed in the heliosphere. No direct comparison with magnetogram-derived estimates were made, but the values obtained were significantly larger than those of Owens et al. (2017). It is also noteworthy that Erdos and Balogh (2014) had to make arbitrary decisions about time averaging for the radial magnetic field and they used 6-hour averages without strong justification.

Owens et al. (2017) investigated the effect of local magnetic field inversions on OSF estimates. Using a combination of electron and magnetic data, intervals where the magnetic field lines are locally bent or twisted were unambiguously identified. As these intervals are expected to result in overestimates of OSF, inversions were removed from the OSF calculation. More details will follow in the next section.

Finally, Badman et al. (2021) investigated OSF in the inner heliosphere using data from the Parker Solar Probe. At these locations too, the observed OSF value was found to be significantly higher than implied by PFSS models. This study concluded that this difference in OSF is most likely to be found in new modeling techniques or by our improved knowledge of the photospheric field.

5.2 Method

5.2.1 Topology of the Field

As explained in Chapter 4, the combined radial magnetic field and suprathermal electron *in-situ* observations were used to determine whether the topology of the magnetic field was open, closed, locally inverted, or disconnected. To summarise: To be categorised as open, the positive/negative radial magnetic field needs to be accompanied by a parallel/anti-parallel Strahl signature. For a closed field, the direction of consecutive magnetic field measurement will change and the Strahl signature needs to be visible in both directions. To identify inverted flux, the radial magnetic field would be positive/negative with an anti-parallel/parallel Strahl signature, which is the opposite of the open flux. Finally, disconnected flux can be identified by the lack of a Strahl signature.

5.2.2 Open Solar Flux

Using the topologies calculated in Chapter 4, we can calculate the OSF from the combined 128s *in-situ* data set, using the method outlined by Owens et al. (2017), though with modifications detailed here.

First, we compute the total unsigned magnetic flux threading the sphere at the radius of observation (approximately $R = 1AU$):

$$\phi_r = 4\pi R^2 \langle |B_r| \rangle_{27days} \tag{5.1}$$

where the averaging interval indicated by the angled brackets is one solar synodic rotation period ($\approx$ 27.27 days for spacecraft in near-Earth space), in order to average over all solar longitudes. However, there is a question of the time resolution at which $|B_r|$ is computed, which adds a level of complication to this, see Section 1.2. Computing $|B_r|$ on 1-day resolution data can reduce ϕ_r by around 30% compared with using 64-second data. This choice of averaging interval is obviously somewhat arbitrary since there is no clear choice of time averaging that will necessarily select out the true OSF component of ϕ_r and, as shown later in Section 5.3.4, this may be expected to vary with the solar cycle in a complex manner.

Instead, the approach outlined by Owens et al. (2017) is to use the highest resolution data available to compute ϕ_r. The difference between 1 or 2 minutes (as used in this study) and 1-second data is very small ($\sim 1\%$) compared with the difference between 1-minute and 1-day data ($\sim$ 30%) (e.g., Figure 2 in Lockwood et al., 2009*a*). Intervals that do not contribute to OSF are then individually identified and subtracted from ϕ_r.

STE (suprathermal electron) data is used to identify inverted HMF intervals that have no direct connection to the Sun. Within a given Carrington rotation, the total magnetic flux contained within inverted HMF is designated ϕ_C and subtracted from ϕ_r. In fact, 2 ϕ_C is removed to include the magnetic flux from sunward Strahl intervals and the (unidentifiable) return HMF topology:

$$\phi_{OSF} = \phi_r - 2\phi_C. \tag{5.2}$$

For each Carrington rotation, the average $|B_r|$ for anti-sunward Strahl (uninverted

HMF), sunward Strahl (inverted HMF), closed, unclassified and all HMF types, referred to as $\langle|B_r|\rangle_{AS}$, $\langle|B_r|\rangle_{SS}$, $\langle|B_r|\rangle_{CL}$, $\langle|B_r|\rangle_{U}$, and $\langle|B_r|\rangle_{ALL}$, respectively, as well as the number of 128s intervals of each type, N_{AS}, N_{SS}, N_{CL}, N_U, and N_{ALL} are determined. From this, Equation 5.1 can be written as:

$$\phi_r = \frac{4\pi R^2}{N_{ALL}}[N_{AS}\langle|B_r|\rangle_{AS} + N_{SS}\langle|B_r|\rangle_{SS} + N_{CL}\langle|B_r|\rangle_{CL} + N_U\langle|B_r|\rangle_U], \tag{5.3}$$

where $N_{ALL} = N_{AS} + N_{SS} + N_{CL} + N_U$.

As displayed in Figure 4.3, disconnected flux (topology e) is identified due to an absence of a Strahl signature. Therefore, any flux that we determine to be unclassified is assumed to be disconnected, so will not contribute to the OSF. Equation 5.3 then becomes:

$$\phi_r = \frac{4\pi R^2}{N_{ALL}}[N_{AS}\langle|B_r|\rangle_{AS} + N_{SS}\langle|B_r|\rangle_{SS} + N_{CL}\langle|B_r|\rangle_{CL}]. \tag{5.4}$$

Finally, the sunward strahl component, ϕ_C, is defined as:

$$\phi_C = \frac{4\pi R^2}{N_{ALL}}[N_{SS}\langle|B_r|\rangle_{SS}]. \tag{5.5}$$

5.3 Results and Discussion

5.3.1 Open Solar Flux

Using the method outlined in Section 5.2.2, the OSF can be corrected for locally inverted flux. Figure 5.1 shows CR averages of the OSF for the combined ACE and *Wind* data from 1994 - 2021. The OSF calculated using Equation 5.1 is shown by the red line and the OSF calculated using Equation 5.2 is shown by the black line. With the removal of inverted flux, the OSF calculated here (Equation 5.2) is consistently lower.

In addition to removing the inverted flux, an assumption has been made that the

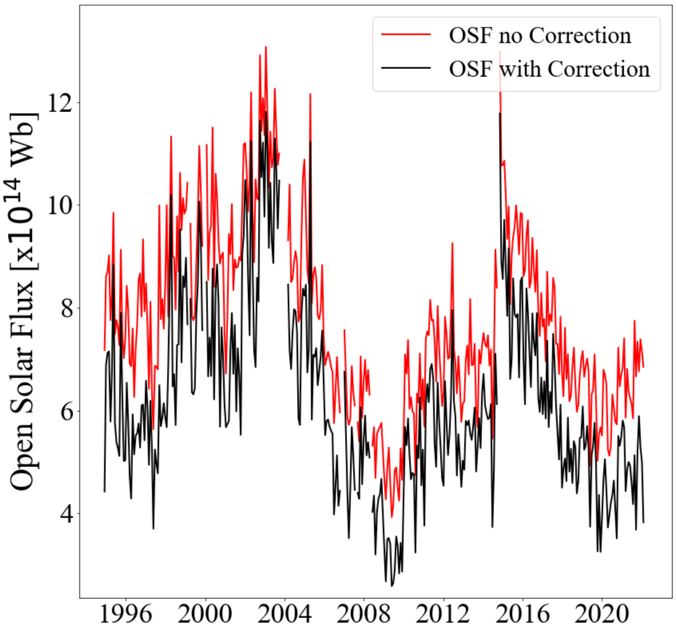

Figure 5.1: Time series of OSF estimates over the period of study. The *red line* shows the OSF calculated using Equation 5.1, which does not include the correction for inverted flux. The *black line* shows the OSF calculated using Equation 5.2, which includes the correction for inverted flux.

unclassified flux is disconnected flux. This is shown by Figure 5.2, where the red line is the OSF calculated by:

$$\phi_r = \frac{4\pi R^2}{N_{ALL}}[N_{AS}\langle|B_r|\rangle_{AS}+N_{CL}\langle|B_r|\rangle_{CL}+N_U\langle|B_r|\rangle_U-N_{SS}\langle|B_r|\rangle_{SS}-\frac{N_{SS}}{N_{ALL}}N_U\langle|B_r|\rangle_U], \tag{5.6}$$

which assumes that the same proportion, as the whole data set, of all other topologies makes up the unclassified flux. The black line shows the OSF calculated using Equation 5.2. This figure shows the effect on the OSF over the entire period of study when the unclassified flux is assumed to contain the same proportions of open/inverted/counterstreaming flux (red line), compared to the unclassified flux being a proxy for disconnected flux (black line). Assuming the unclassified flux is disconnected flux leads to a decrease in the OSF.

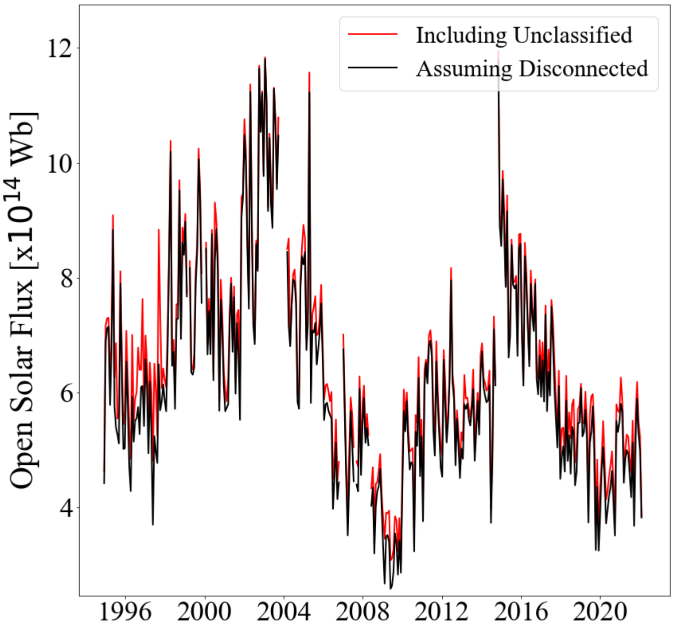

Figure 5.2: Time series of OSF estimates over the period of study. The *red line* shows the OSF calculated using Equation 5.6, which assumes that the same proportion of all other topologies makes up the unclassified flux. The *black line* shows the OSF calculated using Equation 5.2, which assumes the unclassified flux is a proxy for disconnected flux.

5.3.2 Data Gaps

In this section, we aim to assess whether differences between ACE and *Wind* estimates of OSF can be attributed to the data gaps in one or other data set and to quantify the expected OSF uncertainty for a given level of data coverage. Two approaches are taken. Firstly, we compute the "actual error", shown by the bottom panel of Figure 5.3, which is the difference between ACE and *Wind* OSF estimates for the same Carrington rotation, as shown by the top panel of Figure 5.3. This error incorporates the effect of any data gaps, as well as differences in the pitch-angle bins used to define Strahl, the small differences in spacecraft position, and instrumental differences. Given the data availability for the period of overlap, we compute the error in the *Wind* OSF estimate for CRs where there is more than 95 % of data available for ACE.

Figure 5.4a shows the actual errors as black crosses. As expected, there is a general trend for larger errors when there is less data available. This is seen more clearly in the binned data in Figure 5.4b, where the mean actual errors are binned in 5 % intervals

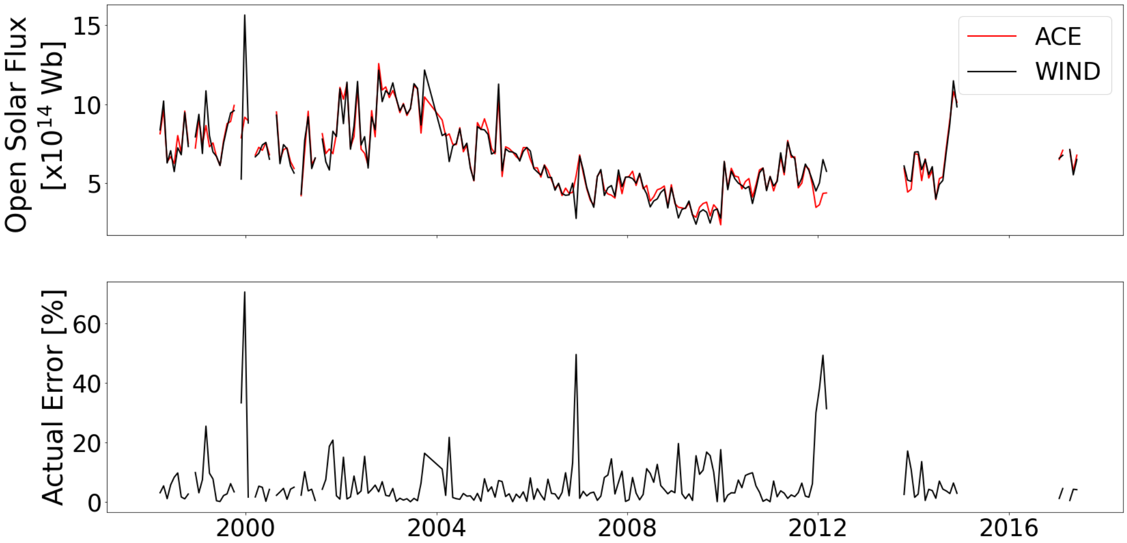

Figure 5.3: Time series of OSF estimates and the “actual error” over the period of study. The top panel shows the OSF calculated using Equation 5.2 using data from ACE (*red line*) and *Wind* (*black line*) for CRs where ACE has more than 95 % of data available. The bottom panel shows the “actual error” for each CR from the top panel.

and a best-fit polynomial is plotted. The flattening of this polynomial highlights the systematic difference between the spacecraft, with ACE producing a higher OSF than *Wind*. In Figure 5.4a, there are noticeable outliers in the actual errors between 80 and 100 % data coverage, highlighted by the red boxes.

Figures 5.5, 5.6, and 5.7 show the CR of data from the points highlighted in Figure 5.4a. In each of these plots: Ai) the suprathermal PA electron data from ACE, Aii) the radial magnetic field from ACE, Bi) the suprathermal PA electron data from *Wind*, Bii) the radial magnetic field from *Wind*, and C) the topology of the field. Aside from the effect of data gaps, the difference between the OSF estimates from ACE and *Wind* can be attributed to spacecraft differences.

In each of these examples, Figures 5.5, 5.6, and 5.7, the strahl direction and the radial field direction visually appear predominantly the same. However the difference between the OSF from each spacecraft is higher than expected from the datagaps alone. Therefore, the conclusion could be drawn that the variation can be attributed to spacecraft differences.

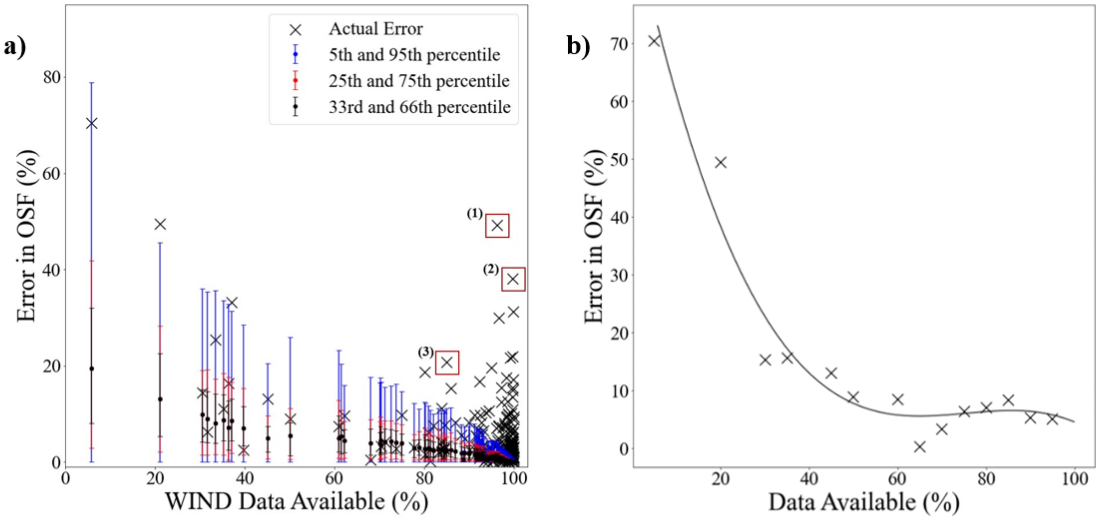

Figure 5.4: The effect of data gaps on OSF estimate. (a) The percentage error in OSF with changing data availability. The "actual errors" (*black crosses*), are given by direct comparison of simultaneous ACE and *Wind* data. Ranges for the 5th/95th (*blue*), 25th/75th (*red*), and 33rd/66th (*black*) percentiles of "predicted errors" are obtained by applying *Wind* data gaps for a given Carrington rotation to the whole 27-year dataset. (b) "Actual errors" binned in 5 % intervals of data availability (*black crosses*) with a best-fit polynomial (black line). Three *red boxes* highlight points for further study.

To investigate the effect of datagaps, we also compute a "predicted error" based purely on the data coverage (rather than also including spacecraft differences) by introducing synthetic data gaps. This is achieved in the following manner. For each CR of *Wind* data, the distribution of data gaps in time is found. In each instance, this data gap "mask" is applied to every CR within the ACE data set where there is more than 95 % data availability. Figure 5.8 shows an example of the application of data gaps. Panel A shows 3 CRs of ACE data with more than 95 % data available, Panel B shows a CR of *Wind* data with data gaps, and Panel C shows the same 3 CRs of ACE data with the same data gaps applied to all 3 CRs. The change in OSF from the complete ACE estimate as a result of the data gap mask is recorded, giving a distribution of OSF errors for each CR. This predicted OSF error distribution is shown in Figure 5.4a in terms of percentiles. Again, there is a general trend for both the mean and the width of the predicted error distribution to decrease with data coverage. However, there are

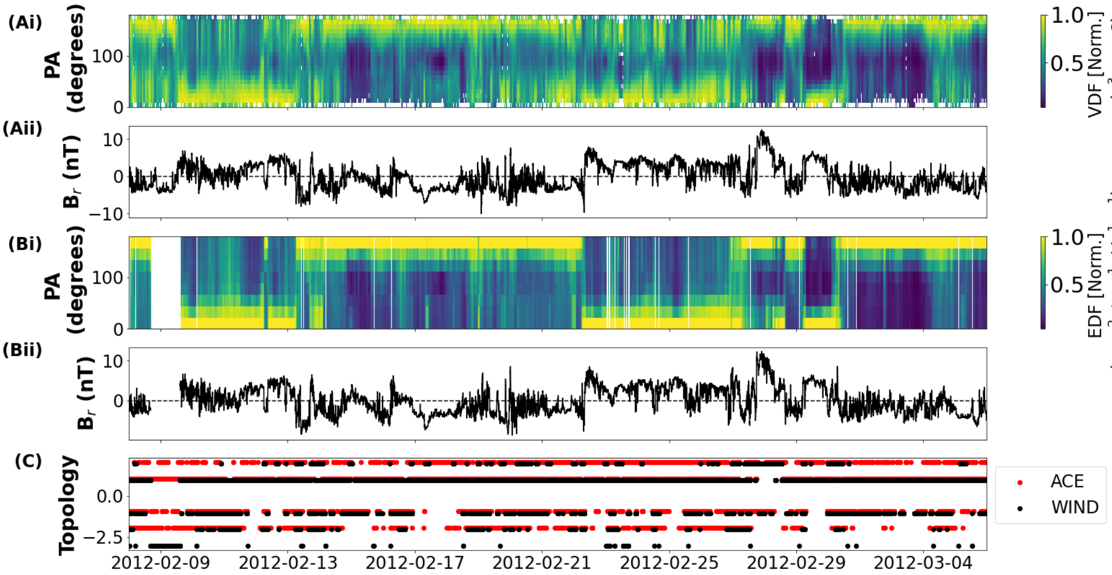

Figure 5.5: The CR of data corresponding to highlighted point 1 in Figure 5.4a. **Ai**) from ACE, the suprathermal electron pitch angle distribution function ($f(v, \theta)$, units $\mathrm{s}^3\mathrm{cm}^{-6}$), normalized to the maximum and minimum flux at each time step. **Aii**) from ACE, the radial magnetic field (nT) in GSE coordinates. **Bi**) from *Wind*, the suprathermal electron differential flux (EDF), units $\mathrm{cm}^{-2}\mathrm{ster}^{-1}\mathrm{eV}^{-1}\mathrm{s}^{-1}$), normalized to the maximum and minimum flux at each time step. **Aii**) from *Wind*, the radial magnetic field (nT) in GSE coordinates. **C**) combined (ACE in *red* and *Wind* in *black*) topology indicator of the magnetic field indicating whether the flux is: open (*+1*), CS (*+2*), inverted (*-1*), unclassified/disconnected (*-2*). *-3* indicates there is missing data.

clear exceptions to this, which are the result of different-sized data gaps (e.g., one big data gap versus lots of small data gaps). By inspection, we confirm that CRs with large contiguous data gaps resulting in larger errors than CRs with smaller frequent data gaps resulted in much smaller errors, even when the total data coverage is comparable. An example of this is shown by the error bars highlighted in Figure 5.9. With nearly identical data availability, the first error bar is over three times the size of the second error bar. The suprathermal electron differential flux (EDF) from *Wind*, see Figure 5.10, shows the CR of data used as the "mask" for each error bar. Panel A has a larger data gap which corresponds to the larger error in OSF, whereas panel B has smaller scattered data gaps which results in a much smaller error in OSF. This disparity in data gap sizes also affects the "actual" errors, especially at higher percentages of available *Wind* data, where many of the actual errors are higher than the predicted error range. In addition,

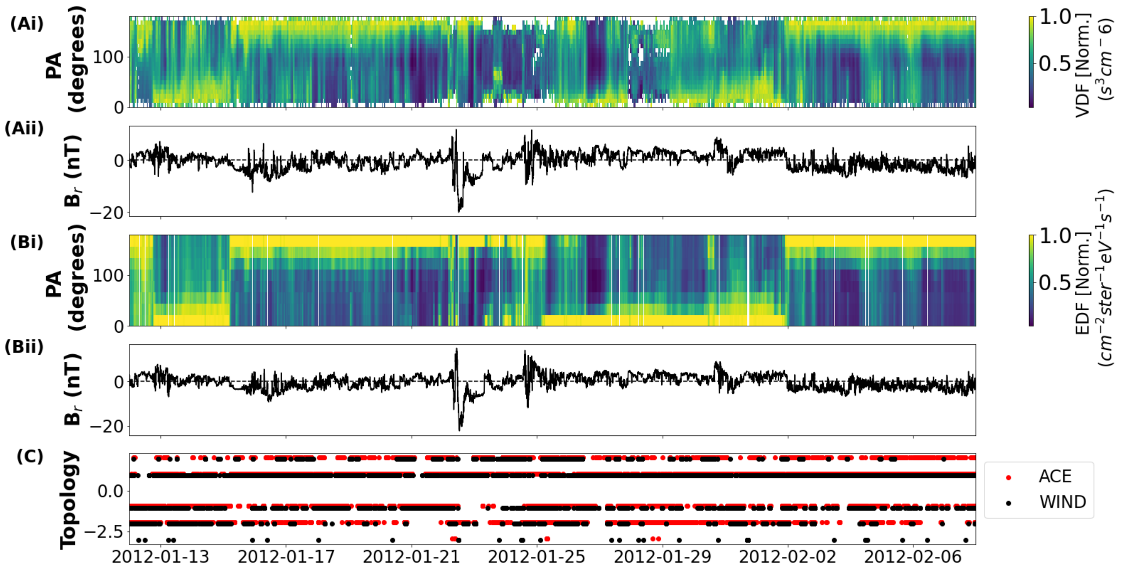

Figure 5.6: The CR of data corresponding to highlighted point 2 in Figure 5.4a. **Ai**) from ACE, the suprathermal electron pitch angle distribution function ($f(v, \theta)$, units s^3cm^{-6}), normalized to the maximum and minimum flux at each time step. **Aii**) from ACE, the radial magnetic field (nT) in GSE coordinates. **Bi**) from *Wind*, the suprathermal electron differential flux (EDF), units $cm^{-2}ster^{-1}eV^{-1}s^{-1}$), normalized to the maximum and minimum flux at each time step. **Aii**) from *Wind*, the radial magnetic field (nT) in GSE coordinates. **C**) combined (ACE in *red* and *Wind* in *black*) topology indicator of the magnetic field indicating whether the flux is: open (*+1*), CS (*+2*), inverted (*-1*), unclassified/disconnected (*-2*). *-3* indicates there is missing data.

the "predicted" errors, which only account for data gaps, are systematically lower than the actual error, which suggests there are small spacecraft-specific differences too.

In order to quantify uncertainty in the final OSF estimate, we fit the binned "actual error" data, shown in Figure 5.4b, with a third-order polynomial:

$$y = -0.0002135x^3 + 0.04825x^2 - 3.566x + 92.17, \tag{5.7}$$

where y is the percentage error in OSF and x is the percentage of data available. This captures the general trend in the data, which is all we seek to do, of a fairly constant error for data availability above 50 %.

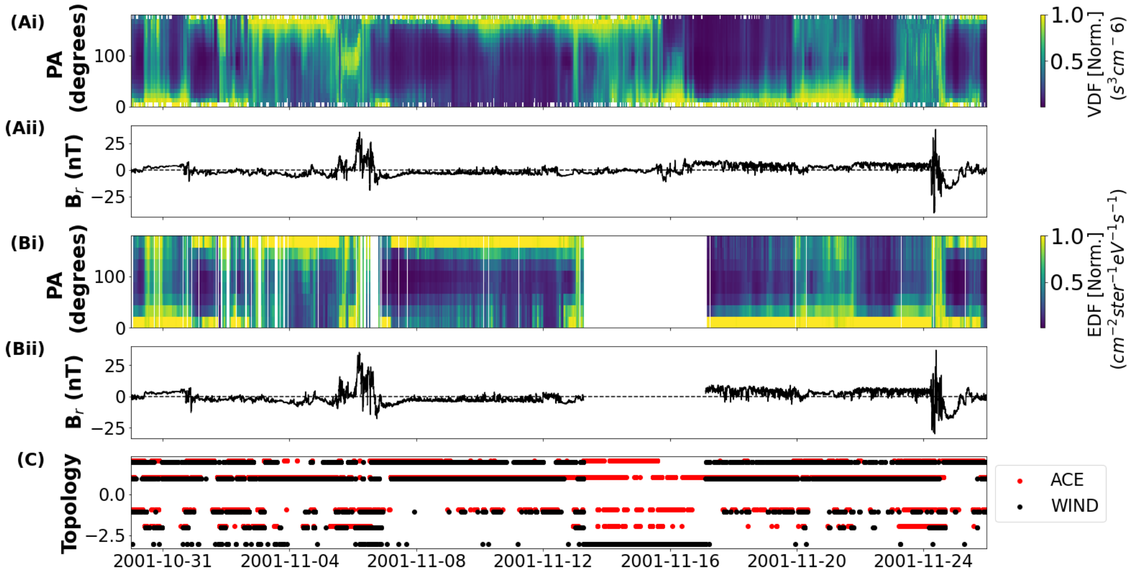

Figure 5.7: The CR of data corresponding to highlighted point 3 in Figure 5.4a. **Ai**) from ACE, the suprathermal electron pitch angle distribution function ($f(v, \theta)$, units s^3cm^{-6}), normalized to the maximum and minimum flux at each time step. **Aii**) from ACE, the radial magnetic field (nT) in GSE coordinates. **Bi**) from *Wind*, the suprathermal electron differential flux (EDF), units $cm^{-2}ster^{-1}eV^{-1}s^{-1}$), normalized to the maximum and minimum flux at each time step. **Aii**) from *Wind*, the radial magnetic field (nT) in GSE coordinates. **C**) combined (ACE in *red* and *Wind* in *black*) topology indicator of the magnetic field indicating whether the flux is: open (*+1*), CS (*+2*), inverted (*-1*), unclassified/disconnected (*-2*). *-3* indicates there is missing data.

5.3.3 OSF Best Estimate

We now combine the ACE and *Wind* data sets to produce a best estimate of OSF over the period of 1994-2021, corresponding to the majority of the length of the *Wind* mission, which is still ongoing. During the period of overlap, for each CR we select the spacecraft with the greatest data coverage, using a minimum data availability of 50 %. Where data coverage is equal, we take an average of the *Wind* and ACE estimates. Figure 5.11a shows the individual spacecraft estimates of OSF and the resulting best estimate. In general, the OSF estimates from the two spacecraft are in very close agreement, but there are two intervals of note. During the early period of overlap, around 1998-2002, *Wind* had poorer HMF coverage owing to its excursions into the magnetosphere, and the best estimate is largely the ACE value. Conversely, a significant

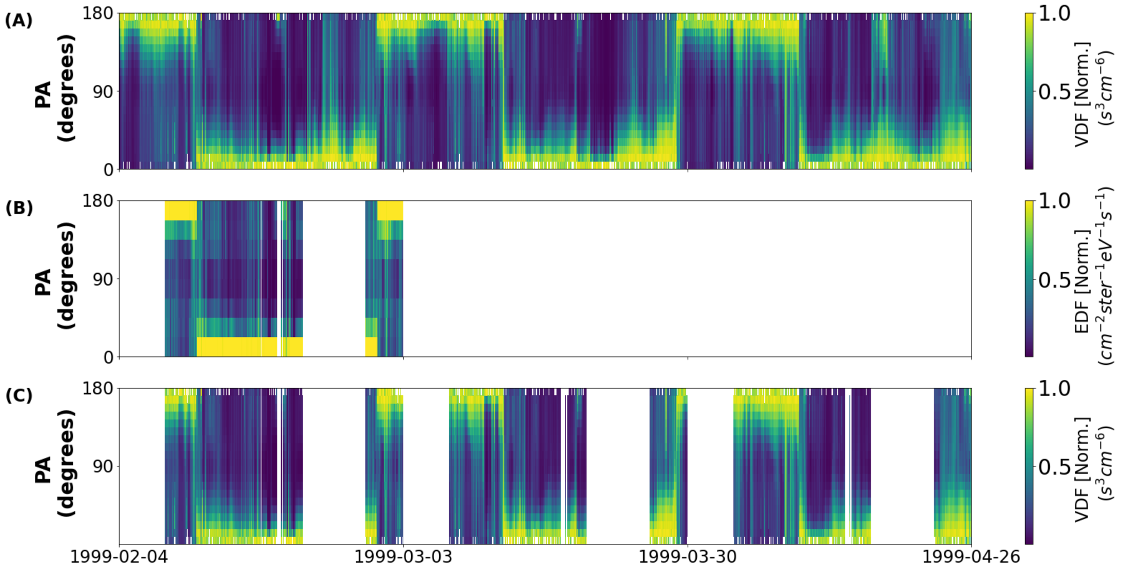

Figure 5.8: An example of the application of data gaps from *Wind* to ACE CRs where there is more than 95 % data availability. **A**) 3 CRs of ACE data, showing the suprathermal electron pitch angle distribution function ($f(v, \theta)$, units s^{3}cm^{-6}), normalized to the maximum and minimum flux at each time step. **B**) single CR of *Wind* data with data gaps, showing the suprathermal electron differential flux (EDF), units cm^{-2}ster^{-1}eV^{-1}s^{-1}), normalized to the maximum and minimum flux at each time step. **C**) same 3 CRs of ACE data from **A** with the data gaps from **B** applied to each CR of data.

proportion of ACE data was missing during 2012-2014, and the coverage remains around 80 % after this period, so the *Wind* estimate is preferable from 2012 onward. Figure 5.11b displays the OSF best estimate with corresponding percentage errors extrapolated from Figure 5.4b.

With the implementation of the method outlined above, the full 1994-2021 best-estimate data consisted of 14.97 % inverted flux by occurrence. Of the remainder, 65.47 % was open flux, 11.29 % newly-opened flux (i.e., counterstreaming) and 8.27 % unclassified flux. Compared to Owens et al. (2017) (17.04 % inverted flux, 68.65 % open flux, 4.18 % newly-opened flux, and 10.13 % unclassified), the values reported here agree well, aside from the higher newly-opened flux which is likely the result of the different conditions we used. Another key difference is the assumption we made about the unclassified flux being a proxy for disconnected flux. Despite the different topologies, the OSF calculated here agrees well and is slightly higher than the Owens

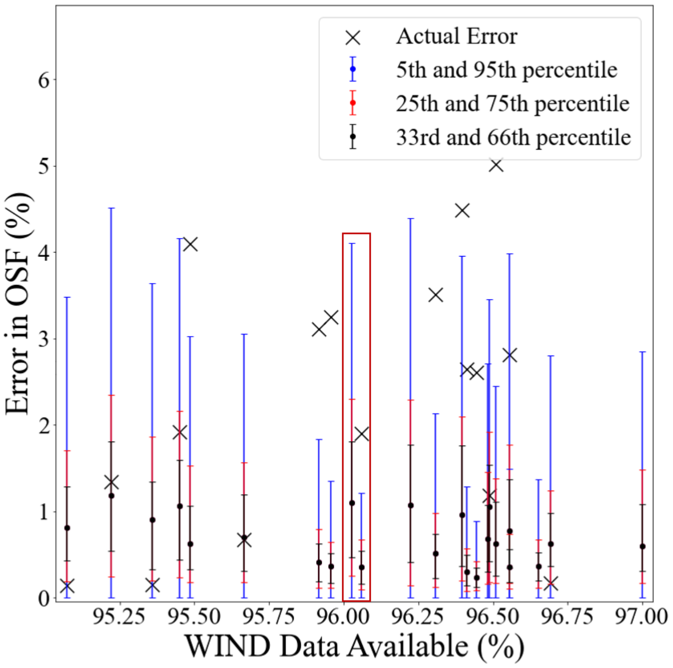

Figure 5.9: As in Figure 5.4a, the percentage error in OSF with changing data availability. The "actual errors" (*black crosses*), are given by direct comparison of simultaneous ACE and *Wind* data. Ranges for the 5th/95th (*blue*), 25th/75th (*red*), and 33rd/66th (*black*) percentiles of "predicted errors" are obtained by applying *Wind* datagaps for a given Carrington rotation to the whole 27-year data set. A more specific portion of Figure 5.4a is shown, with two error bars highlighted for further study.

et al. (2017) result, see Figure 5.14 later. The average OSF from Owens et al. (2017) is $6.45^{+0.28}_{-1.21} \times 10^{14}\mathrm{Wb}$ and our method, for the same period, gave an average OSF of $6.59 \pm 0.35 \times 10^{14}\mathrm{Wb}$. Thus there is agreement within the estimated uncertainty. The results outlined here also generally agree with Badman et al. (2021), which reports an occurrence of 25 % inverted flux, compared to our best estimate of 15 % inverted flux for the same time period. Since PSP data is at a much higher resolution than the combined ACE/*Wind* data set, PSP likely detects rapid inversions that are missing from our data set, which results in a higher percentage from Badman et al. (2021).

5.3.4 Time-averaging Approximation

Previous studies (Wang and Sheeley, 1995, Wallace et al., 2019, Wang et al., 2022) have used 1-day averages of B_r to estimate OSF from *in-situ* data. Owens et al.

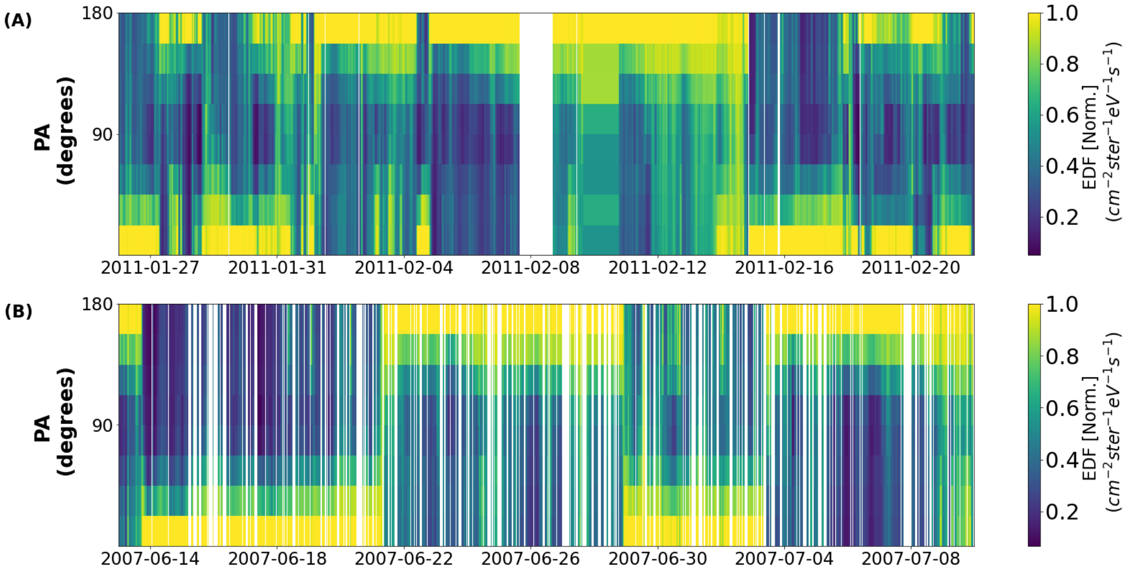

Figure 5.10: The CRs of *Wind* data corresponding to highlighted error bars in Figure 5.9. Both panels show a single CR of *Wind* data with different sized data gaps, showing the suprathermal electron differential flux (EDF), units cm^{-2}ster^{-1}eV^{-1}s^{-1}), normalized to the maximum and minimum flux at each time step. **A**) CR of data corresponding to the first, larger error bar in Figure 5.9. **B**) CR of data corresponding to the second, smaller error bar in Figure 5.9.

(2017) showed that this approximates the more complex strahl method, at least on average. Figure 5.12 shows the best estimate of OSF from the strahl method compared to Equation 5.1, $\Phi_R = 4\pi R^2 \langle |B_r| \rangle$. The shaded regions show Φ_R calculated using B_r computed from different averaging interval durations. From lightest to darkest, Φ_R was computed with averaging intervals of: 1 hour, 10 hours, 18 hours, 20 hours, 24 hours, and 48 hours. From these estimates, the 20-hour B_r averages give the closest agreement to the best-estimate from the Strahl method, shown in Figure 5.12 as the red line, with an average difference of 0.72 %. The OSF calculated by Owens et al. (2017) are able to be approximated by 35-hour averaged data. This 35-hour averaging gives an OSF estimate of 7.29 % higher than the results reported here.

Figure 5.13 shows scatter plots of the best time-averaging approach (i.e., Φ_R computed from 20-hour averages of B_r) compared to the best OSF estimate from the strahl method, computed over 1 year (panel a) and 27 day (panel b) intervals. Panels (c) and (d) show the histograms of the percentage difference between the two methods. At

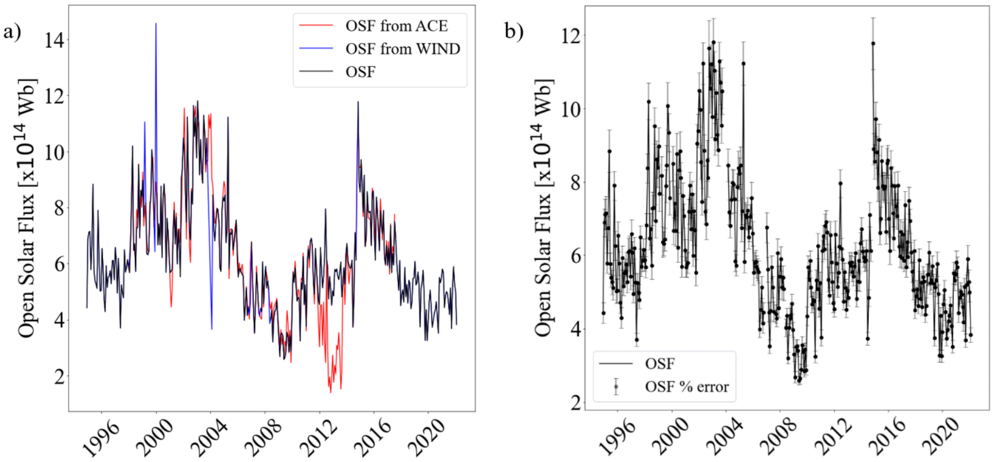

Figure 5.11: Time series of OSF estimates over the period of study. (a) The individual ACE (*red line*) and *Wind* (*blue line*) OSF estimates. The *black line* shows the best estimate derived from taking the highest data coverage on a CR by CR basis (b) The best estimate of OSF (*black line*) with error bars computed from the available data coverage.

both the annual and 27-day resolution, there is clearly a strong correlation between OSF computed by both methods. At annual time scales, there is comparatively low scatter ($\pm 12.2\,\%$), which demonstrates the ability of the standard method to accurately represent the true OSF at annual timescales, if the estimates are constructed from 20-hour averages of $|B_r|$. Panel (b) shows that there is a much larger spread at the 27-day resolution ($\pm 56.3\,\%$), which demonstrates the difficulty in representing the corrected OSF on CR timescales without using the strahl method.

Using 20-hour averages of B_r, Φ_R can be corrected to more closely match the Strahl method using the best fits from Figures 5.13a and b. In order to correct yearly OSF values, the correction is:

$$\mathrm{OSF}_{\mathrm{corrected}} = 1.04\,\mathrm{OSF}_{20-\mathrm{hour}} - 0.28. \tag{5.8}$$

To correct CR OSF values, the correction is:

$$\mathrm{OSF}_{\mathrm{corrected}} = 0.94\,\mathrm{OSF}_{20-\mathrm{hour}} - 0.36. \tag{5.9}$$

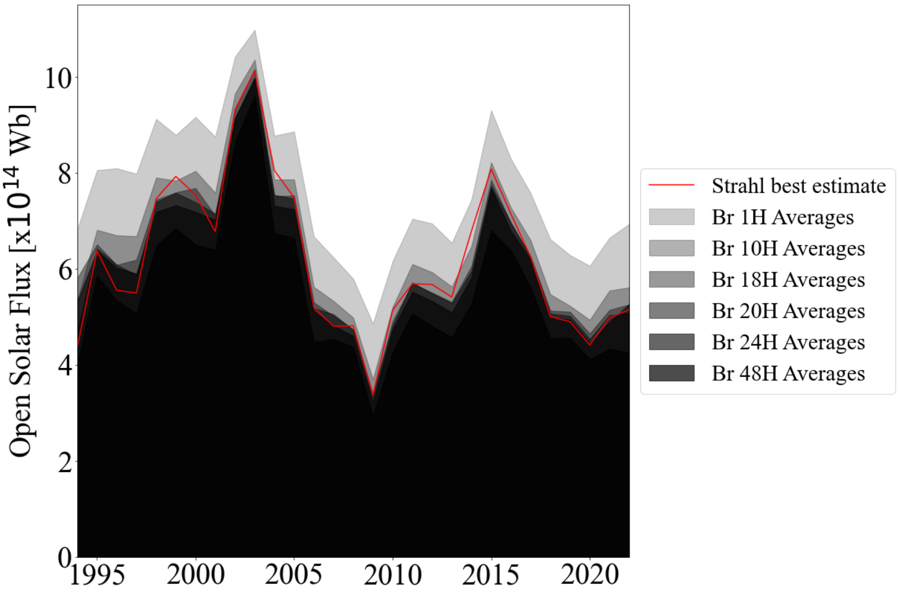

Figure 5.12: OSF yearly time series from different time averages of B_r used in the standard OSF calculation (i.e., $\Phi_R = 4\pi R^2\langle|B_r|\rangle$). The *shaded regions* display the different time averages of $|B_r|$ between 1-100 hours. The *red line* shows the best estimate of OSF calculated from the Strahl method. A 20-hour time average of B_r provides the closest agreement.

These equations correct for the tendency for the time-averaging method to overestimate the OSF at low values (and hence solar minimum), and underestimate OSF at high values (and hence solar maximum).

5.3.5 In-situ and magnetogram OSF comparisons

Figure 5.14 shows the best *in-situ* estimate of OSF compared with the OSF estimates derived from magnetograms (Wallace et al., 2019). These are either potential field source surface (PFSS) estimates, or observational coronal hole identification methods applied to magnetograms. The solid black line is the best estimate of OSF using the Strahl method, as detailed in Section 5.3.3. In general, and echoing the result of Owens et al. (2017), our estimate gives lower OSF than simply computing $\Phi_{R=1\mathrm{AU}}$, bringing the *in-situ* estimate of OSF into a closer agreement with the photospheric magnetic field-based OSF estimates, as highlighted by Figure 5.14. On average, the discrepancy for the period of overlap between our best estimate and WSA (1994-2013) is now a factor 1.6 compared to a factor 2 or higher for $\Phi_{R=1AU}$ computed from 1-hour magnetic field data.

5.4 Conclusions

This study has aimed to improve upon the method outlined in Owens et al. (2017) for estimating open solar flux (OSF) from *in-situ* spacecraft observations and to extend the period of study from 13 to 27 years. We have investigated the robustness of the method and the choice of free parameters which can affect the resulting OSF estimate. The "best estimate" OSF values found here are slightly higher than the Owens et al. (2017) estimates. As stated in Section 4.3, the average OSF from Owens et al. (2017) is $6.45 \pm 1.21 \times 10^{14}\mathrm{Wb}$ for the period 1998-2011, and the average OSF from the Strahl method used here is $6.59 \pm 0.35 \times 10^{14}\mathrm{Wb}$, which agree within the uncertainties. However, a large discrepancy remains between the *in-situ* and magnetogram OSF estimates, indicating that factors in addition to inverted flux must contribute also. These are likely to be either problems with measuring the photospheric magnetic field (Riley et al., 2019, Wang et al., 2022) or methods of determining OSF from the magnetograms, such as assuming all OSF is in observable coronal holes. Indeed, outflows mapping to active regions suggests this may not be accurate (e.g. van Driel-Gesztelyi et al., 2012).

A major outstanding assumption that remains in the OSF estimates from *in-situ* data is that the measurements made at one latitude are representative of all latitudes. $R^2|B_r|$ is expected to be constant with latitude due to the equalisation of tangential magnetic pressure. This is expected to occur relatively close to the Sun, inside the Alfvén point, within $\approx 10R_\odot$ (Suess et al., 1996, Suess and Smith, 1996, Suess et al., 1998). While a latitudinal invariance in $R^2|B_r|$ has been observed in the heliosphere (Smith and Balogh, 1995), the uncertainty introduced to OSF estimates is nevertheless difficult to directly quantify. In particular, HMF inversions have been observed close to the Sun (Badman et al., 2021) and tend to increase in occurrence with R (Macneil et al., 2020), but maybe not equally at all latitudes (Lockwood and Owens, 2009). If inversions are being created in the heliosphere and preferentially in the slow solar wind (Owens et al., 2013), then $R^2|B_r|$ may vary inside/outside the streamer belt. While $R^2|B_r|$ may be different at the equator and poles, the actual OSF per unit latitude should be fixed at the near-Sun value (as it cannot easily equilibrate in the supersonic solar wind). However, this merits further investigation.

The Strahl-based estimate of OSF presented in this study can be approximated by the use of 20-hour averages of B_r in the standard total heliospheric flux calculation $4\pi R^2|B_r|$. This is useful for studies interested in longer-term variations, however, this is not suitable for CR variations. The time-averaging approximation is likely to slightly underestimate the solar cycle variation in OSF, by overestimating OSF during solar minimum and underestimating during solar maximum.

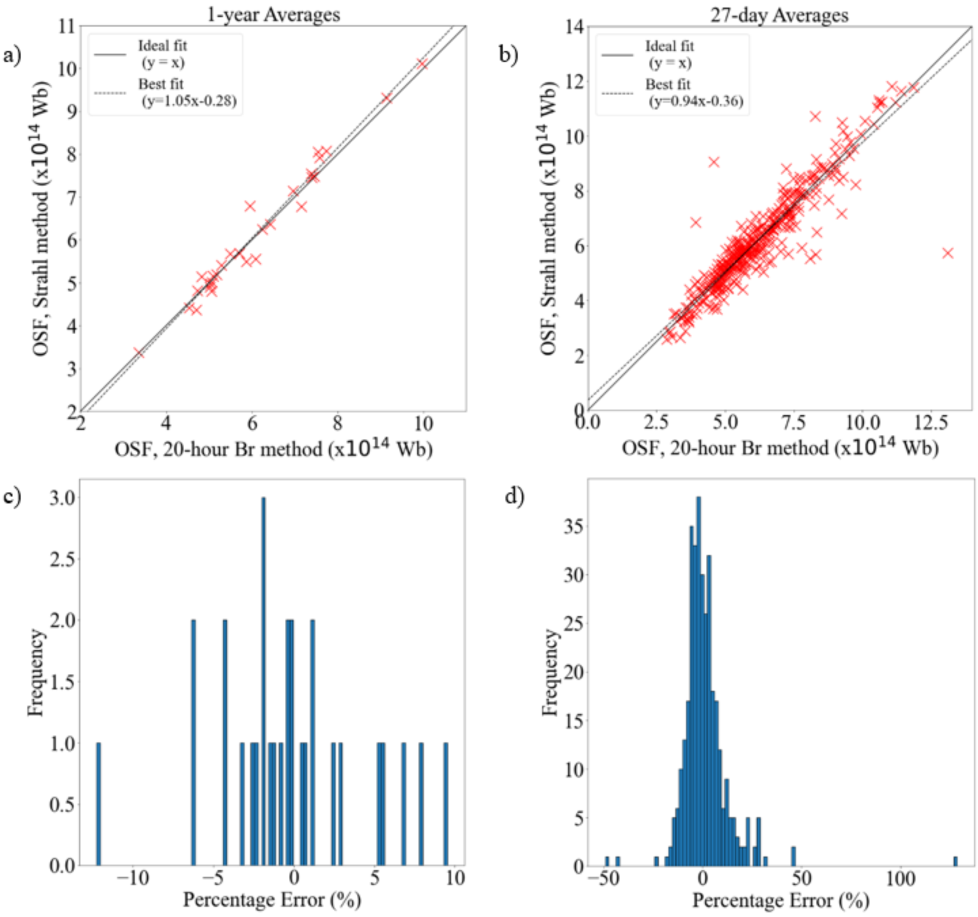

Figure 5.13: Comparisons of OSF calculated via the standard method ($\Phi_R = 4\pi R^2\langle|B_r|\rangle$) computed using 20-hour averages of $|B_r|$ with the best estimate from the Strahl method. (a) A scatter plot of yearly averages. The *solid black line* shows $y = x$, and the *dashed black line* is a linear best fit. (b) A scatter plot of CR averages. (c) A histogram of the percentage errors between the Strahl method and Φ_R computed with 20-hour averaged data for yearly intervals, where a positive error signifies an overestimation. (d) The same as *panel c*, but for CR intervals.

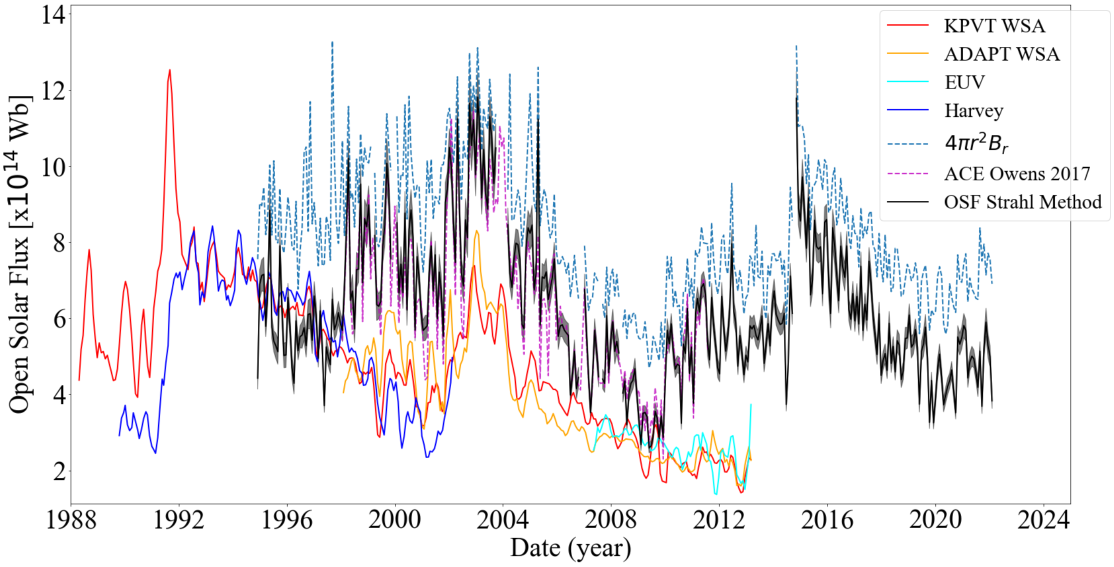

Figure 5.14: Comparison of *in-situ* and photospheric magnetogram estimates of OSF. The best estimate from the current study is shown in *black* with errors as the *grey shaded region*, which is displayed as CR averages. The *dashed magenta line* shows the OSF calculated from Owens et al. (2017), also as CR averages. The *dashed pale blue line* shows the OSF calculated from $\Phi_{R=1\text{AU}}$. The *coloured lines* are magnetogram estimates from KPVT (*red line*), ADAPT (*orange line*), EUV (*cyan line*), Harvey (*blue line*), displayed as 3 CR averages, from Wallace et al. (2019).

Chapter 6

HMF Topologies Around True Polarity Reversals

The open solar flux (OSF) is the extension of the Sun's magnetic field that maps into the heliosphere. This OSF is either directed toward or away from the Sun, the distinction between which can be made using the method outlined in Chapter 4.

The heliospheric current sheet (HCS) is the extension of the source surface neutral line into interplanetary space. A true polarity reversal occurs at the HCS when the field changes direction from away to toward or vice-versa and this reflects the connectivity of the field (i.e. toward is connected to the solar corona and away extends further into the heliosphere). An example of a "false" polarity reversal can be caused by locally inverted magnetic fields giving the indication that the field's polarity has flipped when in reality its ultimate connectivity has remained the same as this inversion does not directly map all the way back to the source surface. At the HCS, magnetic reconnection can occur between the oppositely directed fields, which affects the topology of the HMF.

This chapter describes the occurrence of HMF topologies with respect to the HCS, in order to better understand the formation and evolution of the HMF. Sections 6.1 and 6.1.1 introduce some background to the HCS and Section 6.1.2 reviews some previous studies investigating some solar wind properties at the HCS. In Section 6.2

the method for determining the location of the true polarity reversals (i.e. the HCS) is outlined. In Section 6.3, the variation of the solar wind properties and magnetic field topologies around true polarity reversals are investigated. In Section 6.3.5, evidence for the formation mechanism of inverted flux is outlined. Finally, the main results are summarised in Section 6.4.

6.1 Introduction

The heliospheric magnetic field (HMF) is the extension of the Sun's magnetic field that threads the solar photosphere and extends to a sufficient altitude that it is dragged out by the solar wind (Levine et al., 1977, Owens and Forsyth, 2013). Figure 6.1 shows a sketch of the heliospheric current sheet (HCS), which is the surface separating the regions of oppositely directed open magnetic fields of Toward and Away (to/from the Sun) topology (Smith, 2001, Riley et al., 2002).

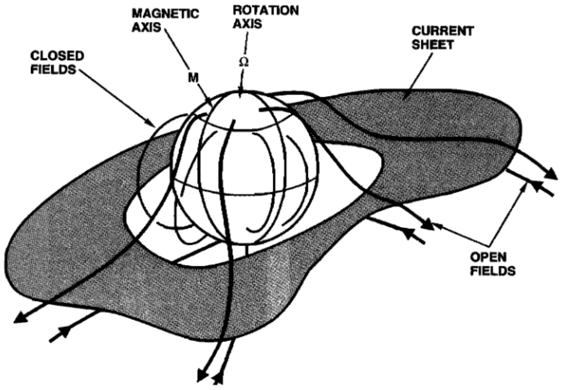

Figure 6.1: Schematic of the heliospheric current sheet from Smith (2001). The shaded region is the current sheet separating the opposite magnetic fields of "Toward" and "Away" topology.

The orientation of the HCS evolves systematically over the solar cycle (Smith, 2001). At solar minimum, the polar fields dominate and the HCS is nearly flat and lies close to the solar equator. Through the rising phase of the cycle, the HCS becomes increasingly inclined with respect to the equator as the polar fields weaken and the quadrupolar component of the solar magnetic field increases. At solar maximum, with no unipolar high-latitude fields, the HCS can extend up to the poles (Hoeksema, 1995).

Using magnetogram measurements of the Sun, the radial magnetic field can be extrapolated using a potential field model, see Section 2.1.1 for more information. The HCS can then be identified as the location of zero field between oppositely-directed fields of opposite topology (the neutral line on the source surface) (Hoeksema et al., 1982).

Using observations of the solar wind electron Strahl, which always travels outward from the Sun, open and closed field lines in the solar wind can be distinguished from each other. Times when the strahl is locally moving sunward suggest the topology of the HMF is evolving, likely as a result of near-Sun reconnection. This may be expected to preferentially occur near the HCS (Gosling et al., 2006), an effect which will be investigated here.

6.1.1 Magnetic Reconnection

As previously discussed in Section 1.2.3, magnetic reconnection can allow the configuration of the HMF to evolve. Figure 6.2 shows a simple sketch of the geometry of magnetic reconnection. Panel A shows the current sheet between the two oppositely directed magnetic field lines in red and blue, with plasma flows forcing them to pinch together. In panel B, the opposite fields are brought together by diffusion where they meet and effectively cross-connect, releasing large amounts of energy. The field lines evolve from having the topology or running along the current sheet to the topology of threading the current sheet, passing through the "separatrices" which is where the field lines from opposite sides of the current sheet first touch and so have both topologies simultaneously. In panel C, the now reconnected fields are strongly bent so are subject to the "magnetic tension force" which straightens the bent field lines. This results in plasma jets and frozen-in fields being ejected along the current sheet. This ejection of plasma brings more plasma into the diffuse region, carrying more magnetic fields to reconnect (Hesse and Cassak, 2020).

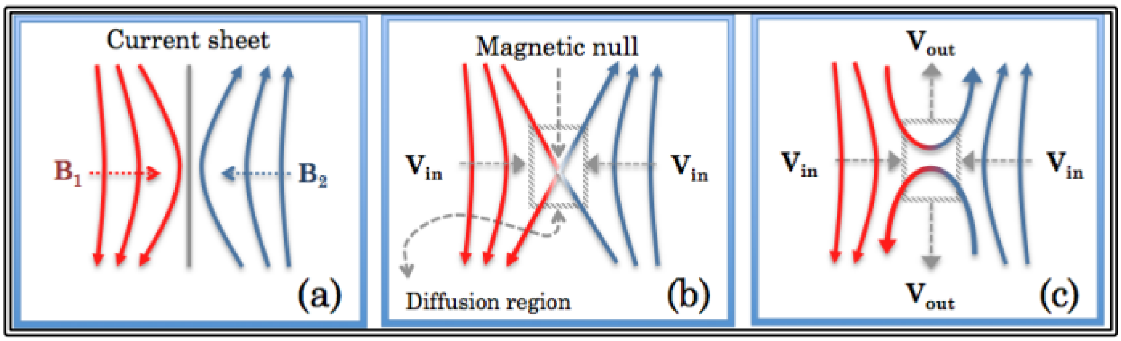

Figure 6.2: Figure from Genestreti et al. (2012) showing the geometry of magnetic reconnection. The red and blue lines illustrate magnetic field lines of opposite polarity.

Figure 6.3 shows a sketch of how magnetic reconnection can occur at or below the source surface to produce disconnected or inverted HMF. The top panel shows the reconnection between two open field lines which results in disconnected HMF and a new coronal loop which does not contribute to the HMF. Such loops have been observed in coronograph images, collapsing back toward the Sun under the magnetic tension force (Sheeley and Wang, 2002). The bottom panel shows the reconnection between an open field line and a closed heliospheric loop (such as contained in a coronal mass ejection), producing locally inverted HMF and a closed coronal loop. Both forms of reconnection lead to the same reduction in OSF (Owens et al., 2011).

6.1.2 Statistical Analysis of HCS Crossings

Superposed epoch analysis (also known as “Chree analysis” (Chree, 1913) or “compositing”) is a procedure used to determine the average behaviour relative to some reference time or feature. A superposed epoch analysis is carried out by binning the data into time bins relative to the target event. Here we use this method to analyse the average structure of the HMF around the HCS.

Borrini et al. (1981) investigated the abundance ratios of helium and hydrogen near the heliospheric current sheet, with the aim of understanding a link to coronal hole conditions. They identified the location of the HCS by a change in magnetic field

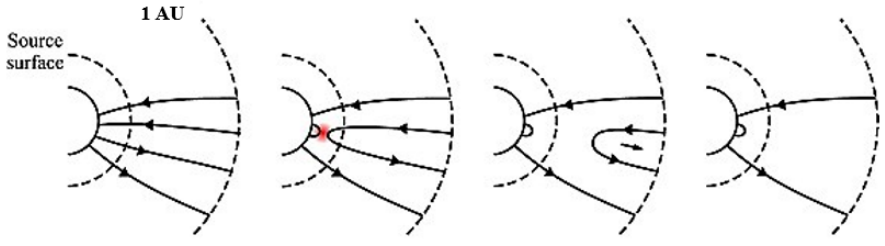

Pinching through disconnection

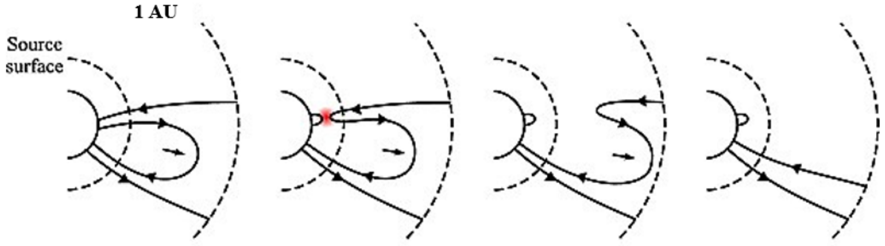

Pinching through interchange reconnection

Figure 6.3: Figure adapted from Owens et al. (2011) showing the reconnection of opposite field lines to produce disconnected flux and inverted flux. The top panel shows the reconnection between open field lines which results in disconnected flux. The bottom panel shows the reconnection between open and closed field lines which does not produce disconnected flux. Instead, the field is locally inverted before straightening further into the heliosphere.

direction that was both preceded and followed by at least 4 days of constant magnetic polarity. Superposed epoch analyses were carried out of solar wind data from IMP 6, 7, and 8 from 1971 to 1978. Borrini et al. (1981) split the data into 2-year intervals to investigate any solar cycle variation ± 20 days from the target time, and they also split the data according to the field polarity prior to the HCS (i.e. whether the HCS was a transition from toward to away magnetic polarity or vice versa). Splitting the data in these ways made no significant differences to the results of the superposed epoch analyses. In the combined result, the alpha-proton flux ratio demonstrated a pronounced minimum at the HCS of $\sim 30\%$. In the 2-year intervals, the minimum in the alpha-proton flux ratio remained statistically significant.

Thomas et al. (2014) performed similar superposed epoch analyses to investigate the galactic cosmic ray flux at the HCS. Before performing the analysis, they split the data according to different HCS criteria, namely the change in magnetic polarity and the strength of any associated solar wind compression. In addition, they tested the significance of any variations by a Monte-Carlo approach, where the same analysis was repeated for the same number of randomly selected times before being repeated 1000 times to represent the background conditions of each variable. They detected polarity reversals with an average occurrence of 1 per 45 days. Thomas et al. (2014) show that the structure of the HCS, as seen in GCR fluxes depends on the Toward/Away polarity seen ahead on the HCS crossing and on the degree of compression seen after the crossing when the HCS is also a stream interaction where fast solar wind catches up to slower solar wind.

6.2 Methods

6.2.1 Topology of the Field

As explained in Chapter 4, the combined radial magnetic field and suprathermal electron *in-situ* observations were used to determine whether the topology of the magnetic field was open, closed, locally inverted, or disconnected. To summarise: to be categorised as open, the positive/negative radial magnetic field needs to be accompanied by a parallel/anti-parallel Strahl signature. For a closed field, the direction of consecutive magnetic field measurements will change and the Strahl signature needs to be visible in both directions. To identify inverted flux, the radial magnetic field component would be positive/negative with an anti-parallel/parallel Strahl signature, which is the opposite of the open flux. Finally, disconnected flux would show no Strahl signature.

6.2.2 Determining Field Polarity

In determining the field direction, we wanted to identify the location of true polarity reversals, where the field changed direction from being dominantly away to being dominantly toward (or visa versa), and this change maps to the source surface, not just a local inversion (i.e., the field polarity change reflects a change in the toward/away connectivity).

From the 128s magnetic field topologies calculated in Chapter 4, all the open flux data was assigned a value based on the polarity of the field. Fields directed toward/away from the Sun are assigned a value of +1 and fields directed inward/toward the Sun are assigned a value of -1. Unclassified and closed fields are assigned a value of 0.

Explicitly, the polarity is toward when the topology is open and $B_r > 0$ or the topology is inverted and $B_r < 0$. The polarity is away when the topology is open and $B_r < 0$ or the topology is inverted and $B_r > 0$.

These assigned values (+1, 0, -1) will be referred to as the 'polarity indicator'.

6.2.3 Locating True Polarity Reversals

The 128s magnetic field topologies were all assigned values according to their polarity, resulting in the 128s polarity indicators.

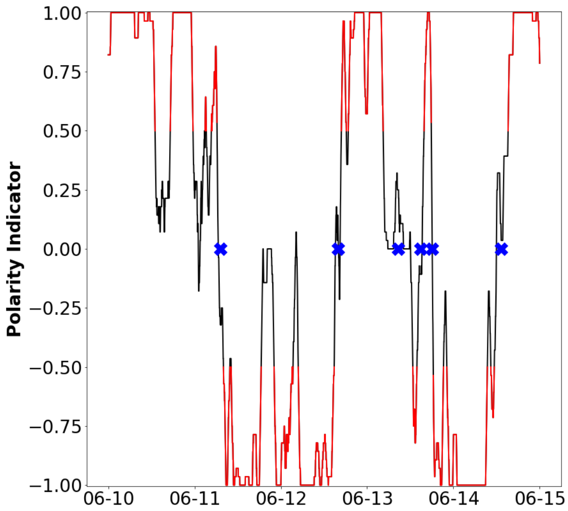

Figure 6.4: Polarity indicator for 5 days of data from 10th-15th June 2008. The *black line* is the hourly smoothed polarity indicator (+1 = toward, -1 = away), the *red line* is the smoothed polarity indicator showing the ± 0.5 minimum values to identify dominantly away/toward sectors, and the *blue crosses* show the location of polarity reversals.

A 1-hour smoothing was applied to the 128s polarity indicators to remove any rapid oscillations between extremes. This 1-hour smoothed data is plotted in black in Figure

6.4. Smoothing the polarity indicator produces a range of values between -1 and 1, which highlights the choice of boundary values to identify a polarity reversal.

Initially, we considered identifying reversals by a sign change in the polarity indicator, however, this yielded a number of rapid reversals. Instead of a sign change, we use a minimum value of ± 0.5, shown in red in Figure 6.4, in order to give well-defined polarity reversals. This brings the automated definition into closer agreement with the identification done by eye in the Borrini and Thomas studies.

6.2.4 Superposed Epoch Analysis Method

Each detected magnetic field reversal is used as the target time for the superposed epoch analysis. From these target times (also called epoch times), we extract *n* sets of data (*n* being the number of trigger times) from the hourly variation of each variable (inverted, uninverted, counterstreaming and unclassified flux percentages, and |B|, |v|, $\mathrm{N}_a/\mathrm{N}_p$ and N_p) 14 days before and after the event. Finally, we average all *n* sets to represent the net effect of each variable.

Using Monte Carlo sampling, the background conditions were determined. *n* random times were selected from the full data set and were used as the target times for the same analysis described above. The average of these *n* random times is a single net effect of each variable. This was repeated 1000 times, and the 5th/95th percentiles were used for the background conditions. Where the variations based on the polarity reversal target times fall outside the 5th/95th percentiles of the background variations, we can be confident that the trend is not simply due to random sampling but is likely the result of systematic structure associated with the HCS.

6.3 Results and Discussion

6.3.1 Field Direction

Using the method outlined in Section 6.2.2, the polarity reversals were identified from the field changing direction from being dominantly away to being dominantly toward, and visa versa. Figure 6.5 shows an example of the polarity indicator (top panel) and B_r (bottom panel) over the same 5-day interval as Figure 6.4. The number of reversals detected using just the sign change in B_r is much higher than the number of reversals detected using the combination of the magnetic field and Strahl data. Many of these reversals are not true polarity reversals and are instead local inversions in the magnetic field that do not map to the source surface, so are subsequently ignored. Figure 6.6 shows 5 days where there are multiple local inversions in B_r, but there are none detected by the polarity indicator.

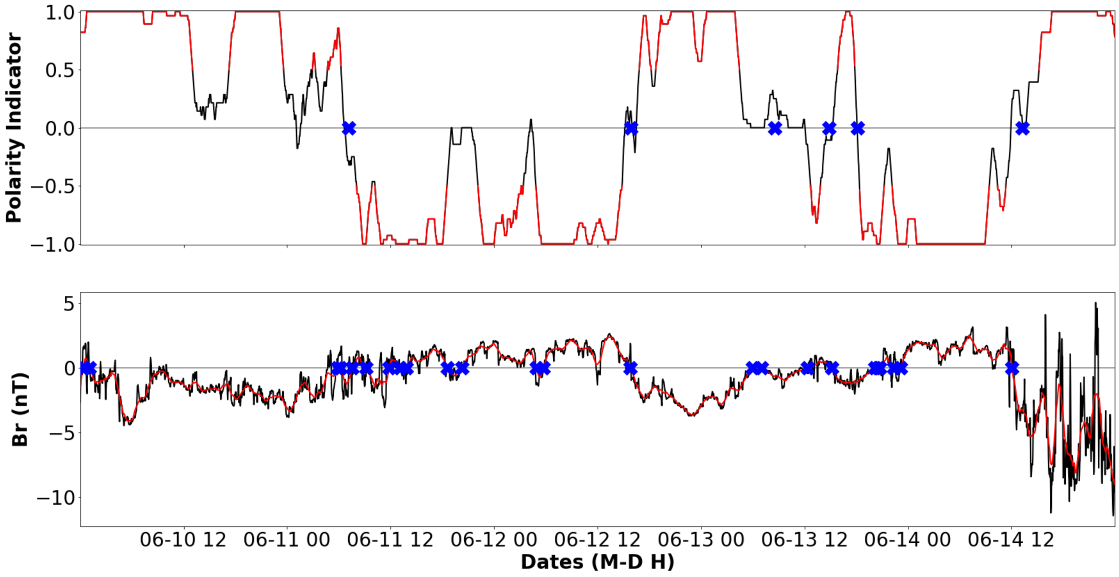

Figure 6.5: An example of the polarity indicator and B_r for 5 days of data from 10th-15th June 2008. (Top) The *black line* is the hourly smoothed polarity indicator (+1 = toward, -1 = away), the *red line* is the smoothed polarity indicator showing dominantly away/toward sectors, and the *blue crosses* show the location of polarity reversals. (Bottom) The *black line* is the 128s radial magnetic field, the *red line* is an hour running smooth of B_r, and the *blue crosses* show the location of the sign change in the hourly smoothed B_r.

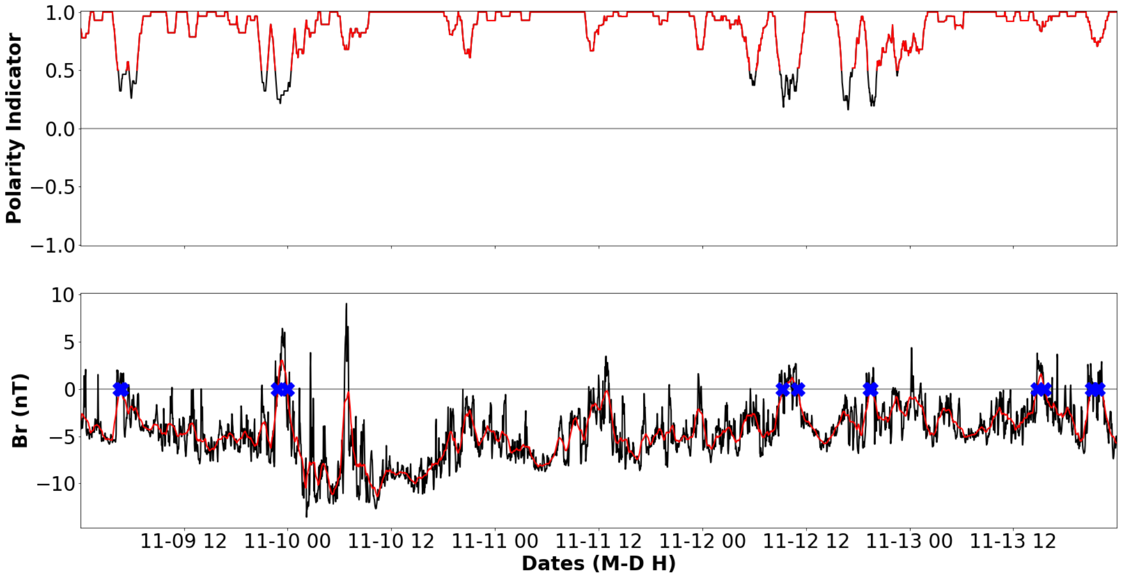

Figure 6.6: An example of the polarity indicator and B_r for 5 days of data from 9th-14th November 2014. (Top) The *black line* is the hourly smoothed polarity indicator (+1 = toward, -1 = away), the *red line* is the smoothed polarity indicator showing dominantly away/toward sectors, and the *blue crosses* show the location of polarity reversals. (Bottom) The *black line* is the 128s radial magnetic field, the *red line* is an hour running smooth of B_r, and the *blue crosses* show the location of the sign change in the hourly smoothed B_r.

Figure 6.7 shows where both the B_r sign change and polarity indicator detect a true polarity reversal. There is an offset between them of around 1 hour, with the polarity indicator identifying the reversal after the B_r sign change. Figure 6.8 shows another example where both the B_r sign change and polarity indicator detect a true polarity reversal, but this offset is 2.7 hours. Both of these offsets indicate relatively long periods of inverted HMF. These periods of inverted HMF are shorter than the 15+ hour intervals reported by Crooker et al. (2004).

6.3.2 Superposed Epoch Analysis

Figure 6.9 shows a breakdown of applying the superposed epoch analysis described in Section 6.2.4. This example shows the variation of B_r at an away-toward true polarity reversal. The left panel of Figure 6.9 shows two random variations (grey lines) of B_r from two independent epoch times. The result of averaging the variations from all n

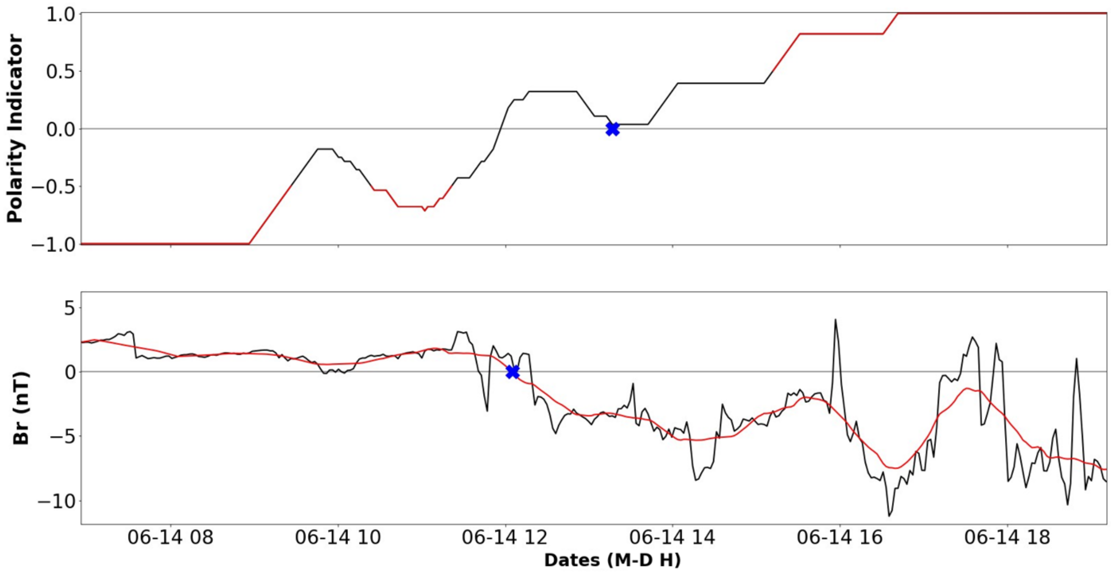

Figure 6.7: An example of the polarity indicator and B_r for 10 hours of data from 14th June 2008. (Top) The *black line* is the hourly smoothed polarity indicator ($+1$ = toward, -1 = away), the *red line* is the smoothed polarity indicator showing dominantly away/toward sectors, and the *blue crosses* show the location of polarity reversals. (Bottom) The *black line* is the 128s radial magnetic field, the *red line* is an hour running smooth of B_r, and the *blue crosses* show the location of the sign change in the hourly smoothed B_r.

epoch times, from the same time bins relative to the target time ($t = 0$), is plotted in red. The right panel shows the same average variation of B_r, without the random variations. Here the standard error of the mean is more easily visible. As explained in Section 6.2.4, Monte Carlo sampling is used to determine these background conditions. *n* random trigger times are selected from the full data set and the above analysis is carried out to produce a single net variation in B_r. This process is repeated a total of 1000 times, and the 5th/95th percentiles of the resulting variations represent the standard error (shown as the boundaries of the shaded grey region).

As shown by grey lines in the left panel of Figure 6.9, the background conditions can be extremely noisy. Since these random sets contribute to the background conditions, this highlights the importance of repeating the Monte Carlo sampling.

This analysis was applied to the ACE and *Wind* data set over the period 1994-2021 resulting in 3210 true polarity reversals, a reversal on average every 3 days. Since the

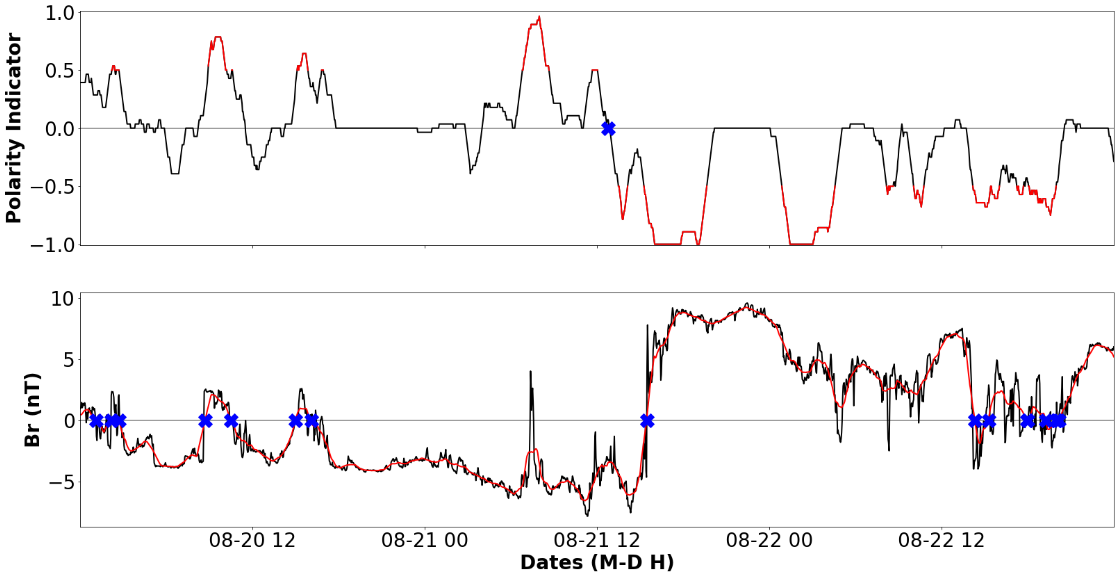

Figure 6.8: An example of the polarity indicator and B_r for 3 days of data from 20th-23rd August 2005. (Top) The *black line* is the hourly smoothed polarity indicator (+1 = toward, -1 = away), the *red line* is the smoothed polarity indicator showing dominantly away/toward sectors, and the *blue crosses* show the location of polarity reversals. (Bottom) The *black line* is the 128s radial magnetic field, the *red line* is an hour running smooth of B_r, and the *blue crosses* show the location of the sign change in the hourly smoothed B_r.

HCS typically passes over Earth between 2-6 times per CR (Smith, 2001), a maximum of 1 per 4.5 days, our detected number of reversals is high. This will be discussed more in Section 6.3.4 after a look at the initial results.

The occurrence rate of these reversals also indicates that there are further triggers in the window of study for the superposed epoch analysis, the effect of which is worth mentioning. The additional reversals can influence the observed signature by amplifying the variation or increasing the overall variability (noise) of the data. To rectify this overlap, trigger times would need to be identified in the absence of additional triggers within the window of study.

Figure 6.10 shows the percentages of inverted, open, counterstreaming, and unclassified flux on the top row, and the magnetic field magnitude |B|, velocity magnitude |v|, alpha-proton ratio N$_a$/N$_p$, and proton density N$_p$ on the bottom row (red line), ± 14 days relative to the epoch time. In this figure, the vertical black line marks the

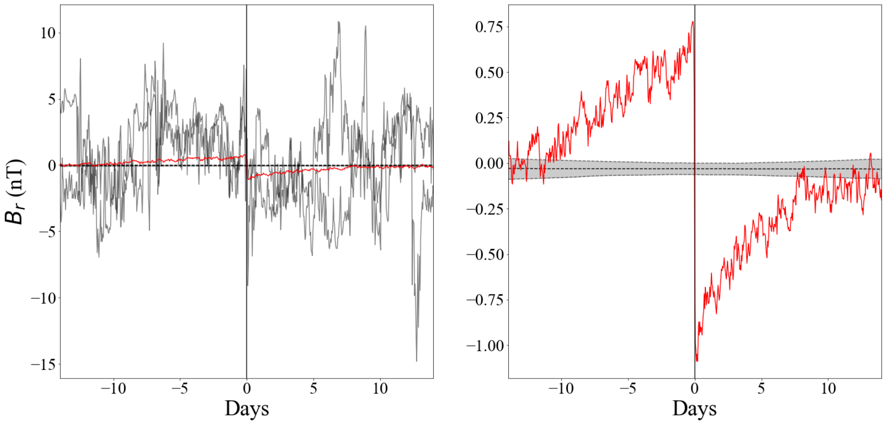

Figure 6.9: Superposed epoch plots of B_r at true polarity reversals. For this example, a subset of data of positive to negative crossing was selected. (Left) two random constituent B_r signatures (*grey lines*) and (Right) the B_r average signature (*red line*). Daily running averages are employed, and true polarity reversals are used as zero epochs. The shaded region shows the area between the 5th/95th percentiles (*black dashed lines*) of the background conditions, found by Monte Carlo sampling as described in Section 6.2.4.

location of the true polarity reversal ($t = 0$) and the grey band indicates the variance of each parameter expected from the limited sample size and random variations (5/95 percentile confidence intervals).

Each of these variations is considered in turn. Figure 6.10a shows the variation of the percentage of inverted flux. The most noticeable features are the two peaks of increased inverted flux prior to $t = 0$ at -3 and -9 days and the drop in inverted flux at +2 days. The peak at -3 days is discussed in Section 6.3.5 as a possible representation of the leading foot point for interchange reconnection. Panel b shows the percentage variation in uninverted (open) HMF. The most noticeable feature is the sharp decrease which coincides with the increase in counterstreaming (panel c) and unclassified (panel d) flux. (Of course, the occurrence of the four HMF classifications must sum to 100%). In panel e, |B| reaches its minimum around -2 days, shortly following the highest peak in inverted flux, before rapidly increasing to its peak at +1 days. In panel f, V sharply declines from -3 days to reach its minimum around -1 days before rapidly increasing to its peak around +3 days. In panel g, the most noticeable feature is the sharp trough in

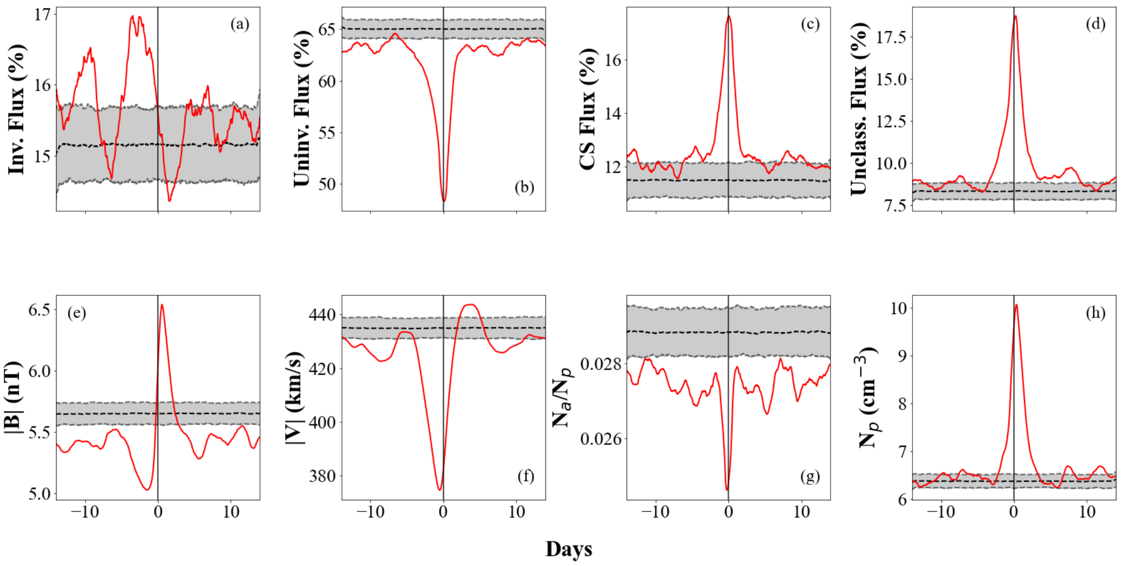

Figure 6.10: Superposed epoch plots of (a) inverted, (b) uninverted (open), (c) counterstreaming, and (d) unclassified flux percentages, and (e) |B|, (f) |v|, (g) N_a/N_p, and (h) N_p at true polarity reversals for all 3210 HCS crossings between 1994-2021. Daily running averages are employed, and true polarity reversals are used as zero epochs. The shaded region shows the extent of the standard error of the mean (black dashed line).

N_a/N_p at $t = 0$, which corresponds to the sharp peak in N_p in panel h. The signature in panel g closely corresponds to the results in Borrini et al. (1981), who also observed a sharp trough in the N_a/N_p and a sharp peak in N_p at the HCS. Independently of N_p, N_a follows a similar pattern to N_p with a sharp peak at the HCS.

To investigate the effect of the solar cycle phases, a year of data around each phase was isolated for each occurrence within the data. Explicitly, for solar minimum, one year of data was isolated from 1996, 2008, and 2019, and the combination of this data was used to find the mean response and the background conditions. Figure 6.11 shows the variation of the topology of the field over different phases of the solar cycle. The columns show plots of inverted (column a), uninverted (column b), counterstreaming (column c), and unclassified (column d) flux percentages at true polarity reversals. The mean responses (plotted in red) are hourly percentages with a daily running average applied. The rows show the use of all data (row i), solar minimum (row ii), solar maximum (row iii), rising phase (row iv), and declining phase (row v).

The solar cycle variation affects the inverted flux percentage more than the other topologies. In the plots of uninverted flux percentage, the sharp decrease is still evident at $t = 0$, as is the sharp increase in counterstreaming and unclassified flux. In the inverted flux percentage, the peaks at -3 and -9 days and the sharp decrease at $+2$ days disappear during solar maximum (a-iii). In the rising phase (a-iv) the peak at -9 days is much less significant than the peak at -3 days, which split into two distinct peaks. During the declining phase (a-v) the peak at -9 days is present, as well as the dual peaks at -3 days.

Figure 6.12 shows the variation of the magnitude of the magnetic field |B| (column a), the magnitude of the velocity |v| (column b), the alpha-proton ratio N$_a$/N$_p$ (column c), and the proton density N$_p$ (column d) at true polarity reversals. As in Figure 6.11, the rows in Figure 6.12 show the use of all data (row i), solar minimum (row ii), solar maximum (row iii), rising phase (row iv), and declining phase (row v).

During the solar cycle, the key features in |B|. In the declining phase, the trough in |v| at -1 days is much less significant than in other phases. One of the most noticeable results is the effect on N$_a$/N$_p$. Borrini et al. (1981) reported no significant differences in the results when splitting the data by solar cycle phase. While this is true during solar minimum (c-ii), we observe N$_a$/N$_p$ increasing at $t = 0$ during the remaining solar cycle phases. Meanwhile, the peak in N$_p$ at $t = 0$ is unaffected by the varying phases.

6.3.3 Offset Between Mean Values and Background

In Figure 6.10, there is a systematic offset between the mean value of the HCS intervals (plotted in red) and the background obtained from random sampling of the same data (grey band). This is clearly seen in panels *b*, *c*, and *d* where the signature sits just above/below the background. This offset is potentially caused by the HCS crossings preferentially clustering around certain solar cycle phases, as demonstrated in Figure 6.13.

The top panel of Figure 6.13 shows the daily sunspot number from SILSO World

Data Center (2022). The bottom panel shows the number of detected true polarity reversals for each Carrington rotation (CR) in the years 1994 - 2021, and the red line through the bottom panel is a 13-point running mean of the number of true polarity reversals. There are three main maxima in the number of reversals (HCS crossings): solar minimum in 1997, rising phase in 2012, and rising phase in 2021. These maxima show that the signatures in Figure 6.10 are predominantly made up of the solar minimum and rising phase. Since the random sampling for the background takes equally from all solar cycle phases, this creates the offsets seen in Figure 6.10. Another potential cause of the offset could be that the analysis is picking up CME fields in addition to HCS crossings.

6.3.4 Smoothing Period and the Number of Reversals

As briefly mentioned at the beginning of Section 6.3.2, the number of reversals detected over the entire ACE/*Wind* data set averaged as one every 3 days, which is higher than the expected maximum of 4.5 days (Smith, 2001). Over the 364 CRs of data, we detected 3210 reversals, averaging around 8.8 reversals per CR.

One possible resolution to decrease the number of detected reversals is to increase the smoothing interval applied to the data at the beginning of the analysis. Figure 6.14 shows the effect of the smoothing period on the number of detected reversals. For an interval of 364 CRs, the expected number of reversals is 2-6 per CR, however, this choice alone greatly affects the smoothing interval. 2 reversals per CR will require a smooth beyond what is plotted on this graph, while 4 reversals will require a smooth of ~ 20 hours and 6 reversals requires a smooth of ~ 3 hours. The selection of the correct smoothing interval would need more investigation.

During the analysis, removing ICMEs from the data using the ICME catalog compiled by Cane and Richardson (2003) was briefly looked at, but since it did not significantly change the mean responses in the data, it was decided to leave them in for the final analysis. However, while removing the ICMEs from the data does decrease the number of detected polarity reversals (to 2862), the occurrence remains high.

6.3.5 Formation of Inverted Flux

In Figure 6.10a there is a peak in inverted flux just prior to the field reversal at -3 days (roughly the solar wind transit time to 1 AU). This corresponds to the slow solar wind ahead of the HCS. Figure 6.11a shows the inverted flux percentage from all data (a-i), solar minimum (a-ii), solar maximum (a-iii), rising phase (a-iv), and declining phase (a-v). At solar minimum, Figure 6.11a-ii, there is a stronger signature present for inverted flux.

At solar minimum, it is more likely that magnetic field lines encountered near Earth ultimately connect to the polar regions at the photosphere. The HCS is generally to be confined to the solar equator at this time. As shown in Figure 6.15a, at higher latitudes the corona rotates faster than the photosphere, which longitudinally shears the open magnetic field lines. To reduce this shear, reconnection occurs between these open fields and small-scale closed loops, allowing the open magnetic flux to diffuse relative to the photosphere. This may produce inverted flux through the process shown in the bottom panel of Figure 6.3. Therefore, this peak of inverted flux at -3 days could represent the leading foot point for interchange reconnection.

Conversely, during solar maximum, it is less likely for magnetic field lines to extend to polar regions, due to the increased occurrence of coronal holes at lower latitudes. The HCS is also much more inclined at this time. This can result in the differential rotation of the corona forcing open flux of opposite polarities together, as shown in Figure 6.16. Reconnection occurs between these opposite fields to produce a disconnected flux through the process shown in the top panel of Figure 6.3. Given the lack of systematic ordering in the location of inverted HMF relative to the HCS at this time, we might expect the signature to be weaker in the super-posed epoch analysis.

6.4 Conclusions and Future Work

This study aimed to investigate the variation of solar wind properties and magnetic field topologies around true polarity reversals (i.e. HCS crossings which map back to the solar source surface). First, we determined the location of true polarity reversals where the polarity changes from toward (open topology and $B_r > 0$ or inverted topology and $B_r < 0$) to away (open topology and $B_r < 0$ or inverted topology and $B_r > 0$), or visa versa. To avoid detecting local rapid field flips, a 1-hour smooth is applied to the polarity of the field.

Each detected polarity reversal is used as the target time for the superposed epoch analysis. The variation of the magnetic field topologies and solar wind properties were investigated 14 days before and after the target time, covering a full solar rotation.

One of the key findings is that 3 days prior to the polarity reversal, a peak in inverted flux was identified which occurs at the minimum in the B-field and just before the solar wind speed drop. These properties align with the formation of inverted flux described in Section 6.3.5.

The work done in this study was a first look at the data, and there are a number of future directions I would be interested in taking. In a continuation of the study, I would aim to further investigate the signatures presented by this work, particularly the variation over different solar cycle phases, as this was only briefly touched on. In particular, N$_a$/N$_p$, which Borrini et al. (1981) reported being unaffected by the solar cycle phase but was observed to increase centred on $t = 0$, particularly in the declining phase, as shown in Figure 6.12c-v.

The major thing I would like to address in a follow-on study is the cause of the high number of polarity reversals per CR. I would like to determine first whether there were too many polarity reversals in every CR of data, which according to the bottom panel of Figure 6.13 seems unlikely to be the sole cause as a number of CRs have 2-6 polarity reversals, or whether there is some explanation in the data as to why there are more in different areas of data. There also appears to be some solar cycle dependence on the increased number of polarity reversals that would require further investigation. As mentioned in Section 6.3.4, one possible resolution to decrease the number of detected reversals is to increase the smoothing interval applied to the data at the beginning of the analysis, however, there is no obvious choice of smoothing interval, so this would require further investigation.

Finally, I would like to further investigate the choice of cutoff in the 'polarity indicator'. The ± 0.5 used in the present study appeared sensible in the examples from the data, but more rigorous testing alongside the choice of smoothing indicator would be preferred. Similar to the work done in previous chapters, a way to unambiguously determine the location of a true polarity reversal would be the objective.

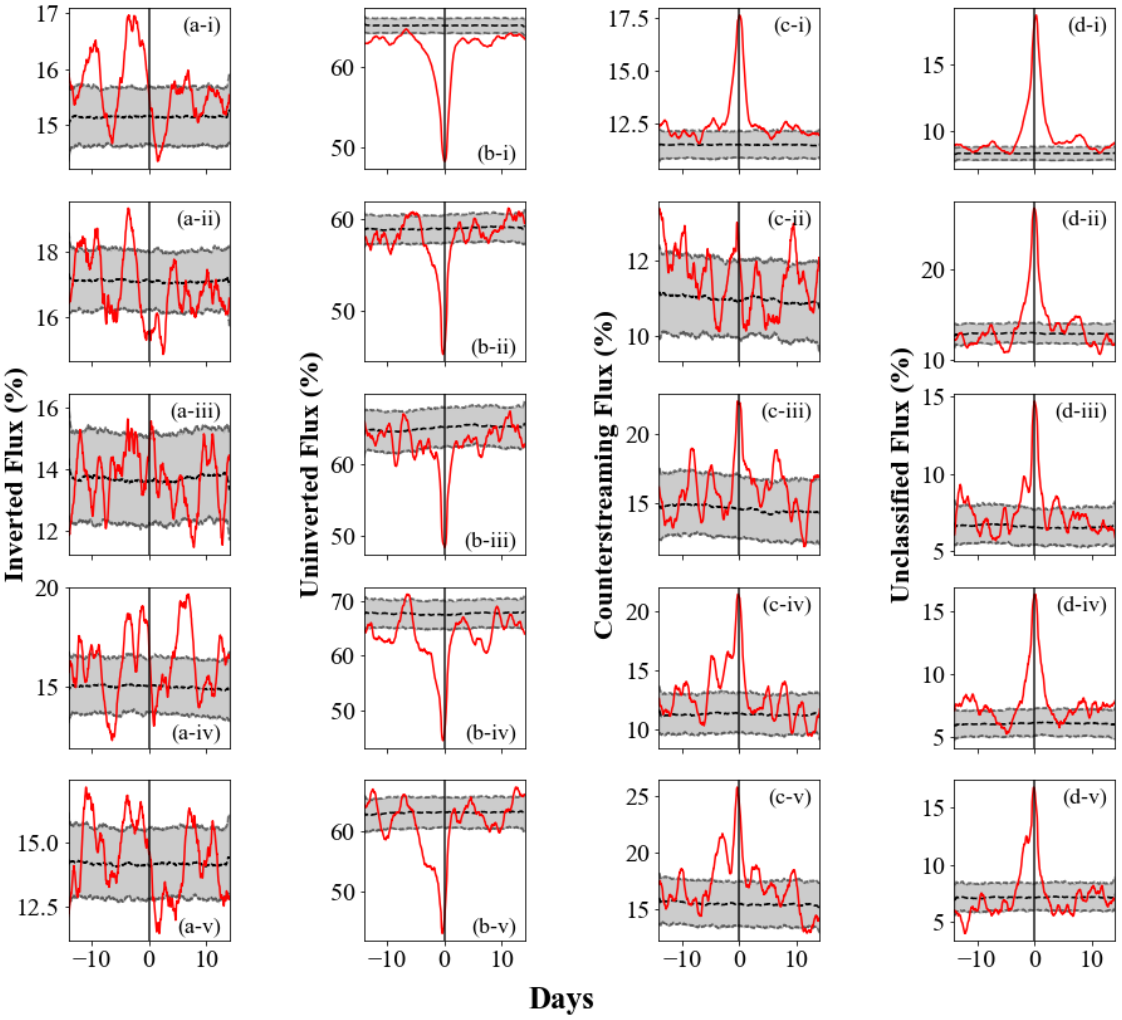

Figure 6.11: The effect of solar cycle on HMF topology about the HCS. Superposed epoch plots of inverted (column a), uninverted (column b), counterstreaming (column c), and unclassified (column d) flux percentages at true polarity reversals. Daily running averages are employed, and true polarity reversals are used as zero epochs. The rows correspond to the use of all data (i), solar minimum (ii), solar maximum (iii), rising phase (iv), and declining phase (v). The shaded region shows the extent of the standard error of the mean (black dashed line).

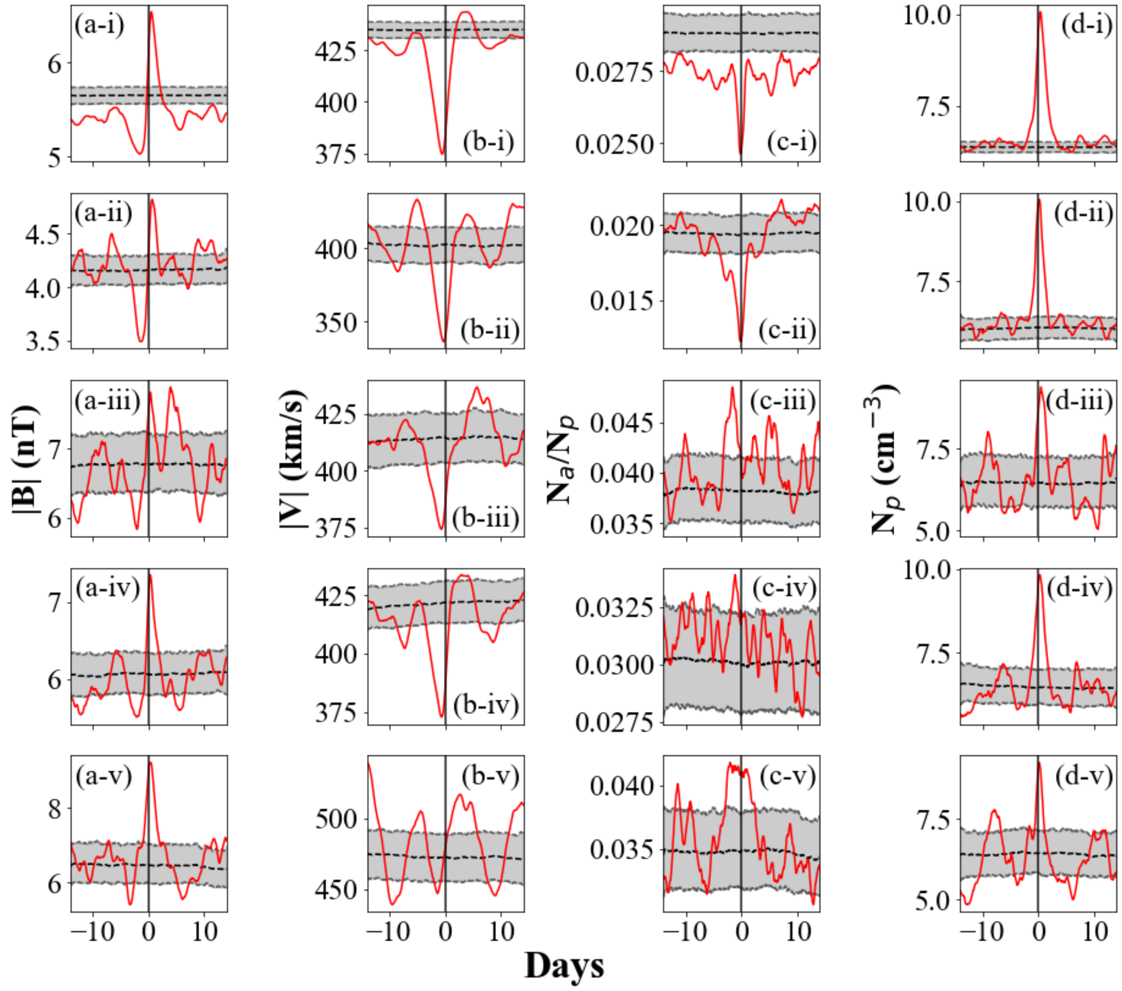

Figure 6.12: Effect of solar cycle on solar wind properties about the HCS. Superposed epoch plots of |B| (column a), |v| (column b), N_a/N_p (column c), and N_p (column d) at true polarity reversals. Daily running averages are employed, and true polarity reversals are used as zero epochs. The rows correspond to the use of all data (i), solar minimum (ii), solar maximum (iii), rising phase (iv), and declining phase (v). The shaded region shows the extent of the standard error of the mean (black dashed line).

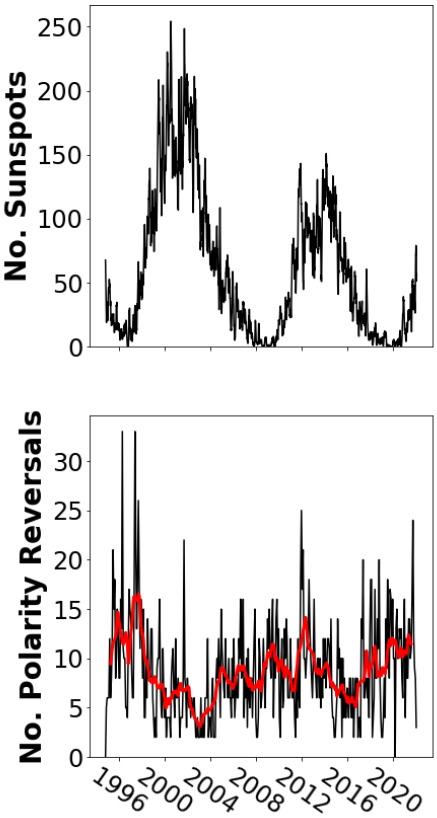

Figure 6.13: Top panel shows the daily sunspot number variation. The bottom panel shows the CR occurrence of true polarity reversals with a 13 CR running mean (*red line*).

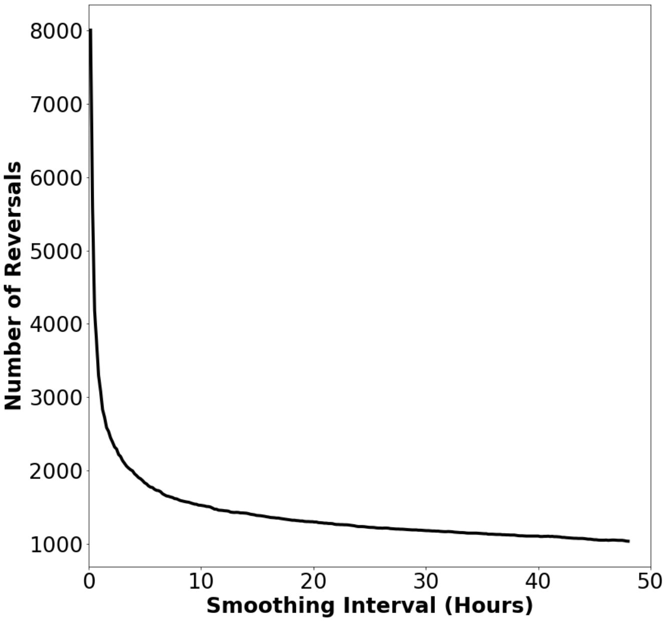

Figure 6.14: Number of true polarity reversals over the full 1994-2021 (364 CRs) data set with increasing smoothing interval.

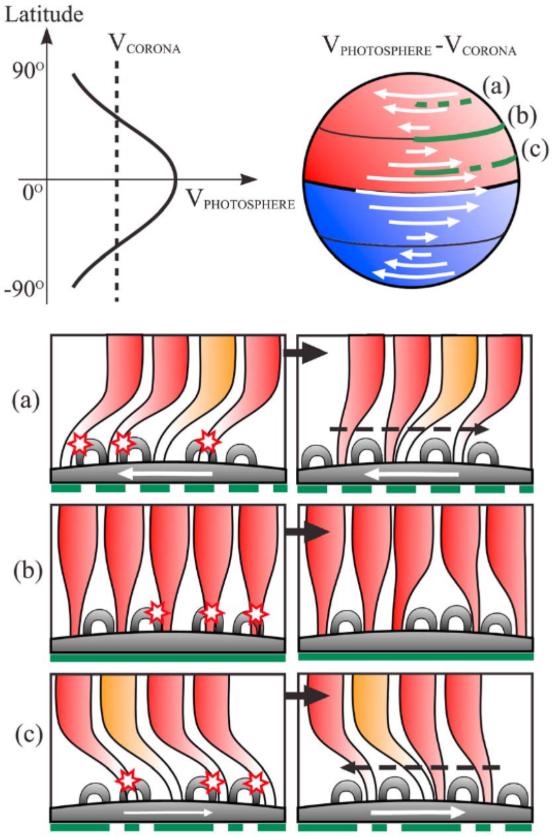

Figure 6.15: Schematic of the transport of open flux resulting from differential rotation of the photosphere, taken from Owens et al. (2011). The top panel shows the rotation speed of the photosphere compared to the corona, which rotates rigidly at the same speed as the midlatitude photosphere. At high latitudes, point a, the corona moves ahead of the photosphere, and flux tubes become longitudinally sheared. Reconnection between open flux and small-scale loops occurs to reduce shear, with open flux foot points "slipping" ahead of the photospheric magnetic field (in the direction of the dashed black arrow). At midlatitudes, point b, reconnection between open flux and small loops occur randomly, resulting in no net motion. At lower latitudes, point c, the photosphere moves ahead of the corona. Open flux is sheared and the open flux foot points move opposite to point a (in the direction of the dashed black arrow).

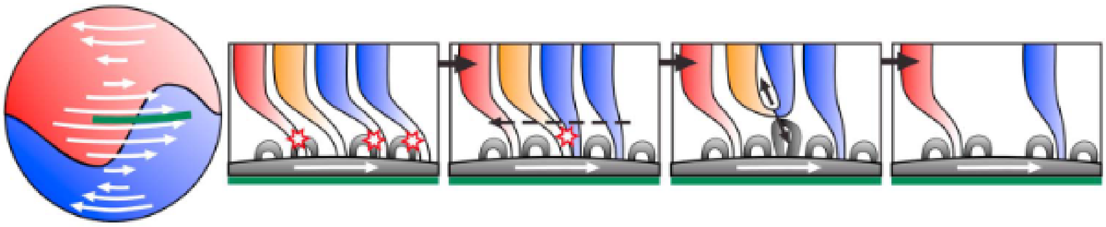

Figure 6.16: Schematic of the transport of open flux at an inclined HCS, taken from Owens et al. (2011). The red and blue colours represent the opposite magnetic field polarities, which are separated by an inclined HCS shown as a solid black line. Here the "slipping" of flux tubes (1st panel) force together open flux of opposite polarity (2nd panel). Reconnection between these flux tubes results in a disconnected loop (3rd panel) which will propagate out with the solar wind, reducing the OSF (4th panel).

Chapter 7

Conclusions and Future Work

The aims of this thesis are to quantify the Sun's open magnetic flux (OSF) and to understand its evolution with time. The OSF is the component of the Sun's magnetic field that reaches a sufficient height above the photosphere to be dragged into the heliosphere by the solar wind giving the Heliospheric Magnetic Field (HMF). The HMF is important because the near-Earth part, often called the Interplanetary Magnetic Field (IMF) controls energy transfer into the magnetosphere and hence space weather at Earth. It is useful to define a solar source surface, typically at an altitude of a few solar radii, where the all magnetic flux is OSF. Estimates of the OSF made on the basis of photospheric magnetic field observations currently disagree with the OSF estimates by *in-situ* spacecraft. As photospheric observations are the basis for all long lead-time space weather forecasts, the ability to reconstruct the OSF acts as a basic test of the coronal models. At present, however, photospheric estimates of OSF are around a factor of two lower than OSF estimates from *in-situ* spacecraft measurements.

Chapter 4 details how I determined the topology of the heliospheric magnetic field (HMF) from the combination of the electron and radial magnetic field data. In this chapter, I used observational results from four existing observational surveys to constrain the parameters used to automatically classify the topology of the HMF. Chapter 5 used these newly classified topologies to provide an improved estimate of OSF on the basis of *in-situ* spacecraft observations. Due to the removal of locally inverted flux, my OSF estimate is systematically lower than simple methods which assume all magnetic flux observed at 1 AU directly connects back to the solar source surface. While this contributes to the discrepancy between OSF estimates from *in-situ* and photospheric magnetograms, there is still some further disagreement. Finally, Chapter 6 investigated the variation of different HMF topologies and solar wind properties at true polarity reversals (i.e. those that are introduced into the HMF by polarity inversions at the source surface). Within this chapter the combination of these topologies and solar wind properties allows us to understand the formation of the detected inverted flux prior to polarity reversals.

7.1 Review of Results

7.1.1 Classifying the Topology of the HMF

The work in Chapter 4 combines *in-situ* electron and magnetic field data at 1 AU to determine the global topology of the HMF. I inter-calibrated and combined measurements from the *Wind* and ACE spacecraft to maximise the data coverage. Using the field-aligned suprathermal electron strahl, it is possible to determine if magnetic flux is directly connected to the Sun's surface or if it is locally inverted. Specifically, using the orientation of the strahl (either parallel or anti-parallel to the field) and the radial HMF component, I determined whether the field was topologically open (uninverted) (where the magnetic field direction and strahl orientation are toward and anti-parallel, or away and parallel) or locally inverted (toward and parallel, or away and anti-parallel).

The metrics to algorithmically determine the orientation of the strahl were referred to as the PAB (percentage above background) and PAO (percentage above opposite). The PAB refers to the suprathermal flux intensity above the background, which is used to first identify the presence of a strahl signature in either orientation (i.e. 0 or 180-degree pitch angle). The PAO is the amount of flux in relation to the other orientation, which is used to identify which orientation has the strongest signature. Using the results from four previous studies, Gosling et al. (1992), Skoug et al. (2000), Pagel, Crooker and Larson (2005), and Anderson et al. (2012), the PAB and PAO values were constrained to a small region of parameter space, the center of which we take the PAB and PAO values of 45 % and 140 % respectively. This means the strahl identification algorithm reproduces the results obtained by expert observers.

Using the optimum PAB and PAO values, the orientation of the strahl was combined with the radial magnetic field direction to determine the topology of the field. As stated above, the field was classified as open (or uninverted) by the magnetic field direction and strahl orientation being either toward and anti-parallel, or away and parallel. If the strahl direction is reversed, the magnetic field direction and strahl orientation being toward and parallel, or away and anti-parallel, then the field is classified as inverted. Where a strahl signature is present both parallel and anti-parallel, this indicates the presence of a closed loop, that is a HMF flux tube that has both ends connected to the source surface. Finally, where there is strahl data present but no clearly defined parallel/anti-parallel signature the field is classified as unclassified flux. One explanation for such a signature is that the flux is disconnected from the source surface at both ends.

Future Research Directions

A possible extension of this study would be to investigate the intervals of unclassified or disconnected flux, particularly those that appear to have a clear uni-directional signature by eye but did not meet the criteria. Is there any commonality between these intervals? Which topology would they have been classified as? What would be the effect on the following studies if these intervals were included? These are just a few questions I would be interested in answering.

A useful question to ask in this area is how the observable flux signature of the returning strahl on closed loops decays as the field line extends deeper into the heliosphere. When observing a closed loop we see bi-directional streaming strahl, but as the loop expands we eventually observe strahl traveling away from the Sun, with nothing coming back towards the Sun. If we could quantify the scattering per unit length along the field line we could work out how big the loop is, and as the toward flux decays work out how much the loop has grown. Knowing this could allow us to study how long it was since a given HMF field line emerged through the source surface which would help us understand and interpret heliospheric structure. However, research would need to be done on how these aims might be achieved.

7.1.2 Estimating the OSF from In-Situ Measurements

The work in Chapter 5 aimed to improve the method for estimating the OSF from *in-situ* spacecraft observations outlined in Owens et al. (2017) by extending the period of study and modifying the method of calculating the OSF. Using the field topologies calculated in Chapter 4, the OSF was estimated as the total unsigned magnetic flux threading the sphere at the radius of observation (1 AU) before subtracting twice the amount of inverted flux (to include the magnetic flux from the sunward strahl intervals and the unidentifiable return field).

In calculating the total unsigned magnetic flux, it was assumed that the unclassified flux is disconnected flux and does not contribute to the OSF. This is an important assumption, as the removal of this disconnected flux resulted in a consistently lower OSF. An alternative approach, used by Owens et al. (2017), assumed that the unclassified flux was made up of the same proportion of all other topologies, however, with the lack of a clear strahl signature the disconnected flux approach was more rational.

Comparing the two studies, the average OSF from Owens et al. (2017) is $6.45 \pm 1.21 \times 10^{14}\mathrm{Wb}$ for the period 1998-2011, and the average OSF from the modified method used here was $6.59 \pm 0.35 \times 10^{14}\mathrm{Wb}$ for the same time interval. Thus there is broad agreement between the two methods. Despite the removal of the locally inverted HMF, there is still a disagreement between the OSF calculated from *in-situ* measurements and the OSF calculated from magnetograms. While this discrepancy still remains, the removal of inverted HMF does begin to close the gap between the two methods.

The strahl-based estimate of OSF presented in this study can be approximated by the use of 20-hour averages of B_r in the standard total heliospheric flux calculation $4\pi R^2|B_r|$. This is useful for studies interested in longer-term variations, however, while this is adequate at the annual resolution, it is not suitable for CR variations. The time-averaging approximation is likely to slightly underestimate the solar cycle variation in OSF, by overestimating OSF during solar minimum and underestimating during solar maximum.

Future Research Directions

A possible extension of this study would be dependent on the results from Section 7.1.1. The unclassified intervals are assumed to be a proxy for disconnected flux, so understanding the true topologies of that data would further impact the OSF calculated in Chapter 5.

A major follow-on study from this work would be to test the assumption that the measurements made at one latitude are representative of all latitudes. While a latitudinal invariance in $R^2|B_r|$ has been observed in the heliosphere (Smith and Balogh, 1995), the uncertainty introduced to OSF estimates is nevertheless difficult to directly quantify. This possible follow-on study is discussed further in Section 7.2.

7.1.3 HMF Topologies Around True Polarity Reversals

The work in Chapter 6 aims to investigate the variation of solar wind properties and HMF topologies around true polarity reversals (i.e. HCS crossings which map back to the solar source surface). First, I determined the location of true polarity reversals where the polarity changes from toward (open topology and $B_r > 0$ or inverted topology and $B_r < 0$) to away (open topology and $B_r < 0$ or inverted topology and $B_r > 0$), or visa versa. To avoid detecting local rapid field flips, a 1-hour smooth is applied to the polarity of the field.

Each detected polarity reversal is used as the target time for the superposed epoch analysis, in order to determine the average variation. The occurrence of the field topologies calculated in Chapter 4 and solar wind properties ($|V|$, $|B|$, N_a/N_p, and N_p) were investigated 14 days before and after the target time, covering a full solar rotation. One of the key findings is that 3 days prior to the polarity reversal, a peak in inverted flux was identified which occurs at the minimum in the HMF intensity and just before the solar wind speed drop. These properties align with the formation of inverted flux presented within that chapter.

Future Research Directions

A possible extension of this study would be to address the cause of the high number of polarity reversals per CR obtained using my automated algorithm. There appears to be some solar cycle dependence on the increased number of polarity reversals that would be interesting to investigate further, however, it is more the case that the absolute number of reversals is too high.

In a continuation of the study, I would aim to further investigate the signatures presented in this work, particularly the variation over different solar cycle phases, as this was only briefly touched on. In particular, N_a/N_p, which Borrini et al. (1981) reported being unaffected by the solar cycle phase but was observed to increase at $t = 0$, particularly in the declining phase.

Finally, I would like to further investigate the choice of cutoff in the 'polarity indicator'. The ± 0.5 used in the present study appeared sensible in the examples from the data, but more rigorous testing alongside the choice of smoothing indicator would be preferred. Similar to the work done in previous chapters, a way to unambiguously determine the location of a true polarity reversal would be the objective.

7.2 Future Work: Ulysses

A major outstanding assumption that spans much of the work done in this thesis is that the OSF estimates from *in-situ* data are made at one latitude and are assumed to be representative of all latitudes. I.e. $R^2|B_r|$ is assumed to be constant with latitude due to the equalisation of tangential magnetic pressure. This is expected to occur relatively close to the Sun, inside the Alfvén point, within $\approx 10R_\odot$ (Suess et al., 1996, Suess and Smith, 1996, Suess et al., 1998).

While a latitudinal invariance in $R^2|B_r|$ has been observed in the heliosphere (Smith and Balogh, 1995), these observations were made over the course of a year and could be aliased with the time evolution of the HMF. Thus the uncertainty introduced to OSF estimates is difficult to directly quantify. In particular, HMF inversions have been observed close to the Sun (Badman et al., 2021) and tend to increase in occurrence with R (Macneil et al., 2020), but maybe not equally at all latitudes (Lockwood and Owens, 2009). If inversions are being created in the heliosphere and preferentially in the slow solar wind (Owens et al., 2013), then $R^2|B_r|$ may vary inside/outside the streamer belt. Indeed, some MHD models of the corona do show this characteristic. While $R^2|B_r|$ may be different at the equator and poles, the actual OSF per unit latitude should be fixed at the near-Sun value (as it cannot easily equilibrate in the supersonic solar wind).

A possible approach to test this assumption is to use electron (Bame et al., 1992) and magnetic field (Balogh et al., 1992) data from the Ulysses spacecraft (Wenzel et al., 1992), which carried out observations in a heliocentric orbit inclined at $80.2°$ to the solar equator with aphelion at ~ 5.4 AU from the Sun and a perihelion distance of ~ 1.34 AU. Correcting for the radial effect would allow the latitudinal effect to be investigated in isolation. With the previous extensive constraining of conditions used in the OSF calculations for ACE and *Wind*, the most consistent approach would be to convert the observations to the equivalent at 1AU. This would require converting the intensity of the peak and the background, as well as the Strahl width.

Testing for the removal of the radial effect, the Ulysses data would need to be confirmed to behave as expected with changing radial distance. One approach could be to look at the varying number density of electrons with the results in Stverak et al. (2009). I have carried out some preliminary analysis of these data by isolating the data from the slow wind and calculating the number density for the halo (background flux) and the Strahl. Explicitly, the number density was calculated using $n = \sum I_i \Delta\theta \text{sin}\theta_i$.

Comparing the variation of the number densities with the results from Stverak et al. (2009) shows consistent trends, see Figure 7.1. There is some variation between our results and those from Stverak et al. (2009) due to the paper reporting the density of electrons where we used the number density of electrons, however, there is good agreement between the two so this is deemed to be a suitable approximation.

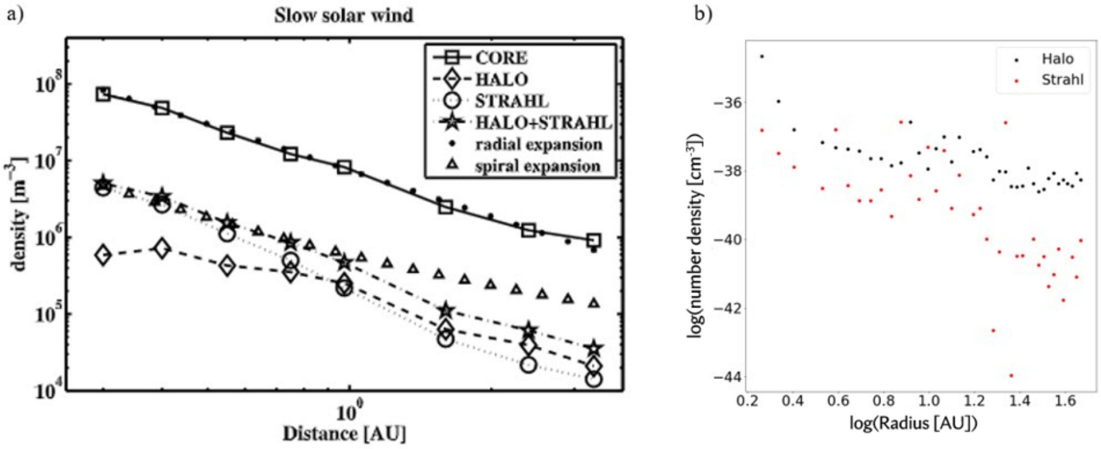

Figure 7.1: Panel (a) shows the radial evolution of the density profiles in the slow solar wind, from Stverak et al. (2009). Panel (b) shows the same slow solar wind radial evolution in intensity from the Ulysses data set.

The next step would be to convert the distribution to be able to reconstruct the pitch angle distribution. Using a Gaussian defined by Hammond et al. (1996),

$$j(\alpha) = K_0 + K_1 \text{exp}\left(-\frac{\alpha^2}{K_3^2}\right), \tag{7.1}$$

where j is the flux as a function of pitch angle, α, K_0 is the halo background, and K_3 is the width of the distribution (derived by $FWHM = 2\sqrt{\text{ln}2}K_3$). The unknown variable

K_1 can be found from the strahl number density, $n_{strahl} = \int_0^{180} \mathrm{d}\theta \sin\theta K_1 \exp\left(-\frac{\theta^2}{K_3^2}\right)$.

From Equation 7.1, the observations could be converted to the equivalent 1AU distribution. The same conditions as those used in Chapter 5 can be used to calculate the OSF and investigate the latitudinal variation in OSF.

A possible complication we have identified was that the time resolution of the Ulysses electron pitch-angle data is not consistent in time as it was within the ACE and *Wind* data sets. Specifically, it varies between approximately 7 and 34 minutes (which is potentially related to the two data rates, but this requires further investigation). This would require some modelling of the ACE and *Wind* data to understand the implications and enable further analysis.

References

Acuna, M. (1974), ‘Fluxgate magnetometers for outer planets exploration’, *IEEE Transactions on Magnetics* **10**(3), 519–523.

Alfvén, H. (1942), ‘Existence of electromagnetic-hydrodynamic waves’, *Nature* **150**(3805), 405–406.

Altschuler, M. D. and Newkirk, G. (1969), ‘Magnetic Fields and the Structure of the Solar Corona. I: Methods of Calculating Coronal Fields’, *Solar Phys.* **9**(1), 131–149.

Anderson, B. R., Skoug, R. M., Steinberg, J. T. and McComas, D. J. (2012), ‘Variability of the solar wind suprathermal electron strahl’, *J. Geophys. Res.: Space Phys.* **117**(A4).

Badman, S. T., Bale, Stuart D., Rouillard, Alexis P., Bowen, Trevor A., Bonnell, John W., Goetz, Keith, Harvey, Peter R., MacDowall, Robert J., Malaspina, David M. and Pulupa, Marc (2021), ‘Measurement of the open magnetic flux in the inner heliosphere down to 0.13 au’, *Astron. Astrophys.* **650**.

Bale, S. D., Badman, S. T., Bonnell, J. W., Bowen, T. A., Burgess, D., Case, A. W., Cattell, C. A., Chandran, B. D. G., Chaston, C. C., Chen, C. H. K., Drake, J. F., de Wit, T. D., Eastwood, J. P., Ergun, R. E., Farrell, W. M., Fong, C., Goetz, K., Goldstein, M., Goodrich, K. A., Harvey, P. R., Horbury, T. S., Howes, G. G., Kasper, J. C., Kellogg, P. J., Klimchuk, J. A., Korreck, K. E., Krasnoselskikh, V. V., Krucker, S., Laker, R., Larson, D. E., MacDowall, R. J., Maksimovic, M., Malaspina, D. M., Martinez-Oliveros, J., McComas, D. J., Meyer-Vernet, N., Moncuquet, M., Mozer, F. S., Phan, T. D., Pulupa, M., Raouafi, N. E., Salem, C., Stansby, D., Stevens, M., Szabo, A., Velli, M., Woolley, T. and Wygant, J. R. (2019), 'Highly structured slow solar wind emerging from an equatorial coronal hole', *Nature* pp. 1–6.

Balogh, A., Beek, T. J., Forsyth, R. J., Hedgecock, P. C., Marquedant, R. J., Smith, E. J., Southwood, D. J. and Tsurutani, B. T. (1992), 'The magnetic field investigation on the ULYSSES mission - Instrumentation and preliminary scientific results', *Astron. Astrophys.* **92**(2), 221–236.

Balogh, A., Forsyth, R. J., Lucek, E. A., Horbury, T. S. and Smith, E. J. (1999), 'Heliospheric magnetic field polarity inversions at high heliographic latitudes', *Geophys. Res. Lett.* **26**(6), 631–634.

Balogh, A., Hudson, H. S., Petrovay, K. and von Steiger, R. (2014), 'Introduction to the Solar Activity Cycle: Overview of Causes and Consequences', *Space Sci. Rev.* **186**(1-4), 1–15.

Bame, S. J., McComas, D. J., Barraclough, B. L., Phillips, J. L., Sofaly, K. J., Chavez, J. C., Goldstein, B. E. and Sakurai, R. K. (1992), 'The ULYSSES solar wind plasma experiment', *Astron. Astrophys.* **92**(2), 237–265.

Baumjohann, W. and Treumann, R. A. (1996), *Basic space plasma physics*.

Beckers, J. M. (1968), 'Principles of operation of solar magnetographs', *Solar Phys.* **5**(1), 15–28.

Biermann, L. (1951), 'Kometenschweife und solare korpuskularstrahlung', *Zeitschrift für Astrophysik* **29**, 274.

Bornmann, P. L., Speich, D., Hirman, J., Matheson, L., Grubb, R., Garcia, H. and Viereck, R. (1996), GOES x-ray sensor and its use in predicting solar-terrestrial disturbances, *in* E. R. Washwell, ed., 'GOES-8 and Beyond', Vol. 2812 of *Society of Photo-Optical Instrumentation Engineers (SPIE) Conference Series*, pp. 291–298.

Borrini, G., Gosling, J., Bame, S., Feldman, W. and Wilcox, J. (1981), 'Solar wind helium and hydrogen structure near the heliospheric current sheet: A signal of coronal streamers at 1 au', *Journal of Geophysical Research: Space Physics* **86**(A6), 4565–4573.

Bothmer, V. and Daglis, I. A. (2007), *Space weather: physics and effects*, Springer Science & Business Media.

Cane, H. V. and Richardson, I. G. (2003), 'Interplanetary coronal mass ejections in the near-earth solar wind during 1996–2002', *Journal of Geophysical Research: Space Physics* **108**(A4).
URL: *https://agupubs.onlinelibrary.wiley.com/doi/abs/10.1029/2002JA009817*

Chamberlain, J. W. (1960), 'Interplanetary Gas.II. Expansion of a Model Solar Corona.', *Astrophys. J.* **131**, 47.

Charbonneau, P. (2020), 'Dynamo models of the solar cycle', *Living Reviews in Solar Physics* **17**(1), 4.

Chree, C. (1913), 'Some Phenomena of Sunspots and of Terrestrial Magnetism at Kew Observatory', *Philosophical Transactions of the Royal Society of London Series A* **212**, 75–116.

Christian, E. R. and Davis, A. J. (2019), 'Advanced composition explorer (ace) mission overview'.
URL: *https://izw1.caltech.edu/ACE/ace_mission.html*

Cranmer, S. R. (2009), 'Coronal holes', *Living Rev. Solar Phys.* **6**(1), 1–66.

Cranmer, S. R. (2019), Solar-Wind Origin, *in* 'Oxford Research Encyclopedia of Physics', p. 18.

Crooker, N., Burton, M., Siscoe, G., Kahler, S., Gosling, J. and Smith, E. (1996), 'Solar wind streamer belt structure', *J. Geophys. Res.: Space Phys.* **101**(A11), 24331–24341.

Crooker, N. U., Kahler, S., Larson, D. and Lin, R. (2004), 'Large-scale magnetic field inversions at sector boundaries', *J. Geophys. Res.: Space Phys.* **109**(A3), 1–7.

de Patoul, J. (2012), Stereoscopy and Tomography of Coronal Structures, PhD thesis, Max-Planck-Institute for Solar System Research, Lindau.

Dungey, J. W. (1961), 'Interplanetary Magnetic Field and the Auroral Zones', *Phys. Rev. Lett.* **6**, 47–48.

Echim, M. M., Lemaire, J. and Lie-Svendsen, Ø. (2011), 'A review on solar wind modeling: Kinetic and fluid aspects', *Surveys in Geophysics* **32**, 1–70.

Erdos, G. and Balogh, A. (2014), 'Magnetic flux density in the heliosphere through several solar cycles', *Astrophys. J.* **781**(1), 50.

Feldman, W. C., Asbridge, J. R., Bame, S. J., Montgomery, M. D. and Gary, S. P. (1975), 'Solar wind electrons', *J. Geophys. Res.* **80**(31), 4181–4196.

Frost, A., Owens, M., Macneil, A. and Lockwood, M. (2022), 'Estimating the open solar flux from in-situ measurements', *Solar Physics* .

Genestreti, K., Kistler, L. and Mouikis, C. (2012), The role and dynamics of oxygen of ionospheric origin in magnetopause reconnection, PhD thesis.

Gosling, J., McComas, D., Skoug, R. and Smith, C. (2006), 'Magnetic reconnection at the heliospheric current sheet and the formation of closed magnetic field lines in the solar wind', *Geophysical Research Letters* **33**(17).
URL: *https://agupubs.onlinelibrary.wiley.com/doi/abs/10.1029/2006GL027188*

Gosling, J. T., Baker, D. N., Bame, S. J., Feldman, W. C., Zwickl, R. D. and Smith, E. J. (1987), 'Bidirectional solar wind electron heat flux events', *J. Geophys. Res.: Space Phys.* **92**(A8), 8519–8535.

Gosling, J. T., McComas, D. J., Phillips, J. L. and Bame, S. J. (1992), 'Counterstreaming solar wind halo electron events: Solar cycle variations', *J. Geophys. Res.: Space Phys.* **97**(A5), 6531–6535.

Gosling, J. T., Skoug, R. M. and Feldman, W. C. (2001), 'Solar wind electron halo depletions at 90° pitch angle', *Geophys. Res. Lett.* **28**(22), 4155–4158.

Graham, G. (2018), The Evolution of Solar Wind Strahl, PhD thesis, UCL (University College London).

Hale, G. E. and Nicholson, S. B. (1925), 'The Law of Sun-Spot Polarity', *Astrophys. J.* **62**, 270.

Hammond, C. M., Feldman, W. C., McComas, D. J., Phillips, J. L. and Forsyth, R. J. (1996), 'Variation of electron-strahl width in the high-speed solar wind: ULYSSES observations.', *Astron. Astrophys.* **316**, 350–354.

Hampshire, Damien, P. (2018), 'A Derivation of maxwell's Equations Using the Heaviside Notation', *Phil.Trans.R.Soc., A* **376**, 20170447.
URL: *https://royalsocietypublishing.org/doi/epdf/10.1098/rsta.2017.0447*

Hathaway, D. (2017), 'The sunspot cycle'.
URL: *https://solarscience.msfc.nasa.gov/SunspotCycle.shtml*

Hathaway, D. (2022), 'The solar interior'.
URL: *https://swc.nict.go.jp/en/knowledge/solar.html*

Heaviside, O. (2003), *Electromagnetic Theory*, American Mathematical Society, Providence, Rhode Island, USA.
URL: *https://books.google.com/books?hl=en&lr=&id=p2xEEAAAQBAJ&oi=fnd&pg=PP2&ots=59*

Hesse, M. and Cassak, P. A. (2020), 'Magnetic reconnection in the space sciences: Past, present, and future', *Journal of Geophysical Research: Space Physics* **125**(2).

Hoeksema, J. T. (1995), 'The Large-Scale Structure of the Heliospheric Current Sheet During the ULYSSES Epoch', *Space Sci. Rev.* **72**(1-2), 137–148.

Hoeksema, J. T., Wilcox, J. M. and Scherrer, P. H. (1982), 'Structure of the heliospheric current sheet in the early portion of sunspot cycle 21', *Journal of Geophysical Research: Space Physics* **87**(A12), 10331–10338.

Hoeksema, J. T., Wilcox, J. M. and Scherrer, P. H. (1983), 'The structure of the heliospheric current sheet: 1978-1982', *J. Geophys. Res.* **88**(A12), 9910–9918.

Hood, A. W. and Hughes, D. W. (2011), 'Solar magnetic fields', *Physics of the Earth and Planetary Interiors* **187**(3-4), 78–91.

Horbury, T. S., Woolley, T., Laker, R., Matteini, L., Eastwood, J., Bale, S. D., Velli, M., Chandran, B. D. G., Phan, T., Raouafi, N. E., Goetz, K., Harvey, P. R., Pulupa, M., Klein, K. G., Wit, T. D. d., Kasper, J. C., Korreck, K. E., Case, A. W., Stevens, M. L., Whittlesey, P., Larson, D., MacDowall, R. J., Malaspina, D. M. and Livi, R. (2020), 'Sharp Alfvénic Impulses in the Near-Sun Solar Wind', *Astron. Astrophys. Suppl.* **246**(2), 45. Publisher: American Astronomical Society.

Hudson, H. S., Svalgaard, L. and Hannah, I. G. (2014), 'Solar Sector Structure', *Space Sci. Rev.* **186**(1-4), 17–34.

Kahler, S., Crocker, N. and Gosling, J. (1996), 'The topology of intrasector reversals of the interplanetary magnetic field', *J. Geophys. Res.: Space Phys.* **101**(A11), 24373–24382.

Kahler, S., Crooker, N. U. and Gosling, J. T. (1998), 'Properties of interplanetary magnetic sector boundaries based on electron heat-flux flow directions', *Journal of*

Geophysical Research: Space Physics **103**(A9), 20603–20612.
URL: *https://agupubs.onlinelibrary.wiley.com/doi/abs/10.1029/98JA01745*

Kahler, S. and Lin, R. P. (1994), 'The determination of interplanetary magnetic field polarities around sector boundaries using e>2 kev electrons', *Geophys. Res. Lett.* **21**(15), 1575–1578.

Kahler, S. W. (1992), 'Solar flares and coronal mass ejections.', *Annu. Rev. Astron. Astrophys.* **30**, 113–141.

Kutner, M. L. (2003), *Astronomy: A Physical Perspective*, Cambridge University Press.

Lang, K. (1995), *Sun, Earth and Sky*, Springer.

Lee, C. O., Luhmann, J. G., Hoeksema, J. T., Sun, X., Arge, C. N. and de Pater, I. (2011), 'Coronal Field Opens at Lower Height During the Solar Cycles 22 and 23 Minimum Periods: IMF Comparison Suggests the Source Surface Should Be Lowered', *Solar Phys.* **269**(2), 367–388.

Lepping, R. P., Acũna, M. H., Burlaga, L. F., Farrell, W. M., Slavin, J. A., Schatten, K. H., Mariani, F., Ness, N. F., Neubauer, F. M., Whang, Y. C., Byrnes, J. B., Kennon, R. S., Panetta, P. V., Scheifele, J. and Worley, E. M. (1995), 'The Wind Magnetic Field Investigation', *Space Sci. Rev.* **71**(1-4), 207–229.

Levine, R., Altschuler, M. and Harvey, J. (1977), 'Solar sources of the interplanetary magnetic field and solar wind', *J. Geophys. Res.* **82**(7), 1061–1065.

Lin, R. L., Zhang, X. X., Liu, S. Q., Wang, Y. L. and Gong, J. C. (2010), 'A three-dimensional asymmetric magnetopause model', *J. Geophys. Res.: Space Phys.* **115**(A4).

Lin, R. P., Anderson, K. A., Ashford, S., Carlson, C., Curtis, D., Ergun, R., Larson, D., McFadden, J., McCarthy, M., Parks, G. K., Rème, H., Bosqued, J. M., Coutelier, J., Cotin, F., D'Uston, C., Wenzel, K. P., Sanderson, T. R., Henrion, J., Ronnet, J. C.

and Paschmann, G. (1995), 'A Three-Dimensional Plasma and Energetic Particle Investigation for the Wind Spacecraft', *Space Sci. Rev.* **71**(1-4), 125–153.

Lin, R. P. and Kahler, S. W. (1992), 'Interplanetary magnetic field connection to the sun during electron heat flux dropouts in the solar wind', *J. Geophys. Res.: Space Phys.* **97**(A6), 8203–8209.

Linker, J., Caplan, R., Downs, C., Riley, P., Mikic, Z., Lionello, R., Henney, C., Arge, C., Liu, Y., Derosa, M., Yeates, A. and Owens, M. (2017), 'The open flux problem', *Astrophys. J.* pp. 1–19.

Lockwood, M. (2016), 'Jim Dungey, The Open Magnetosphere, and Space Weather', *Space Weather* **14**(6), 380–383.
URL: *http://doi.wiley.com/10.1002/2016SW001438*

Lockwood, M. and Owens, M. (2009), 'The accuracy of using the ulysses result of the spatial invariance of the radial heliospheric field to compute the open solar flux', *Astrophys. J.* **701**(2), 964–973.

Lockwood, M. and Owens, M. J. (2013), 'Comment on "what causes the flux excess in the heliospheric magnetic field?" by e. j. smith', *J. Geophys. Res.: Space Phys.* **118**(5), 1880–1887.

Lockwood, M. and Owens, M. J. (2014), 'Centennial variations in sunspot number, open solar flux and streamer belt width: 3. modeling', *J. Geophys. Res.: Space Phys.* **119**(7), 5193–5209.

Lockwood, M., Owens, M. and Rouillard, A. (2009*a*), 'Excess open solar magnetic flux from satellite data: 1. analysis of the third perihelion ulysses pass', *J. Geophys. Res.: Space Phys.* **114**(A11).

Lockwood, M., Owens, M. and Rouillard, A. P. (2009*b*), 'Excess open solar magnetic flux from satellite data: 1. analysis of the third perihelion ulysses pass', *J. Geophys. Res.: Space Phys.* **114**(A11).

Lockwood, M., Owens, M. and Rouillard, A. P. (2009*c*), 'Excess open solar magnetic flux from satellite data: 2. a survey of kinematic effects', *J. Geophys. Res.: Space Phys.* **114**(A11).

Lockwood, M., Stamper, R. and Wild, M. (1999), 'Open magnetic flux: Variation with latitude and solar cycle', *Nature* **399**.

Macneil, A. (2018), Solar Wind Particle Populations at 1 AU: Examining their Origins in Advance of the Solar Orbiter Mission, PhD thesis, UCL (University College London).

Macneil, A. R., Owens, M. J., Wicks, R. T., Lockwood, M., Bentley, S. N. and Lang, M. (2020), 'The evolution of inverted magnetic fields through the inner heliosphere', *Mon. Not. Roy. Astron. Soc.* **494**(3), 3642–3655.

Maksimovic, M., Zouganelis, I., Chaufray, J.-Y., Issautier, K., Scime, E. E., Littleton, J. E., Marsch, E., McComas, D. J., Salem, C., Lin, R. P. and Elliott, H. (2005), 'Radial evolution of the electron distribution functions in the fast solar wind between 0.3 and 1.5 au', *Journal of Geophysical Research: Space Physics* **110**(A9).
URL: *https://agupubs.onlinelibrary.wiley.com/doi/abs/10.1029/2005JA011119*

Maxwell, J. C. (1864), 'Ii. a dynamical theory of the electromagnetic field', *Proceedings of the Royal Society of London* (13), 531–536.

McComas, D., Bame, S., Barker, P., Feldman, W., Phillips, J., Riley, P. and Griffee, J. (1998), 'Solar wind electron proton alpha monitor (swepam) for the advanced composition explorer', *Space Sci. Rev.* **86**(563–612).

McComas, D. J., Gosling, J. T., Phillips, J. L., Bame, S. J., Luhmann, J. G. and Smith, E. J. (1989), 'Electron heat flux dropouts in the solar wind: Evidence for interplanetary magnetic field reconnection?', *J. Geophys. Res.: Space Phys.* **94**(A6), 6907–6916.

Meyer-Vernet, N. (2007), *Basics of the Solar Wind*, Cambridge University Press.

Mueller, D., Marsden, R. G., Cyr, O. S. and Gilbert, H. R. (2013), 'Solar orbiter', *Solar Phys.* **285**(1), 25–70.

Nikolic, L. (2019), 'On solutions of the pfss model with gong synoptic maps for 2006–2018', *Space Weather* **17**(8), 1293–1311.
URL: *https://agupubs.onlinelibrary.wiley.com/doi/abs/10.1029/2019SW002205*

Norgard, J. (2017), *National Association of Broadcasters Engineering Handbook*, Taylor & Francis, chapter 1.1: The Electromagnetic Spectrum.

Ogilvie, K., Chornay, D., Fritzenreiter, R., Hunsaker, F., Keller, J., Lobell, J., Miller, G., Scudder, J., Sittler, E., Torbert, R. et al. (1995), 'Swe, a comprehensive plasma instrument for the wind spacecraft', *Space Science Reviews* **71**(1), 55–77.

Ogilvie, K. and Desch, M. (1997), 'The wind spacecraft and its early scientific results', *Advances in Space Research* **20**(4), 559–568. Results of the IASTP Program.
URL: *https://www.sciencedirect.com/science/article/pii/S0273117797004390*

Okamoto, T. J. and Sakurai, T. (2018), 'Super-strong magnetic field in sunspots', *The Astrophysical Journal Letters* **852**(1), L16.
URL: *https://dx.doi.org/10.3847/2041-8213/aaa3d8*

Owens, M., Arge, C. N., Crooker, N. U., Schwadron, N. A. and Horbury, T. S. (2008), 'Estimating total heliospheric magnetic flux from single-point in situ measurements', *J. Geophys. Res.: Space Phys.* **113**(A12), 1–8.

Owens, M. and Forsyth, R. (2013), 'The heliospheric magnetic field', *Living Rev. Solar Phys.* pp. 1–20.

Owens, M. J. and Crooker, N. U. (2006), 'Coronal mass ejections and magnetic flux buildup in the heliosphere', *J. Geophys. Res.* **111**(A10), A10104.

Owens, M. J., Crooker, N. U. and Lockwood, M. (2011), 'How is open solar magnetic flux lost over the solar cycle?', *Journal of Geophysical Research: Space Physics* **116**(A4).

URL: *https://agupubs.onlinelibrary.wiley.com/doi/abs/10.1029/2010JA016039*

Owens, M. J., Crooker, N. U. and Lockwood, M. (2013), 'Solar origin of heliospheric magnetic field inversions: Evidence for coronal loop opening within pseudostreamers', *J. Geophys. Res.: Space Phys.* **118**(5), 1868–1879.

Owens, M. J., McCracken, K. G., Lockwood, M. and Barnard, L. (2015), 'The heliospheric Hale cycle over the last 300 years and its implications for a "lost" late 18th century solar cycle', *Journal of Space Weather and Space Climate* **5**, A30.

Owens, M., Lockwood, M., Riley, P. and Linker, J. (2017), 'Sunward strahl: A method to unambiguously determine open solar flux from in situ spacecraft measurements using suprathermal electron data', *J. Geophys. Res.: Space Phys.* pp. 1–10.

Pagel, C., Crooker, N. U. and Larson, D. E. (2005), 'Assessing electron heat flux dropouts as signatures of magnetic field line disconnection from the sun', *Geophys. Res. Lett.* **32**(14).

Pagel, C., Crooker, N. U., Larson, D. E., Kahler, S. W. and Owens, M. J. (2005), 'Understanding electron heat flux signatures in the solar wind', *J. Geophys. Res.: Space Phys.* **110**(A1).

Parker, E. (1959), 'Extension of the Solar Corona into Interplanetary Space', *J. Geophys. Res.* **64**(11), 1675–1681.

Parker, E. N. (1958), 'Dynamics of the Interplanetary Gas and Magnetic Fields', *Astrophys. J.* **128**, 664.

Parker, E. N. (1965), 'Dynamical Theory of the Solar Wind', *Space Sci. Rev.* **4**(5-6), 666–708.

Paschmann, G. and Daly, P. W. (1998), ‘Analysis methods for multi-spacecraft data’, *International Space Science Institute* pp. 109 – 112.
URL: *https://www.issibern.ch/PDF-Files/analysis_methods_1_1a.pdf*

Riley, P. (2007), ‘An Alternative Interpretation of the Relationship between the Inferred Open Solar Flux and the Interplanetary Magnetic Field’, *Astrophys. J. Lett.* **667**, L97–L100.
URL: *http://10.0.4.62/522001*

Riley, P., Linker, J. A., Lionello, R. and Mikic, Z. (2012), ‘Corotating interaction regions during the recent solar minimum: The power and limitations of global mhd modeling’, *Journal of Atmospheric and Solar-Terrestrial Physics* **83**, 1–10.
URL: *https://www.sciencedirect.com/science/article/pii/S1364682611003464*

Riley, P., Linker, J. A. and Mikić, Z. (2001), ‘An empirically-driven global mhd model of the solar corona and inner heliosphere’, *Journal of Geophysical Research: Space Physics* **106**(A8), 15889–15901.
URL: *https://agupubs.onlinelibrary.wiley.com/doi/abs/10.1029/2000JA000121*

Riley, P., Linker, J. A., Mikić, Z., Lionello, R., Ledvina, S. A. and Luhmann, J. G. (2006), ‘A comparison between global solar magnetohydrodynamic and potential field source surface model results’, *The Astrophysical Journal* **653**(2), 1510.
URL: *https://dx.doi.org/10.1086/508565*

Riley, P., Linker, J. and Mikić, Z. (2002), ‘Modeling the heliospheric current sheet: Solar cycle variations’, *Journal of Geophysical Research: Space Physics* **107**(A7), SSH–8.

Riley, P., Linker, J., Mikic, Z., Caplan, R., Downs, C. and Thumm, J.-L. (2019), ‘Can an unobserved concentration of magnetic flux above the poles of the sun resolve the open flux problem?’, *Astrophys. J.* **884**, 18.

Russell, C. (2003), Solar system, magnetic and electric fields, *in* R. A. Meyers, ed., ‘Encyclopedia of Physical Science and Technology (Third Edition)’, third edition edn,

Academic Press, New York, pp. 189–209.
URL: *https://www.sciencedirect.com/science/article/pii/B0122274105007043*

Russell, C. T. (1971), 'Geophysical coordinate transformations.', *Cosmic Electrodynamics* **2**, 184–196.

Schatten, K. H. (1968a), 'Large-scale configuration of the coronal and interplanetary magnetic field', *Thesis, University of California* .

Schatten, K. H. (1968b), 'Prediction of the coronal structure for the solar eclipse of september 22, 1968', *Nature* (220).

Schatten, K. H. (1972), Current Sheet Magnetic Model for the Solar Corona, *in* C. P. Sonett, P. J. Coleman and J. M. Wilcox, eds, 'NASA Special Publication', Vol. 308, p. 44.

Schatten, K. H., Wilcox, J. M. and Ness, N. F. (1969), 'A model of interplanetary and coronal magnetic fields', *Solar Physics* **6**(3), 442–455.

Schrijver, C. J. and Siscoe, G. L. (2010), *Heliophysics: Space Storms and Radiation: Causes and Effects*, Cambridge University Press.

Schwabe, H. (1844), 'Sonnenbeobachtungen im Jahre 1843. Von Herrn Hofrath Schwabe in Dessau', *Astronomische Nachrichten* **21**(15), 233.

Senthilmurugan, S., Ganesh, V. and Prabhu, A. (2020), 'Design and implementation of three axis fluxgate magnetometer and its applications', *International Journal of Innovative Technology and Exploring Engineering* .
URL: *https://www.ijitee.org/wp-content/uploads/papers/v9i4/D1186029420.pdf*

Sheeley, N. R., J. and Wang, Y. M. (2002), 'Characteristics of Coronal Inflows', *Astrophys. J.* **579**(2), 874–887.

Shue, J.-H., Chao, J. K., Fu, H. C., Russell, C. T., Song, P., Khurana, K. K. and Singer, H. J. (1997), 'A new functional form to study the solar wind control of the magnetopause size and shape', *J. Geophys. Res.: Space Phys.* **102**(A5), 9497–9511.

SILSO World Data Center (2022), 'The international sunspot number', *International Sunspot Number Monthly Bulletin and online catalogue* .

Skoug, R. M., Feldman, W. C., Gosling, J. T., McComas, D. J. and Smith, C. W. (2000), 'Solar wind electron characteristics inside and outside coronal mass ejections', *J. Geophys. Res.: Space Phys.* **105**(A10), 23069–23084.

Smith, C., L'Heureux, J., Ness, N., Acuña, M., L.F., B. and Scheifele, J. (1998), 'The ace magnetic fields experiment', *Space Sci. Rev.* **86**(613–632).

Smith, E. and Balogh, A. (1995), 'Ulysses observations of the radial magnetic field', *Geophys. Res. Lett.* **22**(23), 3317–3320.

Smith, E. and Balogh, A. (2003), 'Open magnetic flux: Variation with latitude and solar cycle', *Solar Wind Ten: Proceedings of the Tenth International Solar Wind Conference, Pisa, Italy* **679**, 67–70.

Smith, E. J. (2001), 'The heliospheric current sheet', *Journal of Geophysical Research: Space Physics* **106**(A8), 15819–15831.

Srivastava, N., Schwenn, R., Inhester, B., Stenborg, G. and Podlipnik, B. (1999), 'Acceleration Profile of the Slow Solar Wind as Inferred from Gradual Mass Ejections Observed by LASCO', *Space Science Reviews* **87**(1), 303–306.
URL: *https://doi.org/10.1023/A:1005189610536*

Stone, E. C., Frandsen, A., Mewaldt, R., Christian, E., Margolies, D., Ormes, J. and Snow, F. (1998), 'The advanced composition explorer', *Space Science Reviews* **86**(1), 1–22.

Stverak, S., Maksimovic, M., Travnicek, P. M., Marsch, E., Fazakerley, A. N. and Scime, E. E. (2009), 'Radial evolution of nonthermal electron populations in the low-latitude solar wind: Helios, cluster, and ulysses observations', *Journal of Geophysical Research: Space Physics* **114**(A5).

Suess, S., Phillips, J., McComas, D. and et al. (1998), 'The solar wind - inner heliosphere', *Space Sci. Rev.* **83**.

Suess, S. T. and Smith, E. J. (1996), 'Latitudinal dependence of the radial imf component: Coronal imprint', *Geophys. Res. Lett.* **23**(22), 3267–3270.

Suess, S. T., Smith, E. J., Phillips, J., Goldstein, B. E. and Nerney, S. (1996), 'Latitudinal dependence of the radial IMF component - interplanetary imprint.', *Astron. Astrophys.* **316**, 304–312.

Thomas, S., Owens, M., Lockwood, M. and Scott, C. (2014), 'Galactic cosmic ray modulation near the heliospheric current sheet', *Solar Physics* **289**(7), 2653–2668.

Vallee, J. P. (1998), 'Observations of the Magnetic Fields Inside and Outside the Solar System: From Meteorites ($\sim$ 10 attoparsecs), Asteroids, Planets, Stars, Pulsars, Masers, to Protostellar Cloudlets ($<$ 1 parsec)', *Fundamentals of Cosmic Physics* **19**, 319–422.

van Driel-Gesztelyi, L., Culhane, J., Baker, D., Démoulin, P., Mandrini, C. H., DeRosa, M., Rouillard, A., Opitz, A., Stenborg, G., Vourlidas, A. et al. (2012), 'Magnetic topology of active regions and coronal holes: implications for coronal outflows and the solar wind', *Solar Phys.* **281**(1), 237–262.

Vokhmyanin, M. V. and Ponyavin, D. I. (2013), 'Sector structure of the interplanetary magnetic field in the nineteenth century', *Geophysical Research Letters* **40**(14), 3512–3516.

URL: *https://agupubs.onlinelibrary.wiley.com/doi/abs/10.1002/grl.50749*

ŠtveráK, Š., Trávníček, P., Maksimovic, M., Marsch, E., Fazakerley, A. N. and Scime, E. E. (2008), 'Electron temperature anisotropy constraints in the solar wind', *Journal of Geophysical Research (Space Physics)* **113**(A3), A03103.

Wallace, S., Arge, C., Pattichis, M., Hock-Mysliwiec, R. and Henney, C. (2019), 'Estimating total open heliospheric magnetic flux', *Solar Phys.* pp. 1–23.

Wang, Y.-M., Hawley, S. H. and Sheeley, N. R. (1996), 'The magnetic nature of coronal holes', *Science* **271**(5248), 464–469.

Wang, Y. M. and Sheeley, Jr., N. (1992), 'On Potential Field Models of the Solar Corona', *Astrophys. J.* **392**, 310.

Wang, Y.-M. and Sheeley, Jr., N. (1995), 'Solar implications of *Ulysses* interplanetary field measurements', *Astrophys. J.* **447**(2).

Wang, Y.-M., Ulrich, R. K. and Harvey, J. W. (2022), 'Magnetograph saturation and the open flux problem', *Astrophys. J.* **926**(2), 113.

Webb, D. F. and Howard, T. A. (2012), 'Coronal mass ejections: Observations', *Living Reviews in Solar Physics* **9**(1), 1–83.

Wenzel, K. P., Marsden, R. G., Page, D. E. and Smith, E. J. (1992), 'The ULYSSES Mission', *Astron. Astrophys. Suppl.* **92**, 207.

Wilcox, J. M., Scherrer, P. H. and Hoeksema, J. T. (1980), 'The origin of the warped heliospheric current sheet'.

Zeilik, M. (2002), *Astronomy: The Evolving Universe*, Cambridge University Press.